Superconducting thin film nanoelectronics

by

Adam Nykoruk McCaughan

Submitted to the Department of Electrical Engineering and Computer Science
in partial fulfillment of the requirements for the degree of

Doctor of Philosophy in Electrical Engineering

at the

MASSACHUSETTS INSTITUTE OF TECHNOLOGY

September 2015

Author .....
Department of Electrical Engineering and Computer Science
August 31, 2015

Certified by .....
Karl K. Berggren
Professor of Electrical Engineering and Computer Science
Thesis Supervisor

Accepted by .....
Leslie A. Kolodziejski
Chairman, Department Committee on Graduate Theses

Superconducting thin film nanoelectronics

by

Adam Nykoruk McCaughan

Submitted to the Department of Electrical Engineering and Computer Science
on August 31, 2015, in partial fulfillment of the
requirements for the degree of
Doctor of Philosophy in Electrical Engineering

Abstract

Superconducting devices have found application in a diverse set of fields due to their unique properties which cannot be reproduced in normal materials. Although many of these devices rely on the properties of bulk superconductors, superconducting devices based on thin films are finding increasing application, especially in the realms of sensing and amplification. With recent advances in electron-beam lithography, superconducting thin films can be patterned into geometries with feature sizes at or below the characteristic length scales of the superconducting state. By patterning 2D geometries with features smaller than these characteristic length scales, we were able to use nanoscale phenomena which occur in thin superconducting films to create superconducting devices which performed useful tasks such as sensor amplification, logical processing, and fluxoid state sensing. In this thesis, I describe the development, characterization, and application of three novel superconducting nanoelectronic devices: the nTron, the yTron, and the current-controlled nanoSQUID. These devices derive their functionality from the exploitation of nanoscale superconducting effects such as kinetic inductance, electrothermal suppression, and current-crowding. Patterning these devices from superconducting thin-films has allowed them to be integrated monolithically with each other and other thin-film superconducting devices such as the superconducting nanowire single-photon detector.

Thesis Supervisor: Karl K. Berggren
Title: Professor of Electrical Engineering and Computer Science

Acknowledgments

The work performed during my graduate school career was only possible thanks to the support, advice, and contributions of my colleagues, family, and friends. In particular, I would like to thank:

My advisor Karl Berggren for his enthusiasm for science, his dedication to professional and personal development, as well as his remarkable intuition. Under his direction both my creative abilities and discipline thrived.

Professor Terry Orlando and Professor Rajeev Ram for agreeing to be on my thesis committee, the excellent classes they taught, and the great advice they've given me over the years.

Isaac Chuang, for guiding me during my early years of graduate school and showing me how scientific inquisitiveness and technical discipline strongly reinforce each other.

Mark Mondol, Jim Daley, and Tim Savas for their expertise and support with everything NSL and nanofabrication-related.

Faraz Najafi, Qingyuan Zhao, Andrew Dane, Francesco Bellei, Nate Abebe, Jake Mower, Di Zhu, David Meyer, Nick Harris, Luca Alloatti, and Francesco Marsili for their many helpful discussions, collaborations, and experimental assistance.

Yachin Ivry and Richard Hobbes for their advice and insight into chemistry and other topics well outside the realm of my own research.

My colleagues Michael Gutierrez, Arolyn Conwill, Stephan Schulz, Anders Mortensen, Amira Eltony, Yufei Ge, and Paul Antohi.

My mother, father, and sister, who have always inspired me and have always supported my intellectual development. A large part of where I am today is due to their support, and I am overwhelmingly grateful. My father especially, for sharing with me his enthusiasm for research and never hesitating to support my scientific curiosity.

My wonderful fiancée (and creative muse) Cammy, who I am very excited to marry this October. Her support kept the world turning even when the demands of graduate school seemed overwhelming.

Contents

List of Figures

List of Tables

Chapter 1

Introduction to superconducting devices

Superconducting devices are being investigated and applied to address critical needs in the areas of computing [2], communications [3], and sensing [4]. They are vitally important to diverse research and industrial fields such as magnetic-field sensing [5], quantum and classical computing [6], photon sensing in communications [7], and astronomy [8] [9]. These devices fall approximately into two classes of operation: (1) devices which track and manipulate superconducting phase, and (2) devices which take advantage of non-equilibrium states of the superconducting material. Devices in the first class rely on the phase angle difference of the Ginzburg-Landau complex order parameter between bulk superconducting electrodes. Devices in the second class generally manipulate the magnitude of the Ginzburg-Landau complex order parameter, and so typically rely on weakened superconducting states which can be perturbed easily. The wide array of functionality provided by superconducting devices is sourced from these two types of operation. However, there is a large unexplored territory for new devices which can take advantage of both types of operation simultaneously.

Superconducting devices that are built out of thin films are intrinsically well-suited to the manipulation of both the phase and magnitude of the order parameter, making thin-films an ideal platform the exploration of new device functionality. In films with thicknesses on the order of the superconducting coherence length, the

superconducting state is weak but stable. In these films, the magnitude of the order parameter is tied to the phase due to the low current density J_c–the superconducting state can be broken down by over-winding the superconducting phase (equivalent to exceeding J_c). Additionally, due to the presence of kinetic inductance in films of this dimension, the phase is strongly tied to the flow of current in the device.

These relationships enable functionality to emerge from thin films just by patterning them into 2D shapes and passing current through them. Ultimately, the shape of the pattern defines the spatial evolution of the phase. When current flows through a patterned thin film the phase can take on complex patterns based on where the current injection points are and the shape of the patterned film. For example, current flowing around a notch in a thin-film nanowire will generate a large phase gradient around the sharp features of the notch. If more current is added and the phase gradient is increased, this superconducting state will actually break down at the notch, allowing vortices to enter the wire as a means of relaxing the phase

The work done in this thesis describes nanoelectronic devices which take advantage of the phase-magnitude relationship of thin superconducting films. By patterning 2D geometries into thin superconducting films, these devices utilize these relationships as well as the nanoscale effects caused by the controlled breakdown of the superconducting state [10] [11] [12] in order to produce useful functionality such as sensing and amplification. The three devices described in this thesis are the result of the exploration of this rich realm. In this introduction I describe the basic operation of each class of devices, and give examples of devices from each category.

1.1 Phase- and magnitude-based devices

Here I describe a number of devices which either use superconducting phase, or non-equilibrium dynamics of the superconducting order parameter magnitude for functionality. This list is by no means comprehensive, but serves to provide an overview of the various types of the devices in each of these categories.

1.1.1 Phase-based devices

The majority of devices which use the superconducting phase for operation are based on the Josephson junction [13] [14] [15]. The Josephson junction is a two-terminal device which is typically composed of two superconducting electrodes separated by a thin insulating layer [16]. As long as this insulating layer is on the order of (or smaller than) the superconducting coherence length ξ, the quantum states of the two electrodes overlap enough to allow electrical current to tunnel through the insulating layer without resistance. The magnitude of this tunneling current is described by the Josephson relation $I = I_c \sin\phi$, where I_c is the critical current of the junction and ϕ is the phase difference between the superconducting electrodes.

The most commonly used device which incorporates the Josephson junction is the superconducting quantum interference device (SQUID). A SQUID is formed by electrically connecting two Josephson junctions in parallel with superconducting wires. By connecting them with superconducting wires, the phase difference across the junctions becomes related and as a result anything which perturbs this phase – such as a magnetic field threading the loop formed by the SQUID – can be detected by the resulting change in the combined junction tunneling currents. This phase sensitivity gives SQUIDs their functionality as the world's most sensitive magnetometers.

Manipulation of the superconducting phase can also be used to create digital logic. One such technology is rapid-single-flux-quantum (RSFQ) logic, which tracks the phase in a SQUID loop as a way to represent the digital values of 0 and 1 [17] [18]. Since the phase in a SQUID can evolve extremely rapidly (changing by π in under a picosecond), this technology has demonstrated logical clock rates as high as 770 GHz [19].

Unfortunately, systems based on SQUIDs (including RSFQ electronics) suffer from major disadvantages which render them impractical for a variety of applications and environments. These disadvantages include low gain, high sensitivity to magnetic fields, difficulty in driving large-impedance loads, and challenges in fabrication [20]. Devices based on the SQUID must be biased with substantial amounts of current, but

are limited in how much output current they can source. The result is a device with low gain. In addition, the requirement that these devices include Josephson junctions – ultra-thin tunneling barriers – renders them notoriously sensitive to fabrication imperfections. A variation of an atomic layer in barrier thickness can radically change the operating point of a device. Finally, SQUIDs are intrinsically the most sensitive magnetic field sensors available. This feature is a blessing and a curse, as SQUID-based computing devices must be heavily shielded in order to operate.

The Andreev interferometer is one of the few devices which uses superconducting phase to produce functionality, but does not require Josephson junctions [21]. This type of interferometer can measure long-range correlations across a non-superconducting metal conductor [22]. These correlations mediate the apparent resistance of the normal metal conductor based on the superconducting phase difference between the two ends of the conductor. The Andreev interferometer can be used to spectroscopically probe the quantum state of superconducting magnetic-flux-based qubits [23].

1.1.2 Magnitude-based devices

There are a diverse set of of devices based on the various implementations of non-equilibrium superconductivity, but for the most part these devices fall into two categories: sensors, and digital devices.

Sensors Superconducting sensors have been highly successful, and have found applications in a number of fields. These devices mostly rely on the shifts in superconducting equilibrium incurred by incident radiation. One example is the superconducting-nanowire single-photon detector (SNSPD), which is used as an optical sensor for low-power classical and quantum optical processes [24] [3]. Due to its narrow cross-section, the SNSPD can detect single photons by means of a breakdown of superconductivity in the area where a photon lands. The fast response time of the SNSPD and low timing-jitter make it a leading candidate for readout integration with quantum photonic processors [25]. The SNSPD has found broad application in a diverse set of fields such as biological sensing [26], circuit thermal analysis [27], and space

communications [28].

Another example of a successful superconducting sensor is the microwave kinetic-inductance detector (MKID) [9] [4], which uses high-quality-factor superconducting resonators to detect the perturbation of the superconducting state by incident photons. Since each MKID pixel is based on a high-Q superconducting resonator, thousands of pixels can be read out on a single transmission line [29]. Due to its inherent multiplexing capabilities, this device was rapidly developed as a useful astronomical tool. In the last 20 years MKID implementations have grown dramatically, and several present-day telescopes use MKID-based cameras with over 1,000 pixels [30].

Digital devices The implementation of magnitude-based superconducting devices for logic and other digital readout applications has been less successful than their sensor counterparts [31]. These devices have the potential to use the advantages of superconducting electronics (e.g., low noise, low dissipation, high speed, etc) while avoiding the disadvantages of the Josephson junction (magnetic field sensitivity, low gain, etc), but have thus far failed to find common application because they typically require multi-layer structures for fabrication, have low input-output amplification, and low-impedance outputs.

Superconducting digital devices have been pursued ever since the 1950s (well-prior to the invention of the Josephson junction) when Dudley Buck invented the cryotron, a four-terminal logic element which was significantly more compact than the then-dominant vacuum tube technology [32]. However, these four-terminal devices were abandoned after the development of the Josephson junction and the SQUID. In the intervening years, SQUID-based technologies have dominated the literature, but a number of other devices based on non-equilibrium states have also been introduced. These include tunable-supercurrent SNS junctions [33], resistive heaters stacked on top of superconducting films [34], quasiparticle-injection links [35] [36] [37], and Josephson FETs [38]. Despite their diversity, all of these devices have required two or more active layers, and none have been demonstrated beyond the characterization of their basic three- or four-terminal unit. Additionally, none of them except the cryotron has been

able to demonstrate a high-gain (>10), high-impedance output ($\geq$50 Ω) which has limited their abilities to be integrated with other non-superconducting technologies. As a result, the practical implementation of any kind of superconducting logic device which avoids the disadvantages of the Josephson junction has eluded researchers for the last 40 years.

1.2 This thesis: Thin-film nanoelectronic devices

Advances in nanofabrication have enabled researchers to miniaturize devices smaller with every passing year. Currently, electron-beam lithography has enabled routine patterning of features as small as 10 nm [39] [40], which is less than nearly every intrinsic length scale of the superconducting material NbN – a material which was used extensively in the work done for this thesis. As device dimensions approach these intrinsic length scales, the resulting changes in the superconducting behavior can produce new behavior and correspondingly, new functionality. This thesis describes new devices which have been developed through the exploration of this behavior.

Current-biased nanoSQUID The first device described in this thesis is a new type of nanoSQUID which can be modulated by current biasing instead of magnetic field biasing. A description of this current-biased nanoSQUID, its output characteristics, and its development appear in Chapter 4. This device takes advantage of the kinetic inductance as a means to asymmetrically bias an otherwise-symmetric superconducting loop. Since it does not require a large magnetic inductance to operate, the method of biasing can apply to arbitrarily small nanoSQUIDs. This biasing method reduces the need for large magnetic fields to be applied at a pickup loop, which may be inadvertently coupled to the sample area.

nTron Presented next in this thesis is the nanocryotron (nTron), which is detailed in Chapter 5. The nanocryotron is based on the cryotron, which used magnetic fields induced by one superconducting wire to switch another nearby superconducting wire. The cryotron was a promising superconducting digital logic element, but was never

successfully shrunk to nanoscale sizes because its magnetic field requirements did not scale well to dimensions below several micrometers of size. The nanocryotron, however, is able to achieve similar operation to the cryotron at the nanoscale by changing the mechanism of operation from magnetic field suppression to electrothermal suppression. The key to the effectiveness of this electrothermal suppression is that the device must be on the order of – or smaller than – the quasiparticle diffusion length, which is about 100 nm in NbN.

yTron In Chapter 6, both electrothermal effects and kinetic inductance are utilized to create a novel three-terminal device called the yTron. By utilizing kinetic inductance to create current crowding, the yTron is able to act as an inline current sensor for superconducting currents. Previously, sensing superconducting currents without significantly perturbing them was only possible by weakly magnetically coupling to them. Using a Y-shaped geometry, the yTron can be used to infer the magnitude of current passing through one of the upper arms of the "Y" by measuring the critical current of the other arm. Because of the excellent film-substrate thermal coupling, this device can actually sustain a voltage state in one arm without disturbing the current in the other arm. This feature has enabled the yTron to read out quantized superconducting currents from a superconducting loop without perturbing the number of quanta in the loop.

Experimental methods In Chapter 7, I discuss a number of experimental techniques which enabled the rapid development of the devices described here. Among these include a robust way to perform I_c measurements, along with a discussion why it is important to choose a consistent I_c measurement method. Also included is a primer on automating test measurements using Python and GPIB, and details regarding the fabrication of the sample holders that were used for submerging samples in liquid helium.

Chapter 2

Nanoscale superconducting devices

While superconductivity has been a topic of research since 1911, only recently have superconducting device dimensions reliably approached the nanoscale. In many cases, shrinking these superconducting devices has the potential to yield improve metrics. For example, in superconducting nanowire single photon detectors (SNSPDs), narrower nanowires have enabled the detection of longer wavelengths with better efficiency [41]. For superconducting magnetometers such as the nanoSQUID [42] [43], reducing device sizes down to the nanoscale has enabled them to be sensitive to the point of detecting a single electron spin [44]. For large-scale integrated superconducting electronics such as rapid-single-flux-quantum logic (RSFQ) [17], scaling down the basic element of computation – the Josephson junction – has reduced power consumption and increased their density of integration [45].

However, even as device sizes shrink, the fundamental length scales which govern a superconducting material remain approximately constant. This scaling leads to a variety of effects which can impact the operation of miniaturized devices. Although these effects can adversely impact the operation of existing devices, these phenomena can also be exploited to create new devices as well.

2.1 The effects of scaling down superconductors

Although superconductivity is best known as the transition of a material from being electrically resistive to having zero resistance, there are several other effects which are relevant to superconducting device construction. Additionally, there are additional phenomena which begin to manifest as the length scales of the superconducting object are reduced. Here we describe some of the basic principles of bulk superconductors, and analyze how these principles are affected by reduced dimensions.

2.1.1 Characteristics of bulk superconductors

Superconductivity is characterized by the transition of a material from a diffusive "sea" of electrons to the condensation of a macroscopic quantum state [46] [47]. This quantum state is characterized by the superconducting energy gap Δ, which represents the energy difference between the quasiparticle sea and the superconducting ground state. This energy can also be interpreted as a frequency through the relation $f = \Delta/h$, where h is Planck's constant equal to $6.626 \times 10^{-34}\,\mathrm{J\,s}$. The frequency f, which is typically in the hundreds of gigahertz, is called the gap frequency and can be thought of as the minimum frequency that incoming radiation would need to have to perturb the superconducting state.

The onset of superconductivity occurs when certain materials drop below what is called the transition temperature or critical temperature T_c. When the material temperature drops below T_c, the electrons in the material become correlated and binding together to form Cooper pairs. This attraction is actually present at all temperatures in the material, but at temperatures above T_c the spectrum of phonon noise in the system includes frequencies above f (with non-negligible amplitudes), meaning the electron-electron attraction is drowned out and correlations are destroyed as quickly as they are formed.

These correlated electrons, or Cooper pairs, are able to move through the material while avoiding several types of scattering that would otherwise affect a single electron. Specifically, the scattering sources which are avoided are those due which are

symmetric to time-reversal, e.g. phonons and non-magnetic impurities. This lack of scattering means that current can be carried through the material without resistance. Unlike normal electrons, the Cooper pairs do not have their momentum randomized as they scatter off atoms in the material lattice, and so are able to carry current without dissipation, as well as store energy in their motion.

Additionally, superconductors can be subjected to a certain magnitude of magnetic field before the magnetic field is allowed to penetrate or destroy the superconducting state. This magnitude is called the critical field, and its level is dependent on the superconducting material (H_{c1} or H_{c2}). Associated with this magnetic field is a metric called the critical current density J_{c}. Although a superconductor can carry current without dissipation, the total amount of current it can carry before breaking down is finite. As the result of this critical current, superconductors can exhibit strongly nonlinear responses by being biased near J_{c}. This nonlinear response was made use of extensively in the production of the devices described in this thesis.

As a result of the ability to carry current without resistance, superconductors act similarly to perfect conductors and are able to repel applied magnetic fields. If, for example, a magnetic field is applied to a perfectly conducting sphere with an infinite charge carrier density, magnetic induction produces a surface current on the sphere which generates an equal and opposite field inside the sphere. Thus, the superposition of the applied field and the induced field cancel each other. The result is that the sphere gains a surface current. This surface current does not dissipate, and so never allows the magnetic field into the sphere's core; the magnetic field inside the sphere remains constant under all conditions.

Although its surface currents can be carried without dissipation, a superconducting sphere's interior is not perfectly shielded from magnetic fields. Due to the finite density and non-zero mass of the charge carriers, magnetic fields are imperfectly screened on the surface of a superconductor. As a result, an applied magnetic field penetrates into a superconductor's surface to a finite depth – this depth is generally known as the "penetration depth" λ. In the superconducting clean limit (e.g. when looking at bulk niobium), this depth is called the "London penetration depth" λ_{L}.

The penetration depth refers to the fact that in the surface of the superconductor, the magnetic field falls off exponentially as $B(x) = B_0 \exp\left(-\frac{x}{\lambda}\right)$, where x is the depth into the material. This thesis deals primarily with thin-film niobium and niobium nitride and so we will deal only with the dirty-limit form of λ. The equation describing λ is [46]

$$\lambda = \sqrt{\frac{h}{2\pi^2 \Delta \mu_0 \sigma_n}} \tag{2.1}$$

where μ_0 is the magnetic permeability of vacuum, and σ_n is the normal-state conductivity of the material (as measured just above T_c).

2.1.2 Superconducting thin films and kinetic inductance

If the superconducting sphere is scaled down so that its radius is on the order of λ, however, the magnetic field will be able to penetrate the entire sphere to some degree. As a result, current will flow throughout the entirety of the sphere, trying to repel as much of the magnetic field as possible. However, due to its small dimension, there are a limited number of electrons available for carrying the surface currents in the superconductor. In these circumstances, the Cooper pairs act as an inertial energy storage mechanism, since each Cooper pair (composed of two correlated electrons) carries kinetic energy $E_k = 2(\frac{1}{2} m_e v^2)$, where m_e is the mass of the electron and v is its velocity. This kinetic inductance is not typically present in normal conductors (except under very high frequency radiation), because this energy is continually dissipated due to scattering.

This inertial energy storage is called kinetic inductance because it is an analogous energy storage mechanism to the more familiar magnetic inductance. In both superconductors and normal conductors, energy is stored in the magnetic field surrounding the current-carrying conductor. The amount of energy stored in the magnetic field is dependent solely on the magnitude of current, the geometry of the conductor, and the magnetic permeability of the materials surrounding it. In superconductors, the energy stored in the kinetic motion of the Cooper pairs also depends on magnitude

of current, but since the energy storage is taking place inside the conductor – instead of an external magnetic field – it does not depend on the surrounding geometry. The total amount of energy carried by the Cooper pairs in a superconducting wire can be equated to the inductive energy storage term L_{k} by

$$2(\frac{1}{2}m_e v^2)(n_s l A) = \frac{1}{2}L_K I^2 \tag{2.2}$$

where v is the velocity of the Cooper pairs, n_s is the Cooper pair density per unit volume, l is the length of the wire, A is the cross-sectional area of the wire, and I is the total current carried by the wire.

For a fixed amount of current circulating in a superconducting object, the disparity between the energy stored in the magnetic field versus the energy stored in the kinetic motion increases as the size of the superconducting object shrinks. Take for example a very thin superconducting disc with a magnetic field applied perpendicular to the disc plane. If the thickness of the disc is such that $t << \lambda$, the magnetic field inside the superconducting material will be almost completely uniform. The circulating current induced by the applied magnetic field will be carried by all the Cooper pairs in the entire volume of the device. If the disc is thinned by a factor of two, there will be half the number of total charge-carrying Cooper pairs available to carry current. So to carry a given amount of current, each of the Cooper pairs will have approximately double the velocity. Along with this doubled velocity, the kinetic energy storage per unit current the kinetic inductance will also approximately double since $L_{\mathrm{k}} \propto A$. However, reducing the disc thickness does not significantly change the magnetic inductance of the disc, and so as the length scales of the superconducting object shrink below λ, the kinetic inductance can overtake the magnetic inductance.

A useful approximation for kinetic inductance in a dirty thin film can be produced using only the superconducting gap energy and the London penetration depth. This approximation assumes that the superconducting material obeys the BCS relation $2\Delta_0 = 3.528 k_{\mathrm{B}} T_{\mathrm{c}}$, which may not be true for extremely thin films or exotic materials, but is a reasonable estimate for the dirty-limit films used in this thesis. The

approximation is [4]

$$L_{\mathrm{k}} = \mu_0 \lambda^2 / t = \frac{\hbar R_{\mathrm{s}}}{\pi \Delta_0} = 1.38 \frac{R_{\mathrm{s}}}{T_{\mathrm{c}}} \quad \mathrm{pH}/\square \tag{2.3}$$

where R_{s} is the thin-film sheet resistance (measured just above T_{c}), and L_{k} is measured in terms of the sheet inductance of the thin film. The sheet inductance is similar to the sheet resistivity, and is measured by counting the number of squares in a current path. For instance, a 1 µm long wire that is 100 nm wide would be ten squares long, regardless of thickness. To complete the example and calculate the sheet inductance for a realistic film, if the film had a sheet resistance of R_{s} of 300 Ω/□ and a T_{c} of 12 K, the kinetic inductance per square of the film would be 34.5 pH/□, and the total inductance of the ten-square-long wire would be approximately 345 pH.

2.2 Applications of thin superconducting films

Patterning devices out of thin superconducting films is a useful approach for making devices which have at least one nanometer-scale dimension. For instance, there are several devices which can be produced from few-nanometer-thick superconducting thin films, such as the superconducting nanowire single photon detector (SNSPD) [48]. The SNSPD is a nanowire typically about 4 nm thick and 100 nm wide, have lengths on the order of 100 µm to 1000 µm, and are made from niobium nitride (NbN) or tungsten silicide (WSi) [49] [50]. Due to their thin nature they have tens to hundreds of nanohenries of kinetic inductance–typically each square (100 nm × 100 nm segment) of the nanowire contributes 50 pH–100 pH of inductance. In operation, these devices are current biased such that the wire current density is just below J_{c}, the critical current density of the superconducting material. When an optical photon lands on the nanowire, it deposits its energy onto the wire and perturbs the superconductivity in a small area. Due to the extremely small dimensions of the nanowire, this <1 eV perturbation is enough to suppress J_{c} at cross-section of the wire where the photon lands. The result is that the superconductivity breaks down at the photon arrival location, forming a resistive region known as a hotspot. This resistive region expels

the current from the nanowire, and diverts it out into a load impedance such as an amplifier or transmission line.

Aside from its need for a small cross-section, the SNSPD derives much of its functionality from its thin-film nature. First, by virtue of its large total kinetic inductance, the current which is diverted into the external load takes some time to recover back into the nanowire. This recovery time is critical to the free-running operation of the SNSPD, as the expelled current must remain diverted from the nanowire long enough for the nanowire resistive region to cool and heal back into the superconducting state [51]. The second advantage of fabricating an SNSPD from a thin film also ties into this cooldown time. Because the nanowire cross section is wide and thin, the superconducting material making up the SNSPD has a large surface area which is in intimate contact with the substrate [52]. For the SNSPD, the substrate acts as a thermal tank which cools the resistive hotspot. A wide and thin cross-section allows for excellent thermal coupling between the device and the substrate, and speeds up this cooling process. This increased thermal coupling allows the device to recover more quickly and operate at a higher count rate.

Another device which is typically fabricated from a superconducting thin film is the kinetic inductance detector (KID) [9]. The MKID consists of an LC resonator where the inductive component is provided by the kinetic inductance of a thin film. Hundreds or thousands of these resonators can be capacitively coupled to a transmission line, such that each resonator has a unique resonant frequency $f_i = 1/\sqrt{LC}$. By measuring the spectrum of the transmission line, each resonator can be uniquely identified by its frequency. When a photon lands on one of the resonators, some of the Cooper pairs in that resonator are briefly broken apart. Since the total number of available Cooper pairs is reduced in the resonator, the kinetic inductance of the resonator increases and correspondingly, the resonant frequency of that resonator is reduced. That frequency shift can then be read out by looking at the spectrum of the transmission line. Thus, using a single transmission line several thousand KIDs can be read out simultaneously.

Both the SNSPD and KID are typically created by patterning and etching a su-

perconducting thin film. This fabrication method has natural advantages for devices whose functionality relies on thin film properties such as kinetic inductance or excellent thermal cooling. The growth of thin films can be controlled to the sub-nanometer level by sputter deposition, and can be deposited in thickness ranging from a few nanometers to hundreds of nanometers [53]. Due to this range and precision, devices which rely on kinetic inductance can have their thicknesses tuned precisely. By growing a thin film, the smallest dimension of the device can be characterized in advance, and only 2D patterning is needed to complete the fabrication process.

Chapter 3

The 2D electrothermal model

To better understand the operation of a new device, it is important to build a simulation or analysis framework with which to test observations. In the case of the SNSPDs, the development of a 1D electrothermal model [54] was crucial to the development and understanding of the nanowire physics. However, this 1D model was not applicable to devices that have a fundamentally 2D geometry such as those described in this thesis. This chapter describes the development and application of the 2D electrothermal model, which was used with great success to simulate the operation of the nTron and yTron.

3.1 Electrothermal basics

The electrothermal model described here is based on the two-temperature model described by Ref. [55]. In this work, the authors analyze a superconducting film in terms of two effective temperatures: the electron temperature T_{e}, and the phonon temperature T_{ph}. These temperatures represent the non-equilibrium distributions of the electron and phonon systems, respectively. These temperatures are spatially dependent, for example, the local value of T_{e} corresponds approximately to the local density of Cooper pairs and may vary spatially across the device. This formulation lends itself well to simulating device operation, as it is inherently time-dependent, couples the systems together in a straightforward fashion, applies to a wide range

of temperatures (e.g. not only $T \ll T_c$ or $T \approx T_c$), and can smoothly transition between the superconducting and normal states.

To implement the two-temperature model then, the first step was to choose a numerical solver capable of working with the partial differential equations (PDE) of interest: an electrical PDE and two thermal PDEs. For this implementation, we used the COMSOL numerical simulation software, which had a built-in heat equation PDE, current flow PDE, and allows for multiple PDEs to be coupled easily. After that, it was a matter of implementing the relevant equations and parameters to suit the material of interest, in this case, thin-film niobium nitride (NbN).

3.1.1 The heat equation

The two-temperature model desribed in Ref. [55] used two coupled heat equation PDEs to describe the effect electron and phonon temperatures of the superconducting material. The heat equation PDE fundamentally describes the inflow and outflow of thermal energy versus time for each point in space. Its most basic form is

$$\frac{\partial(cT)}{\partial t} = \nabla^2(\kappa T) \tag{3.1}$$

where T is the temperature, c is the specific heat of the material, κ is the in-plane thermal conductivity of the material. In the implementation described here, all of these variables are functions of both space and time (e.g. κ is $\kappa(\vec{r}, t)$). For every point in space, what Eq. 3.1 describes is the conservation of thermal energy during a diffusive process, neglecting any external couplings. For any point in space, the rate of thermal energy loss (the left term of Eq. 3.1) is equal to the curvature of the thermal energy (the right term of Eq. 3.1). This characterizes a diffusive thermal process: as time passes the system smooths any non-uniformity in T such that the whole geometry tends to a uniform temperature.

3.1.2 Modifying the basic heat equation

The basic form of the heat equation shown in Eq. 3.1 neglects any outside sources of thermal heating or cooling, and so only describes the passive diffusion of heat from a given starting condition. In order to fully describe the operation of a current-biased thin film on a substrate, this equation must add three additional terms: one term to represent electrical Joule heating from current flow across resistive regions, one term to represent the thermal coupling of the film to the substrate, and one term to describe the coupling between the electron and phonon systems. Since the substrate subtracts energy only from the phonon system, and the Joule heating adds energy to only the electron system, it is now prudent to explicitly write out the two coupled heat equation PDEs and the electrical PDE.

Electron temperature PDE

Eq. 3.2 describes the electron system effective temperature, and is represented by the basic heat equation with an additional term for Joule heating, and another term to represent the electron-phonon coupling.

$$\frac{\partial(c_{\mathrm{e}} T_{\mathrm{e}})}{\partial t} = \nabla^2(\kappa_{\mathrm{e}} T_{\mathrm{e}}) + |\mathbf{J}|^2 \rho - \frac{c_{\mathrm{e}}}{\tau_{\text{e-ph}}}(T_{\mathrm{e}} - T_{\mathrm{ph}}) \tag{3.2}$$

In Eq. 3.2, c_{e} is the electron specific heat, κ_{e} is the electron thermal conductivity, $|\mathbf{J}|^2$ is the norm of the current density, ρ is the resistivity, and $\tau_{\text{e-ph}}$ is the electron-phonon interaction time. Since experimental measurements often measure D_{e} and c_{e} instead of κ_{e} directly, it should be noted that κ_{e} and c_{e} are related by the standard thermal diffusivity relation $D_{\mathrm{e}} = \kappa_{\mathrm{e}}/c_{\mathrm{e}}$.

Phonon temperature PDE

To describe the phonon system, we use the basic heat equation with an additional term for cooling into substrate, as well as another term to represent the electron-phonon coupling. The term for electron-phonon coupling is the negative of the term in Eq. 3.2) so that the sum of the two coupling terms is zero, because the coupling

only describes energy transfer and not net gain or loss. The equation for the phonon system then becomes

$$\frac{\partial(c_{\mathrm{ph}}\,T_{\mathrm{ph}})}{\partial t} = \nabla^2(\kappa_{\mathrm{ph}}\,T_{\mathrm{ph}}) - \frac{c_{\mathrm{ph}}}{\tau_{\mathrm{esc}}}(T_{\mathrm{ph}} - T_{\mathrm{sub}}) + \frac{c_{\mathrm{e}}}{\tau_{\mathrm{e\text{-}ph}}}(T_{\mathrm{e}} - T_{\mathrm{ph}}) \tag{3.3}$$

where c_{ph} was the phonon specific heat, κ_{e} was the phonon thermal conductivity, T_{sub} is the temperature of the substrate, and τ_{esc} was the escape time constant which determined the rate of cooling into the substrate. Note that the term with the escape time constant has several different forms–for instance, it can instead be replaced by the Kapitza resistance which has the form $((T_{\mathrm{ph}})^{\eta} - (T_{\mathrm{sub}})^{\eta})$ where η is typically 4, but can range between 3 and 6 depending on the substrate-film interface [56]. The precise form was never adequately measured in our NbN films, and so the form given by Ref. [24] above was used. Literature on transition-edge sensors has a wealth of information on this topic for further investigation [56]. As described before, all of the variables in Eq. 3.2 and Eq. 3.3 are spatially dependent and time dependent, with the exception of the parameters T_{sub} which is a constant.

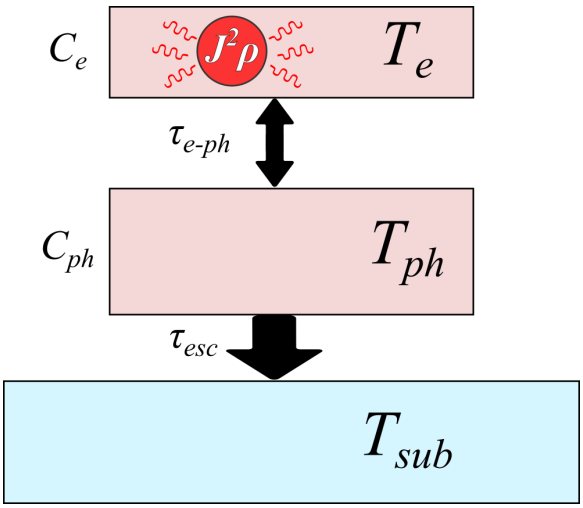

Figure 3-1: Diagram showing the production and flow of energy between the different coupled systems in the electrothermal model.

Electrical currents PDE

The electron temperature heat equation now contains a term corresponding to resistive heating caused by current flow. This means that there must be a third PDE coupled to the two heat equation PDEs, which couples to the electron system heat equation by the Joule heating term $|\mathbf{J}|^2\rho$. This PDE is based on Ohm's law:

$$\mathbf{J} = \frac{1}{\rho}\mathbf{E} \tag{3.4}$$

3.2 Adapting the 1D model to 2D

Much of the groundwork for this implementation was laid out in Ref. [54], which outlines an electrothermal model in one dimension. While it would have been convenient to simply impose the correct boundary conditions to adapt the 1D model to 2D, it was not that simple. The greatest difference between the 1D implementation and the one outlined here was the 1D model's discrete separation of the superconducting and normal states. In the 1D model, when $T > T_\mathrm{c}$ or $J > J_\mathrm{c}$ for any segment of the wire, the internal logic of the simulation instantaneously changed that segment of the wire from being completely superconducting (zero resistance) to completely normal.

The discrete division of the superconducting state from the resistive state was not possible in a 2D topology, due to the effect of current crowding [57]. Consider the example of a current-biased superconducting nanowire which has a photon land on it. The simulation begins with a nanowire which has a constant current flowing through it such that J is well below J_c. If a photon lands and a resistive island is formed in the center of the nanowire, physically one would expect the resistive spot to dissipate since there is not enough current to support the creation of a full hotspot. However, in this numerical implementation, in the time step following the creation of the resistive island, the solver will compute the current flow around that resistive island. In this time step, current crowding guarantees the solver will see a greatly increased current density at the boundary between the normal and superconducting sections–especially if the mesh is coarse. Then, because $J > J_\mathrm{c}$ for the mesh elements

near the boundary of the island, the solver will set those elements to the normal state, increasing the size of the island. This process will continue until every mesh element in the entire wire is resistive. Additionally, this erroneous process occurs no matter how small the timesteps are because the boolean check of $J > J_c$. For instance, if the solver steps with 1 fs increments, the entire wire can become resistive in under a picosecond, which represents a non-physical response.

The non-physical expansion of resistive regions was amended in the 2D model by more fully implementing the two-temperature model and eliminating the discrete division of the superconducting and resistive states. In the two-temperature model, the resistivity becomes a function dependent only on T_e. Since the T_e heat equation is fundamentally diffusive, this helps ensure a spatially-smooth solution for ρ. Instead of adjacent mesh elements having different states and causing current-crowding, the value of T_e and thus ρ instead varies smoothly over several mesh elements. This adaptation also requires a modification of the Joule heating term of the two-temperature model. In the 1D model, the discrete superconducting and resistive states make calculation of the Joule heating simple: superconducting sections do not produce Joule heating, and resistive sections produce Joule heating according to $I^2 R_n$, where I is the current flowing through the 1D wire and R_n is the normal resistivity of that segment. In the 2D model this distinction is not quite so clear since the superconducting and normal state are not as well-defined. This 2D model implements the Joule heating by adding the equation for $J_c(T_e)$, so that everywhere $T_e < T_c$ has a nonzero J_c. We then assumed that the Joule heating for any area where $T_e < T_c$ was equal to $\min\left(\left(|\mathbf{J}| - Jc(Te)\right)^2, 0\right)$. This form had a phenomenological purpose: it prevented the model from producing heating in areas where the current density was smaller than J_c, even if the resistivity was nonzero. It is unclear whether this formulation was microscopically accurate, but subtracting the $J_c(T_e)$ term from the current density norm reduced the time to numerical convergence, and did not appear to affect the operational results when the simulation was used on actual device geometries. from

3.3 Variables, equations, and parameters

This section lists all the physical variables and parameters used in constructing the 2D electrothermal model, the references in which they appeared, and notes specific to their implementation in COMSOL. Most of the values compiled here were specific to thin-film NbN .

3.3.1 Electrothermal variables

The superconducting gap energy Δ

The equation for the superconducting gap Δ can typically only be solved by numerical integration [46]. However, for standard BCS superconductors there is a form that is accurate to within a few percent, which can be found in Ref. [58]. This form is

$$\Delta(T_\mathrm{e}) = 1.76 k_\mathrm{B} T_\mathrm{c} \tanh\left(\frac{\pi}{1.76}\sqrt{\frac{2}{3}(1.43)\left(\frac{T_\mathrm{c}}{T_\mathrm{e}}-1\right)}\right) \tag{3.5}$$

where k_B is Boltzmann's constant, and T_c is the thin-film superconducting critical temperature which was measured to be 12.6 K. A plot using these parameters is shown in Fig. 3-2.

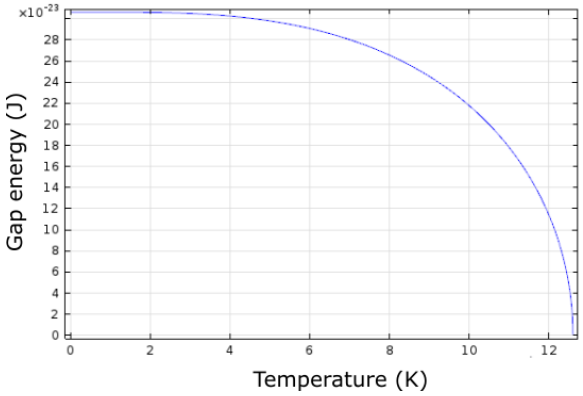

Figure 3-2: A graph of Eq. 3.5, plotting the superconducting bandgap Δ versus temperature.

The electron specific heat c_e

The equation for the electron specific heat c_e is state dependent [54]. In the superconducting state ($T_e < T_c$), it decays exponentially with temperature. In the normal state ($T_e \geq T_c$), it increases linearly like most metals. Its form is

$$c_e(T_e) = \begin{cases} A \exp\left(-\Delta(T_e)/(k_B * T_e)\right) & 0 < T_e < T_c \\ c_{e0} T_e & T_e \geq T_c \end{cases} \tag{3.6}$$

where c_{e0} was 240 J/(m^{3}K^2) for thin-film NbN [24], and A was the proportionality constant $2.43 c_{e0} T_c$. The electron specific heat had a discontinuity at $T_e = T_c$, corresponding to the specific heat gained by the onset of superconductivity. This discontinuity caused problems in the simulation, because when the solver made small changes to T_e around T_c, the specific heat changed drastically. To remedy this issue, the COMSOL function was smoothed by enforcing a continuous second derivative, sacrificing some accuracy for the sake of ensuring the solution converged successfully. A plot using these parameters is shown in Fig. 3-3.

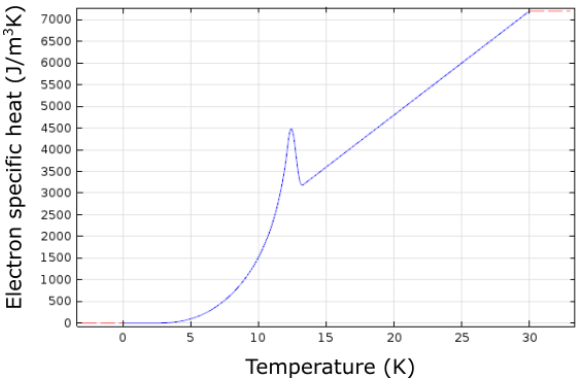

Figure 3-3: A graph of Eq. 3.6, showing the electron specific heat c_e versus electron temperature T_e.

The electron thermal conductivity κ_e

The thermal conductivity of the electron system was also state-dependent. Its equation for $T_e > T_c$ was well defined, but in the superconducting state there are several formulae and representations that can be used. One solution, used in Ref. [59] and

subsequently in Ref. [54], was to linearly interpolate $\kappa_e(T_e)$ between zero and its value at T_c. This is expressed by the piecewise equation

$$\kappa_e(T_e) = \begin{cases} \frac{L T_e}{\rho_{20K}} \left(\frac{T_e}{T_c}\right) & 0 < T_e < T_c \\ \frac{L T_e}{\rho_{20K}} & T_e \geq T_c \end{cases} \tag{3.7}$$

where L is the Lorenz number $L = 2.44 \times 10^{-8}\,\mathrm{W\Omega/K^2}$, and ρ_{20K} was the normal resistivity of the NbN film (measured just above T_c) which had a value of $2.85 \times 10^{-6}\,\Omega\,\mathrm{m}$. A plot using these parameters is shown in Fig. 3-4.

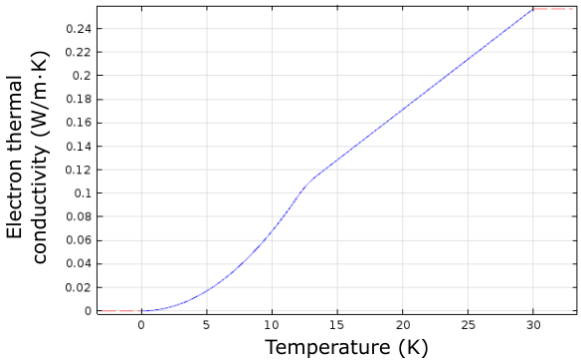

Figure 3-4: A graph of Eq. 3.7, showing the electron thermal conductivity κ_e versus temperature.

The resistivity ρ

For simulation purposes, it was convenient to not distinguish ρ expressly between the superconducting and normal states, and instead express the onset of superconductivity as a smooth reduction of $\rho(T_e)$ as T_e approached zero. This was accomplished using modified version of the form specified in Ref. [24]:

$$\rho(T_e) = \rho_{20K}\left(1 + \exp\left(-4\frac{T_e - T_c}{dT_c}\right)\right)^{-1} + \rho_{sc}\left(1 + \frac{T_e}{T_c}\right) \tag{3.8}$$

where ρ_{sc} was an artificial constant set to $1 \times 10^{-8}\,\Omega\,\mathrm{m}$, and dT_c was the width of the resistive-to-superconducting transition, set to 1.1 K. This modified form includes the $\rho_{sc}\left(1 + \frac{T_e}{T_c}\right)$ term as a way to assist the solver in converging to a solution. Without this term, near $T_e = 0$ the resistivity becomes exponentially close to zero. This

approach to zero causes problems for the solver because the values in the electrical PDE has a $1/\rho$ term which diverges rapidly. By adding the extra term, ρ was given a minimum value of ρ_{sc} which limited the size of the $1/\rho$ component of the electrical PDE solution. The $\left(1+\frac{T_{\mathrm{e}}}{T_{\mathrm{c}}}\right)$ part of the extra term additionally enforced a minimum value to the first derivative of ρ, which also helped with convergence. A plot showing both ρ and $\sigma = 1/\rho$ is shown in Fig. 3-5 to help illustrate this point.

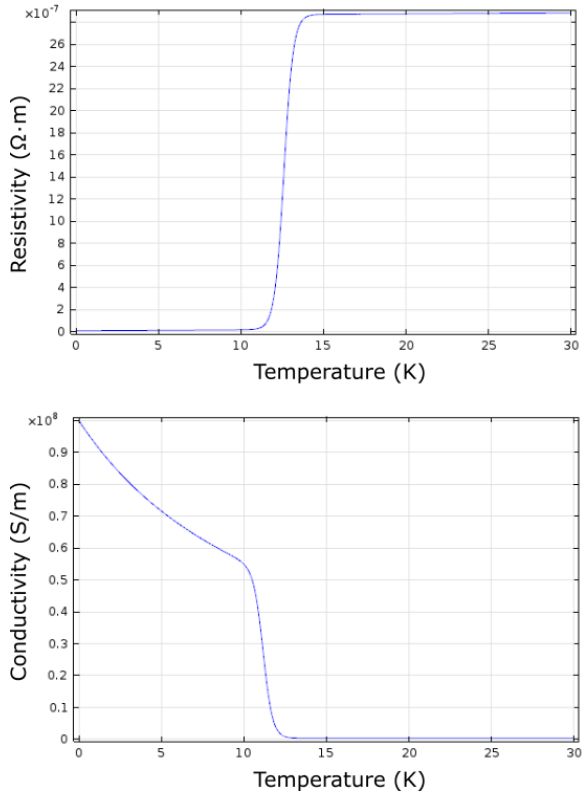

Figure 3-5: (above) A graph of Eq. 3.8, showing the resistivity ρ versus temperature. (below) A graph of the inverse of Eq. 3.8, showing the conductivity $1/\rho$ versus temperature.

The critical current density J_{c}

The form of the critical current density is taken directly from Ref. [60]. The equation is

$$J_{\mathrm{c}}(T_{\mathrm{e}}) = J_{\mathrm{c0}}\left(1-\left(\frac{T_{\mathrm{e}}}{T_{\mathrm{c}}}\right)^2\right)^{3/2}\left(1+\left(\frac{T_{\mathrm{e}}}{T_{\mathrm{c}}}\right)^2\right)^{1/2} \tag{3.9}$$

where J_{c0} was the measured critical current density of the NbN film. This value was $6.6 \times 10^{10}\,\mathrm{A/m^2}$ for thin-film NbN, and was determined by measuring the critical current of a relatively wide (1 µm) wire, and dividing it by the cross-sectional area of the wire. A plot using these parameters is shown in Fig. 3-6.

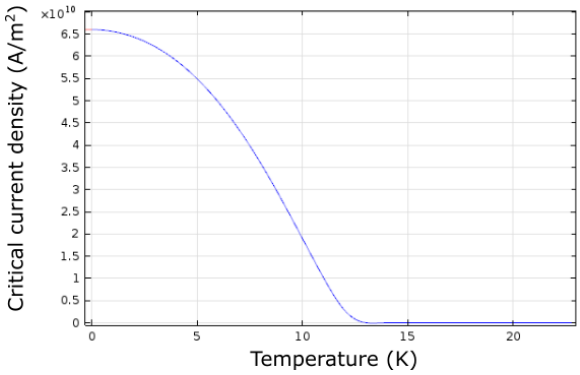

Figure 3-6: A graph of Eq. 3.9, showing the critical current density J_c versus temperature.

The electron-phonon interaction time $\tau_{\text{e-ph}}$

The electron-phonon interaction time described the rate at which the phonon and electron effective temperatures reached equilibrium with each other. The form used in this implementation was taken from Ref. [24], and was

$$\tau_{\text{e-ph}}(T_e) = \tau_{\text{e-ph0}} \left(\frac{T_e}{T_c} \right)^{-1.6} \tag{3.10}$$

where $\tau_{\text{e-ph0}}$ was 17 ps. A plot using these parameters is shown in Fig. 3-7.

The phonon specific heat c_{ph}

Only one of the variables in the electrothermal model depended on on the phonon temperature, and that variable was the phonon specific heat. The phonon specific heat was state independent, and scaled like the cube of the temperature T_{ph}:

$$c_{\text{ph}}(T_{\text{ph}}) = c_{\text{ph0}}\, {T_{\text{ph}}}^3 \tag{3.11}$$

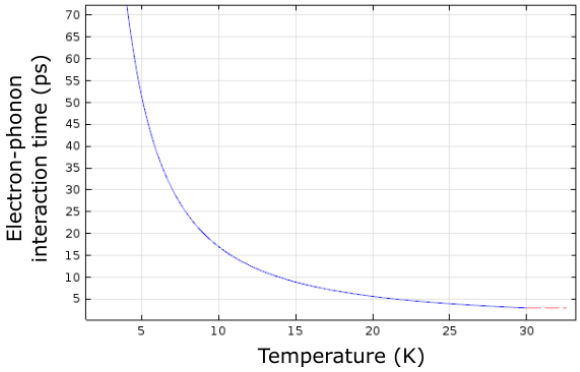

Figure 3-7: A graph of Eq. 3.10, showing the electron-phonon interaction time $\tau_{\text{e-ph}}$ versus temperature.

The value c_{ph0} was taken from Ref. [24] and was set to $9.8\,\text{J/m}^3\text{K}^4$. A plot using these parameters is shown in Fig. 3-8.

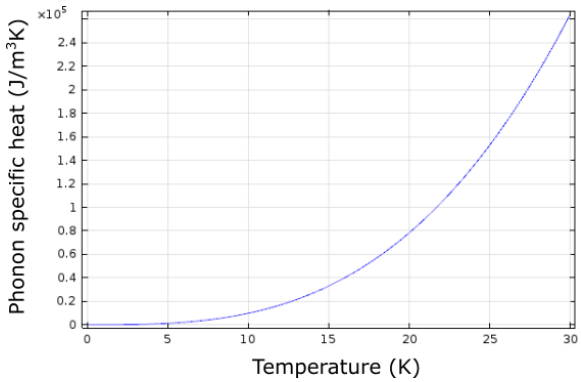

Figure 3-8: A graph of Eq. 3.11, showing the phonon specific heat c_{ph} versus phonon temperature T_{ph}.

3.3.2 Boundary conditions and initial values

The boundary conditions used in the 2D electrothermal modal were similar to those used in Ref. [54]. Electrical terminals were placed where desired on the 2D geometry, and those boundaries had their temperatures fixed to $T_{\text{e}} = T_{\text{ph}} = T_{\text{sub}}$. This boundary condition represented the wire extending off to infinity, where it was in equilibrium with the substrate temperature. All other boundaries were set to be both thermally insulating as well as electrically insulating, ensuring no heat or current passed through them.

In many situations, the NbN nanowire structures being simulated were hysteretic. Due to this hysteresis, it was required to provide the solver with sensible initial values, since at a given bias point there could be multiple solutions and the solver would not know which ones to choose. The most robust method that was found for setting initial values was to begin with bias conditions where the entire device was superconducting. The initial values could then be set such that everywhere $T_{\mathrm{e}} = T_{\mathrm{ph}} = T_{\mathrm{sub}}$ for the heat PDEs, and $V = 0$ everywhere for the electrical PDE. Once these initial values were set, the time dependent simulation could begin, during which the bias conditions could be changed to create resistive regions or simulation other types of operation.

3.4 Conclusions and future work

This chapter described the implementation of a 2D electrothermal model which was based off the two temperature model described by Ref. [55] and 1D implementation done in Ref. [54]. The model was critical to predicting and understanding the operation of the nTron, which is described in Chapter 3.

There are still areas of the model which could benefit from further work. The first is the inclusion of an inertial term to the electrical PDE which would model the effects of kinetic inductance. In the implementation described here, current flow is determined independently in each time step, and so may change freely from one time step to the next. In the actual physical thin film, however, kinetic inductance plays a role in ensuring current flow cannot change its magnitude or direction instantaneously. Adding a kinetic inductance term would better model the physical system, as well as likely help the implementation converge faster, since the electrical PDE would not be able to change drastically between adjacent time steps. Currently the COMSOL implementation described here was not extremely efficient, as the simulation of about 100 ps of time required about an hour on a Intel Core i7 3 GHz processor.

Another improvement that could be implemented in the 2D model would be to add the physics from a microscopic quantum theory, such as the time-dependent Ginzburg-Landau [61] equation or Usadel [62] equations. The two-temperature model described

here currently lacks an important component of current-carrying superconducting thin films: the motion of vortices. Vortices have been suggested as a mechanism for detection events in SNSPDs [63], and play an important role in other nanoscale superconducting devices [64].

Chapter 4

The current-biased nanoSQUID

The nanoSQUID is a nanoscale superconducting quantum interference device (SQUID) in which the weak-link elements are Dayem bridges [65] instead of Josephson junctions (JJs) [66]. These devices have have been fabricated from a number of materials, including aluminum [43], niobium [67] [68] [69], and lead [44], and have demonstrated flux sensitivities of $50\,\mathrm{n}\Phi_0/\sqrt{\mathrm{Hz}}$ [44], sufficient to resolve a single electron spin. The use of Dayem bridges instead of multilayer JJs allows the nanoSQUID to be patterned from a single-layer thin film, to reach diameters below 100 nm, and to be realized in high-T_c superconductors [70] [71]. At these scales, the geometric inductance of the nanoSQUID superconducting ring is small, on the order of 100 fH for a ring of size 100 nm. However, the kinetic inductance of the thin film can be significant even at these sizes, ranging from comparable to the geometric inductance to several orders of magnitude larger.

To date, nanoSQUIDs have been probed using an applied magnetic field; but in many applications, the presence of this field will perturb the sample being studied. Like a conventional SQUID, tuning the nanoSQUID to its most sensitive region typically involves coupling an external magnetic bias field to the device. In the case of scanning SQUID microscopy (SSM) the bias field must be capable of coupling several Φ_0 of flux in the nanoSQUID loop to provide closed-loop feedback. This amount of flux corresponds to a large local field that must be applied to the sensing area of the nanoSQUID, potentially perturbing the nearby sample. Here we report a new

method of modulating a nanoSQUID by coupling to the device kinetic inductance instead of its geometric inductance. We have been able to demonstrate nanoSQUID modulation without the application of any external field, using kinetic inductance coupling of currents injected asymmetrically into the nanoSQUID. More generally, this result demonstrates current-based modulation of a fluxoid inside a superconducting mesoscopic loop, which was previously performed by applying magnetic flux to the loop [72] [66] [73] [74].

The text that follows constitutes a preliminary writeup of work which will be condensed and submitted to a journal for publication.

4.1 Device characteristics

The nanoSQUID device geometry is shown in Fig. 4-1 and is composed of a superconducting ring, with four connecting terminals and two constrictions, all patterned on a 10-nm-thick niobium film. The terminals at the top and bottom of the loop were used to measure the switching current of the nanoSQUID, while the two terminals coming from the right of Fig. 4-1 were used to inject modulation current. The fabricated constrictions were 105 nm wide, several times larger than the coherence length of thin-film niobium, but significantly smaller than the thin-film penetration depth $\lambda_{\text{thin}} = \lambda^2/d$ where d is the thickness of the film and λ is the London penetration depth [75].

The device was fabricated from ∼10 nm niobium deposited on sapphire by DC magnetron sputtering. The film had a T_c of 8.2 K, a room-temperature sheet resistance of 30.4 Ω/□, and a residual resistance ratio (RRR) of 3.3. Contact pads were created by evaporating titanium and gold onto the surface using a liftoff process. The nanoSQUID geometry was then patterned by electron-beam lithography, using ∼50 nm HSQ as a resist. The pattern was transferred into the film by reactive-ion etching at 0.15 W/cm^2 for 3 min in 1.3 Pa (10 mTorr) CF_4.

These constrictions shown in Fig. 4-1 are a type of superconducting weak link, the Dayem bridge [65]. Depending on its dimensions, a Dayem bridge may have a

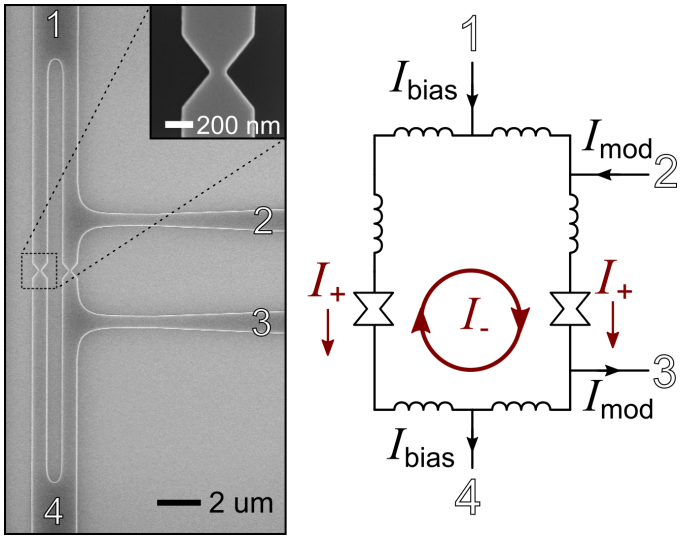

Figure 4-1: (left) Scanning-electron micrograph of a current-controlled nanoSQUID device, fabricated from a thin niobium film. Inset shows a closeup of one of the nanoSQUID constrictions, which were measured to be 105 nm wide at their narrowest point. (right) Equivalent circuit of the nanoSQUID device. Shown are the four terminals of the device and their inputs. I^{bias}, which is used to measure the switching current of the device, flows in from terminal 1 at the top and is carried out through terminal 4 at the bottom. The modulation current I_{mod} enters and leaves through the terminals 2 and 3 on the right. I_{sym} and I_{loop} are the symmetric and circulating components of I_{mod}, respectively.

significantly different current-phase relationship (CPR) than the typical Josephson relation $I = I_{\mathrm{c}} \sin(\phi)$. Our constrictions are wider than the coherence length, and so likely have a different CPR [76]. However, as long as the bridge cross section is significantly smaller than the thin-film magnetic penetration depth (λ_{thin} is $\sim$60 µm for our 10-nm-thick Nb), the CPR of the bridge is expected to be 2π-periodic and allow phase slippage [77]. The exact nature of the CPR determines the method of phase slippage. In wider bridges like the ones used here, phase slippage occurs by the passage of vortices across the wire. However, the modulation technique reported here is not dependent on the form of the bridge CPR, and so should extend to narrower, more Josephson-like bridges as well.

4.2 Analysis of the nanoSQUID switching current

With some basic analysis, it was possible to plot what the expected the nanoSQUID switching current versus the gate current should look like. This was a useful way to check the results of the experiment, as well as do some basic analysis to extract values of interest from the measured device.

4.2.1 Analysis of the nanoSQUID switching current

The analysis began by quantifying the currents traveling through the left and right constrictions. These two equations were

$$i_L = I^{\text{bias}}/2 + I^{\text{gate}}r - nI_0 \tag{4.1}$$

$$i_R = I^{\text{bias}}/2 + I^{\text{gate}}(1-r) + nI_0 \tag{4.2}$$

where i_L is the current through the left constriction, i_R is the current through the right constriction, I^{bias} was the applied bias current, I^{gate} is the applied gate current, I^R_{sw} is the current in the right constriction, I^L_{sw} is the switching current in the left constriction, I_0 is the current induced in the loop by a single fluxoid, and r is the splitting ratio of the gate current between the left and right constrictions ($0 < r < 1$). For simplicity, all currents are normalized such that $I^L_{sw} = 1$.

The next step was to define the conditions that must be met in order for a given combination of I^{bias} and I^{gate} inputs to be superconducting. The condition imposed by this requirement is simply that i_L and i_R must be less than their respective critical currents. This resulted in the following inequalities:

$$|i_L| = \mid I^{\text{bias}}/2 + I^{\text{gate}}r - nI_0 \mid < 1 \tag{4.3}$$

$$|i_R| = \mid I^{\text{bias}}/2 + I^{\text{gate}}(1-r) + nI_0 \mid < I^R_{sw} \tag{4.4}$$

Rearranging these to eliminate the absolute value terms yielded a set of four inequalities that indicated, for a given I^{gate}, the range values of I^{bias} which were valid superconducting states:

$$I^{\text{bias}} < 2(1 - I^{\text{gate}} r + nI_0) \tag{4.5}$$

$$I^{\text{bias}} < 2(I_{sw}^R - I^{\text{gate}}(1 - r) + nI_0) \tag{4.6}$$

$$I^{\text{bias}} > 2(-1 - I^{\text{gate}} r + nI_0) \tag{4.7}$$

$$I^{\text{bias}} > 2(-I_{sw}^R - I^{\text{gate}}(1 - r) + nI_0) \tag{4.8}$$

4.2.2 Visualizing the analysis

In the 2D plane of I^{gate} versus I^{bias}, each of the inequalities in Eq. 4.5 forms a boundary for the valid superconducting region as shown on the left in Fig. 4-2. By solving for all four of them, an area of this 2D plane can be solved for, as shown on the right in Fig. 4-2.

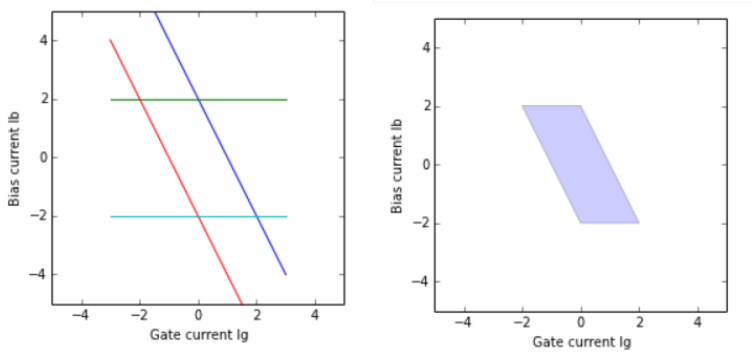

Figure 4-2: Graph plotting the solution to the nanoSQUID inequalities for $r = 0.5$, $I_0 = 0.5$, $I_{sw}^R = 1$, and $n = 0$. (left) Graph of the boundaries generated by the inequalities in Eq. 4.5. (right) Graph of the area which solves all four inequalities in Eq. 4.5

The graphs shown in Fig. 4-2 represent the solutions for all values of I^{gate} and I^{bias}, but only for the fluxoid state $n = 0$. In the actual device, the fluxoid state was allowed to change through phase slips, so therefore the inequalities had to be solved for any integer value of n, which is shown in Fig. 4-3.

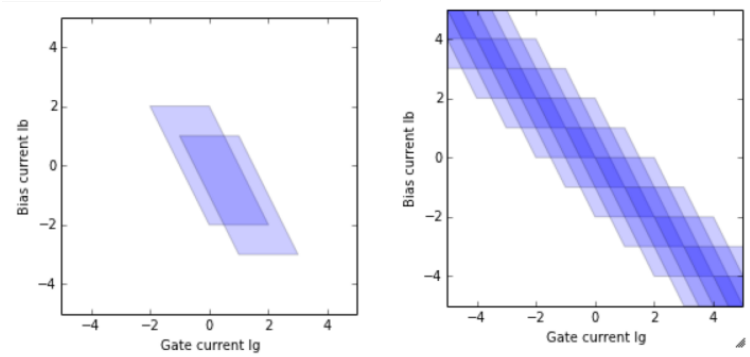

Figure 4-3: Graph plotting the solution to the nanoSQUID inequalities for $r = 0.5$, $I_0 = 0.5$, $I_{sw}^R = 1$ (left) Graph of the valid regions for $n = 0$ and $n = 1$. (right) Graph of the valid regions for all integer values of n

At this point, the solutions still do like the standard SQUID diagram, where applied magnetic flux creates a sawtooth modulation in the critical current. This was because the measurement that actually takes place in the experiment is a measurement of I_{sw}, which is equal to $I^{\text{gate}} + I^{\text{bias}}$. By instead plotting the total current $I^{\text{gate}} + I^{\text{bias}}$ versus I^{gate} as shown in Fig. 4-4, the plots better represented what the experimental results measured.

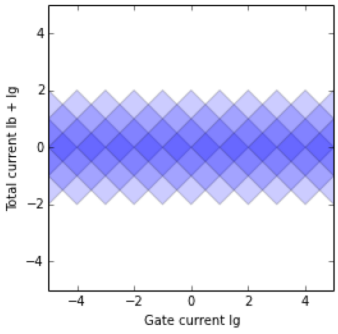

Figure 4-4: Results of the analysis of the nanoSQUID for $r = 0.5$, $I_0 = 0.5$, $I_{sw}^R = 1$ and all integer values of n, plotted with the total $I^{\text{gate}} + I^{\text{bias}}$ which better corresponds to the experimentally measured switching current.

By tuning the parameters and replotting the results, such as those in Fig. 4-5, this analysis enabled us to quickly develop a qualitative understanding of what each of the parameters did to the results. It additionally assisted us with the final analysis of the physical device.

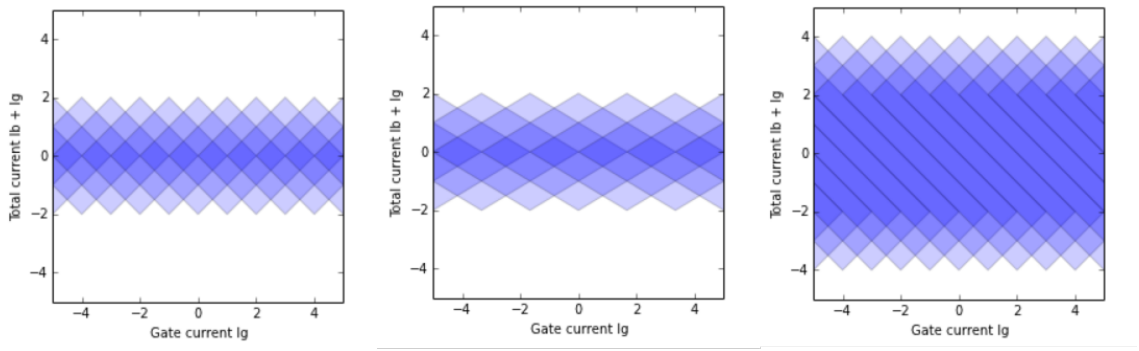

Figure 4-5: Results of the analysis of the nanoSQUID based on different parameter inputs. (left) Graph generated when the splitting ratio is $r = 0.8$. (middle) Graph generated when the flux induced current I_0 was set to $= 0.2$. (right) Graph generated when the constriction critical currents were asymmetric, such that $I_{sw}^R = 3$.

4.3 Measurements and results

To measure the nanoSQUID, we injected a fixed modulation current I_{mod} into the device, as shown in the circuit schematic of Fig. 4-1. We then measured the switching current I_{sw} of the device using current applied through the bias terminals. Specifically, the I_{sw} discussed here represents the total amount of current passing through the constrictions just before the constrictions switched to the normal state.

The nanoSQUID I_{sw} distribution measurements took place with the sample submerged in a bath of liquid helium. The sample was placed in a copper-shielded sample holder, but no magnetic shielding was used. The modulation current I_{mod} was supplied using an SRS variable battery source with two 20 kΩ resistors, one in series with each terminal of the battery source. With I_{mod} fixed, the distribution of I_{sw} was then measured by ramping I^{bias} until a nonzero voltage appeared at the I^{bias} terminal, indicating that the constrictions switched to the normal state. The current ramp for I^{bias} was provided by an arbitrary waveform generator (AWG) in series with a 10 kΩ resistor. The AWG output a 5 Vpp, 200 Hz triangle wave, corresponding to a current ramp rate of 0.3 A/s. Extended details about this type of measurement can be found in Section 7.1.1.

As we varied the injected current I_{mod}, we observed the modulation of the device I_{sw} shown in Fig. 4-6. As the device is modulated by I_{mod}, the switching current

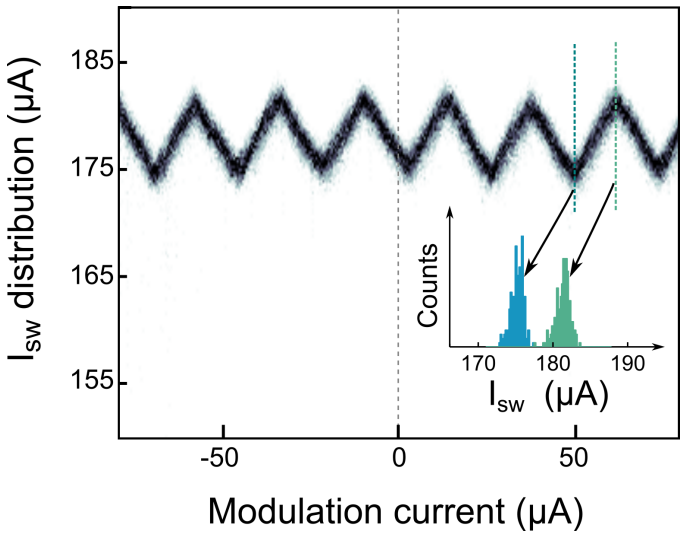

Figure 4-6: Experimental results of the nanoSQUID being modulated by injected current. Shown is the distribution of the nanoSQUID switching current (I_{sw}) varying as a function of the injected modulation current (I_{mod}). Each vertical slice of the graph corresponds to a a measurement of the I_{sw} distribution for that value of I_{mod}. (inset) Two slices showing the distribution of I_{sw} when maximally and minimally modulated by I_{mod}.

exhibits a triangle-wave pattern similar to that seen in Ref. [73], indicating a multi-valued, approximately-linear current-phase relationship. Since the nanoSQUID forms an unbroken superconducting loop, the shape of the I_{sw} modulation can be understood as follows. To maintain phase single-valuedness, current injected by I_{mod} splits between the two paths around the loop according to each path's relative inductance. One of the paths has a smaller inductance, and so carries a larger fraction of I_{mod}. The resulting imbalance of current flowing through the two constrictions reduces the total I_{sw} of the device. To make this analysis clearer, we can break up the contributions of I_{mod} into two constituent currents: I_{sym}, the portion of the modulation current which is divided equally between the two constrictions, and I_{loop}, a circulating current which has equal and opposite values through each constriction. These components are shown in Fig. 4-1. Since our measurement of interest, I_{sw}, is defined as total amount of current passing through both constrictions when they switch, the measurement of I_{sym} is automatically absorbed into I_{sw}, leaving only I_{loop} to affect the value of I_{sw}. Thus, we can view the effect of I_{mod} as solely producing a loop current,

similar to how a magnetic field would induce a loop current in a conventional SQUID.

The periodicity of the I_{sw} modulation arrives from the London quantization condition, which enforces an integer number of fluxoids in the loops. When I_{mod} produces enough circulating current, the device can counteract the induced current by allowing a fluxoid in through one of the constrictions. Thus, the adjacent maxima of the triangle wave shape correspond to I_{mod} inducing a circulating current equivalent to one fluxoid. One feature of note is that the distribution is not at an extrema when I_{mod} is zero. This distribution shift can be explained by a 4 % variation in I_{c} between the two constrictions. We additionally verified that the shape and form of the current modulation matched that of magnetic modulation, by applying a magnetic field to the device.

4.4 Results analysis

By analyzing the results, we extracted several parameters from the device, including the total device inductance, the kinetic inductance per square, the total inductance of each current path, the loop current induced by each fluxoid, and the splitting ratio of I_{mod} between each constriction. The film's total inductance can be calculated by $L_{\mathrm{tot}} = \Phi_0/(2I_{\mathrm{sw}}^{\mathrm{mod}})$, where $I_{\mathrm{sw}}^{\mathrm{mod}}$ is the depth of modulation of the device switching current and corresponds to half the current induced by a fluxoid. From our experimental results in Fig. 4-6 we found an $I_{\mathrm{sw}}^{\mathrm{mod}}$ of $5.9 \pm 0.1\,\mu\mathrm{A}$, corresponding to a total inductance of $175 \pm 3\,\mathrm{pH}$.

To extract the material's kinetic inductance, we assumed that the kinetic inductance per square was uniform over the entire patterned film. Kinetic inductance is expected to increase with current density [78], but such increases are small except within a few percent of the critical current. It is likely this assumption was violated in the vicinity of the constrictions [79], but the constrictions represent a small fraction of the total device inductance. Since the total inductance is just the summation of the geometric and kinetic contributions, the film's kinetic inductance per square was then $L_{\mathrm{k}} = L_{\mathrm{tot}} - L_{\mathrm{g}}$, where the geometric inductance L_{g} was numerically calculated, giving

a value of 16.7 pH. We then numerically calculated that there were 60.1 squares in the loop, resulting in a kinetic inductance per square of $2.6 \pm 0.1\,\mathrm{pH}/\square$. This sheet inductance was larger than the value predicted by $L_\mathrm{k} \approx \hbar R_\mathrm{s}/\pi\Delta_0 = 1.5\,\mathrm{pH}/\square$, where R_s is the sheet resistance just above T_c and Δ_0 is the superconducting gap energy at zero temperature [29]. This difference likely due to degradation of the film during the fabrication process, increasing R_s or decreasing the RRR. Lastly, by measuring the periodicity of the triangle pattern, we found that I_mod split between the two constrictions such that only $2.0 \pm 0.1\,\%$ passed through the constriction on the left in Fig. 4-1. This contrasted with our expectation that $8\,\%$ of I_mod would pass through that constriction.

4.5 Minimizing L_k

We also fabricated nanoSQUID devices with a number of other designs. One of these in particular was designed an effort to reduce L_k as much as possible. The design we chose was an hourglass-shape, shown in Fig. 4-7, which had very small number of total squares in the loop, resulting in a minimum amount of kinetic inductance. Ideally, we wanted to reduce L_k enough such that the amount of current induced by each fluxoid ($I_{\Phi_0} = \Phi_0/L_\mathrm{k}$) was greater than the critical current of the constrictions. This goal can be restated as we wanted $I_{\Phi_0}/I_\mathrm{c} > 1$. Reducing L_k would have increased I_{Φ_0} while nominally leaving I_c the same. This would have allowed us to create a nanoSQUID which could not trap any flux, and thus remove any chance for hysteresis in the device since it would only have one state – the number of fluxoids n in the device would always be zero.

However, there was a fundamental problem with trying to reduce L_k to below this level: in a constant-thickness Dayem-type bridge, the current path through a single constriction – of even the most optimized geometry – always results in enough inductance such $I_{\Phi_0}/I_\mathrm{c} \approx 1$. This is explained thoroughly in Ref. [77], and is demonstrated schematically in Fig. 4-8. As a result of this L_k-I_c relation, a loop made from a constant-current thickness film and two constrictions always had a I_{Φ_0}/I_c ratio of

at least two, and thus could always store fluxoids. Changing the thickness of the material does not help–for instance, if the thickness is doubled, L_k drops to half its previous value and I_{Φ_0} doubles, but simultaneously I_c is doubled, leaving the I_{Φ_0}/I_c ratio the same. The only way around this L_k minimum is to use multiple thickness of superconducting material – this type of constriction is called as a variable-thickness bridge in Ref. [77].

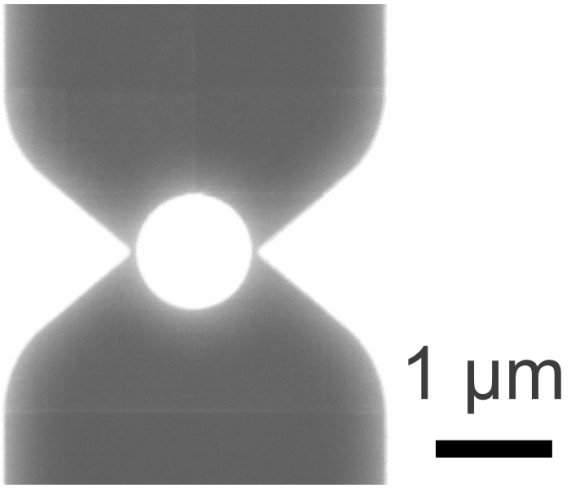

Figure 4-7: Hourglass nanoSQUID geometry designed to be as low-inductance as possible.

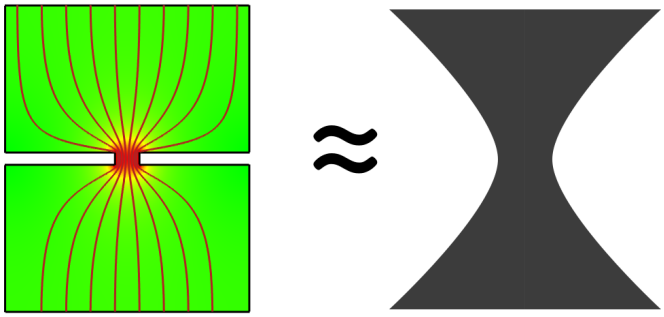

Figure 4-8: Figure showing how a bridge which nominally comprises only a few squares actually has more squares due to the path of the current flow. On the left is a simulation of current flowing across a narrow constriction. It appears to be about 1 square in total, but the simulation reveals it is more than 3 squares total. This is due a majority of the current taking an hourglass path, shown by the streamlines on the left, and represented geometrically on the right.

4.6 Variations in the behavior of the nanoSQUID

Before performing a full characterization on the device shown in Fig. 4-1(a), we tested a number of other devices and found that the output characteristics of the nanoSQUID depended highly on the material from which they were fabricated, and also on the uniformity of the constrictions.

4.6.1 Material dependency

We fabricated devices both from not only thin-film niobium (Nb) as described above, but also thin-film niobium nitride (NbN). Generally speaking, these materials are very similar: they are both type-II BCS superconductors, they have relatively high bulk T_c values ($\sim$9 K for Nb, $\sim$16 K for NbN), and their nominal critical current densities are on the same order [80]. However, when it came to their operation as nanoSQUIDs, their output was qualitatively different.

Shown in Fig. 4-6 and Fig. 4-9 are the results from measuring two different nanoSQUIDs, one which was fabricated from a Nb film, and the other which was fabricated from a NbN film. As can be seen in Fig. 4-6, the output of the Nb device did not show any of the underlying fluxoid-state structure like can be seen in Fig. 4-9. Only the uppermost edges of the valid regions can be seen in the Nb device. However, in the NbN device, this underlying structure is visible–the edges of the triangle-wave shape which constitutes the valid-region border extend beyond the border. With this device, for a given I^{gate} value there can be several distinct distributions of of I_{sw}.

The presence of this underlying structure indicates that the device switched (constrictions became hotspots) when fluxoids entered or exited the loop. This process is shown Fig. 4-10. When measuring the nanoSQUID, the gate bias I^{gate} was fixed, and then the I^{bias} current was ramped. This trajectory through the I^{gate}-I^{bias} is shown by the dashed blue line in Fig. 4-10. If, for example, the device started in state $n = 2$ (point A in Fig. 4-10), when it reached the edge of the $n = 2$ state (point B in Fig. 4-10), there would be enough current in the loop such that one of the constrictions would be biased exactly at its critical current. At this bias current,

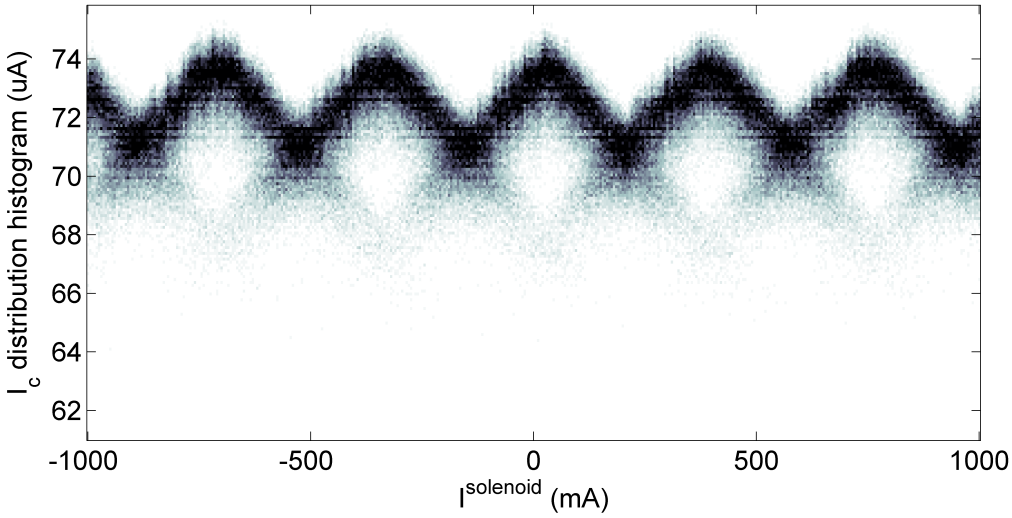

Figure 4-9: Measurements of the switching distributions for a NbN nanoSQUID. This nanoSQUID was biased using an induced magnetic field from a solenoid instead of current-biased.

the superconducting state is suppressed (due to $J \approx J_c$ in the constriction), and it becomes energetically favorable for fluxoids to leave the loop. As this fluxoid is leaving, however, there are two scenarios that can occur, dependending on the material from which the nanoSQUID is made. The first scenario is that the fluxoid exits out (either coherently, through a phase slip, or a vortex), superconductivity is restored in the constriction, and $n = 1$ now. The bias current I^{bias} can continue to be increased without a voltage appearing on the device until it reaches the edge of the $n = 1$ state (point B in Fig. 4-10). Once at this border, there are no more valid states for the nanoSQUID to relax into, and so the constrictions become normal voltage appears on the device if I^{bias} is increased.

The second scenario is that the fluxoid exits out (again either coherently, through a phase slip, or a vortex), and the self-heating caused by the passage of the fluxoid causes so much energy dissipation that a hotspot forms in the nanowire constriction [63]. This is represented by the device switching at point B in Fig. 4-10 – even though there is a valid state to switch into ($n = 1$), the dynamics of the fluxoid dissipation create a hotspot. The presence of this hotspot has a long thermal lifetime and so before the first hotspot can cool, all the current is diverted to the other constriction

where it causes a second hotspot. The result is that both constrictions switch to the normal state and a voltage appears.

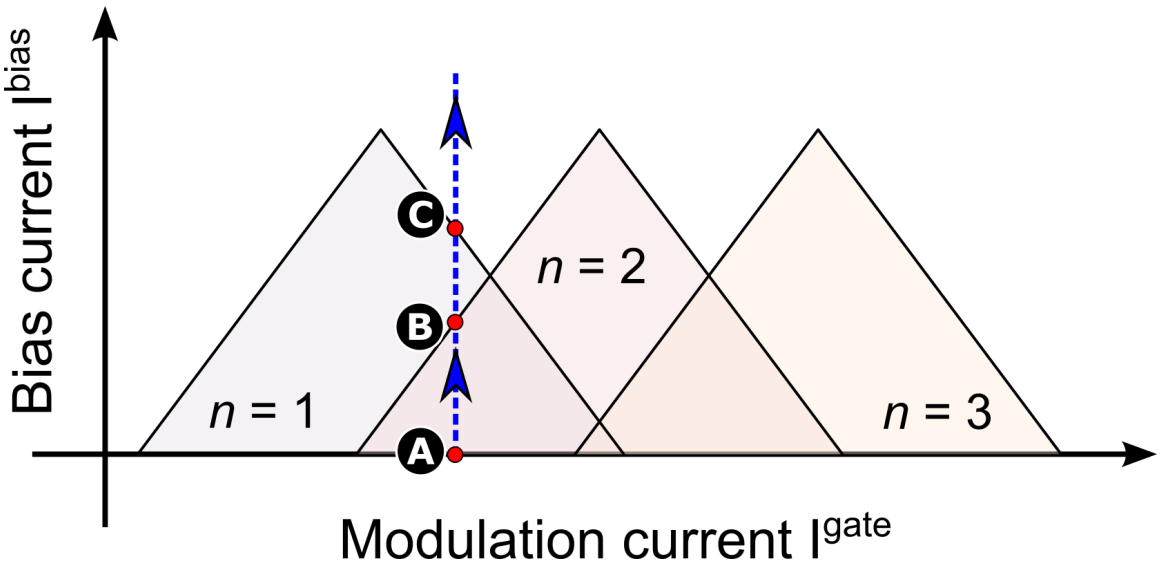

Figure 4-10: Diagram showing the nSQUID states as I^{bias} is increased. First, I^{gate} is set and I^{bias} is zero (point A) – the device begins in the state $n = 2$. Next, I^{bias} increased until it reaches the boundary of the $n = 2$ state (point B). At this time, if the device is hysteretic, it may create a hotspot and latch. Otherwise, the device will transition to the $n = 1$ state by ejecting a fluxoid, and as I^{bias} is further increased it exits the valid region and forms a hotspot (point C).

The sheet resistivity of the nanoSQUID thin film determines which of these two scenarios takes place [81] [82]. In lower-resistivity films like the Nb film, the thermal energy dissipation that is incurred by the passage of the fluxoid is quickly drawn out into the banks surrounding the constriction, and even if it causes a Joule-heated region, this hotspot is quickly quenched because the Nb constriction is very low-resistance even when normal and cannot easily sustain a hotspot. However, in the NbN film this self-shunting process cannot occur due to the high sheet resistivity. If enough energy is dissipated to cause a hotspot, this hotspot will be very effectively self-Joule-heated by the current flowing through the high-resistance NbN constriction.

4.7 Use of the nanoSQUID geometry as an L_k metrology tool

This device has proven to be a convenient metrological tool for extracting the kinetic inductance of superconducting thin films since it only requires low-frequency DC currents. The design of superconducting devices which have kinetic inductances often requires characterization of that inductance to achieve optimal device performance, for example tuning the L/R times of superconducting nanowire single photon detectors or nTrons. Typically, these L_k values are measured by microwave reflection measurements using a network analyzer [79], or by measuring the magnetic penetration of the film using two-coil mutual inductance measurements [83]. By patterning a current-modulated nanoSQUID on the same film as these devices, it instead becomes possible to directly extract the thin-film inductance per unit square using only low-frequency currents–no microwave characterization or tunable magnetic fields are required.

In summary, we have demonstrated the first modulation of a nanoSQUID using injected current rather than an applied magnetic field. By adding current asymmetrically to the two constrictions of the nanoSQUID, we were able to modulate the switching current of the device. This modulation method is a direct analog to inducing a loop current by applying a magnetic field. This technique has immediate applications as a closed-loop feedback mechanism for scanning-SQUID microscopy. Although the device described here has a large total inductance, and thus low sensitivity when operated as a magnetometer, this method of modulation should generalize to nanoSQUIDs of any design.

Chapter 5

The nanocryotron (nTron)

Superconducting devices are vitally important in several fields such as magnetic-field sensing, quantum and classical computing, photon sensing in communications, and astronomy. These areas require sophisticated electronics for control, amplification, and related information processing. To address the challenges posed by these application areas, superconducting device families such as Rapid Single-Flux Quantum (RSFQ) electronics have been developed for the past several decades as possible scalable electronics technologies. But all these efforts have been based fundamentally on the Superconducting Quantum Interference Device (SQUID). The SQUID provides the non-linearity and gain that is fundamentally required in order to realize sensing and amplification in electronic systems.

Unfortunately, systems based on SQUIDs (including RSFQ electronics) suffer from major disadvantages which render them impractical for a variety of applications and environments. These disadvantages include low gain, high sensitivity to magnetic fields, difficulty in driving large-impedance loads, and challenges in fabrication. Devices based on the SQUID must be biased with substantial amounts of current, but are limited in how much output current they can source. The result is a device with low gain. In addition, the requirement that these devices include Josephson junctions – ultrathin tunneling barriers – renders them notoriously sensitive to fabrication imperfections. A variation of an atomic layer in barrier thickness can radically change the operating point of a device. Finally, SQUIDs are intrinsically the most sensitive

magnetic field sensors available. This feature is a blessing and a curse, as SQUID-based computing devices must be heavily shielded in order to operate. On top of these issues, the challenge in reproducibly fabricating high-Tc Josephson junctions has prevented SQUID-based active electronic devices with critical temperatures above $\sim$15 K from being developed. In large part, the practical concerns outlined here have been a barrier to the broader application of superconducting systems. By circumventing the usage of SQUIDs and Josephson junctions entirely, the devices described in this chapter overcome these impediments while at the same time operating with characteristics that make them suitable for integration with existing SQUID-based systems.

The text that follows is a reprint of work that was originally published in *Nano Letters* [84]. Reprinted with permission from McCaughan, A. N. and Berggren, K. K. A Superconducting-Nanowire Three-Terminal Electrothermal Device. *Nano Lett.* 2014, 14 (10), 5748-5753, copyright 2015 American Chemical Society.

5.1 Challenges of superconducting circuitry

Superconducting circuits have a long history, beginning 50 years ago with Dudley Buck's invention of the cryotron [32] [77]. The cryotron was a device composed of intertwined superconducting wires, in which a gate wire induced a magnetic field that would switch the channel wire between a superconducting and resistive state, thus enabling active control of the channel resistance. Since then, a number of two, three, and four terminal superconducting logic devices have also been introduced [36] [33] [34] [38] [35] [85], but were not developed beyond basic characterization. One exception has been the Josephson junction, which has found widespread success in a variety of fields, thanks in large part to their $>$100 GHz operating speeds and sub-aJ/bit power consumption (9, 10). However, the fundamental property that makes Josephson junctions attractive–their manipulation of single flux quanta–also limits the scope of their application, especially in areas that require driving large impedances, fanning out digital signals, or operating in noisy magnetic environments. Additionally, building small-scale circuits with Josephson junctions requires either

access to a foundry, or very well developed processes as a junction's key parameters depend sensitively on sub-Angstrom-scale thickness variation of the tunneling barrier.

To address some of the challenges faced by superconducting circuitry, we have developed the nanocryotron (nTron). Similar to the cryotron, the nTron uses an input gate current to induce changes in the resistivity of the channel. However, unlike the cryotron, the nTron uses a localized, Joule-heated hotspot [10] [11] [12] formed in the gate to modulate current flow in a perpendicular superconducting channel. The rapid transition to a highly resistive state enables the nTron to drive large impedances ($>100\,\mathrm{k}\Omega$) and fanout to multiple devices (>4). Additionally, although the input current sensitivity is sufficient to detect single flux quanta (1-σ grey zone of 66 nA), the nTron does not require superconducting loops and so can circumvent the issue of flux trapping in noisy environments. Furthermore, because the hotspot effect occurs in all known superconductors [86] [87], we expect the design to be extensible to other materials, providing a viable path to digital logic, switching, and amplification in high-temperature superconductors. We have characterized the nTron, matched it to a theoretical framework, and demonstrated a half-adder circuit made from nTron logic gates. In addition, we have used it as a low-jitter ($<25\,\mathrm{ps}$) digital amplifier for superconducting nanowire single-photon detector (SNSPD) pulses. Initially, the nTron will most likely find use in driving digital storage address lines in Josephson-junction-based computers, in amplifying SNSPD pulses (e.g. for feed-forward applications in photonic quantum computing), and possibly in other cryogenic applications requiring small-signal discrimination with sub-25-ps timing accuracy and moderate (e.g. below 1 GHz) repetition rates.

5.2 nTron device description

The nTron is a thin-film superconducting device with a gate, a drain, and a source terminal, all connected contiguously with no junctions (Fig. 5-1A). As shown in Fig. 5-1B, the gate terminal perpendicularly intersects the side of the channel via a narrow bottleneck called the choke. Current entering the gate terminal, I^{gate}, switches the

phase of the choke from the superconducting (S) to the resistive (R) state. The S→R phase transition is induced in the ∼15-nm-wide choke by locally exceeding the critical current density J_c of the niobium nitride film. In turn, the resistive phase of the choke induces a nonlinear suppression of the critical current of the channel, I_c^{channel}. The resulting dependence of the channel critical current on the gate input current, $I_c^{\text{channel}}(I^{\text{gate}})$, enables the nTron to produce robust switching and gain. Fig. 5-2 depicts the characterization of a non-inverting nTron amplifier circuit. The observed form of $I_c^{\text{channel}}(I^{\text{gate}})$ is ideal for a digital logic family: nearly zero modulation of the channel critical current was seen until a threshold of gate current, $I_c^{\text{gate}} = 2.9\,\mu\text{A}$, was reached. Exceeding that threshold produced a $30.5 \pm 0.5\,\%$ reduction in I_c^{channel} from its base value $I_c^{\text{channel}}(0) = I_{c0}$. This reduction occurred coincidentally with a nonzero resistance measured at the gate terminal, indicating that the formation of the resistive hotspot in the choke was responsible for the suppression of I_c^{channel}. Bias currents greater than $0.9\ I_{c0}$ resulted in undesired behavior such as photon- and noise-induced hotspot generation, while operating the devices at lower bias currents improved their robustness to source noise and typical ambient magnetic noise.

5.2.1 Fabrication of the nTron

The nTrons described here were fabricated from a contiguous 10 nm film of niobium nitride (NbN) deposited on a single 2 inch R-plane sapphire wafer. For the simulation, parameters extracted from the device and the film from which it was fabricated included (1) the device critical current density $J_c = 6.6\,\text{MA/cm}^2$, (2) the critical temperature $T_c = 12.6\,\text{K}$ and its transition width $\Delta T_c = 1.1\,\text{K}$ of the film, and (3) the device sheet resistance $R_s = 285\,\Omega/\square$. For patterning, we spun on 50 nm hydrogen silsesquioxane (HSQ) resist and exposed the device patterns in a 125 kV Elionix electron-beam lithography tool. We then etched the NbN around the patterned HSQ to complete the nTron fabrication. Contact pads were added by photolithography of 1-micrometer-thick Shipley S1813 photoresist, followed by evaporation of 10 nm Ti and 25 nm Au and then liftoff. Electrical connections between the sample mount and device contact pads were made using aluminum wirebonds. For all experiments de-

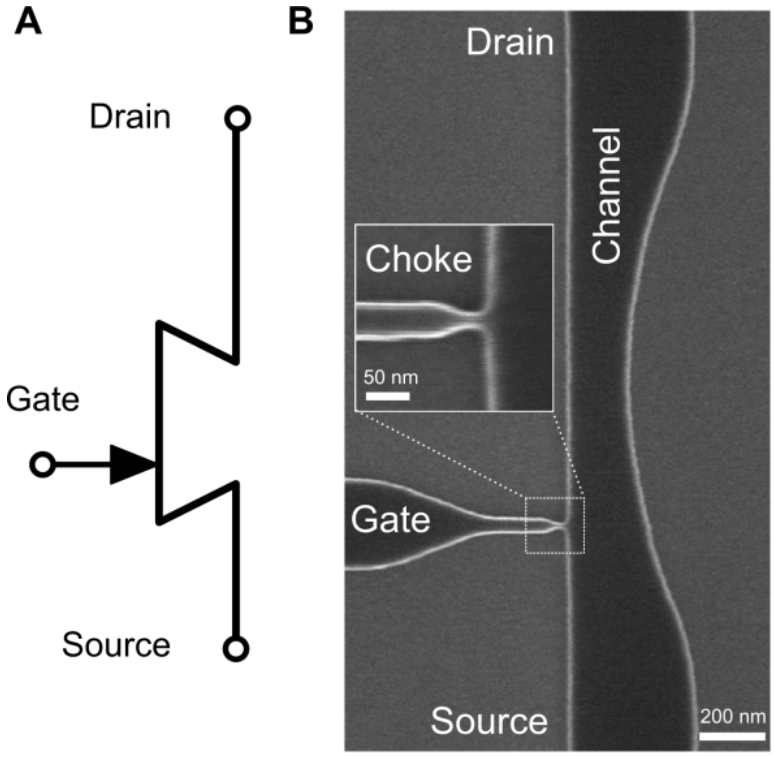

Figure 5-1: (A) Three-terminal circuit symbol. The position of the gate arrow denotes the location of the choke relative to the narrowing of the channel. (B) SEM of a fabricated nTron, the inset depicts a close-up of the choke, the area in which the resistive hotspot is first formed.

scribed here, samples were submerged in a bath of liquid helium. Experiments took place in ambient magnetic conditions.

5.3 nTron operation

During operation, the nTron moves between three distinct states (Fig. 5-3). Under the bias condition $I_c^{\text{channel}}(I_c^{\text{gate}}) < I^{\text{bias}} < I_{c0}$, when a logical LOW ($I^{\text{gate}} < I_c^{\text{gate}}$) is fed into the gate input, the channel remains superconducting, and when a logical HIGH ($I^{\text{gate}} > I_c^{\text{gate}}$) is input, the channel becomes resistive. In this context, we used the nTron as a discrete digital element for performing logical functions. Digital operation was reproduced for load impedances of 50 Ω, 100 Ω, 1 kΩ, 10 kΩ, 100 kΩ, and the open-circuit case. In the open-circuit case, the bias condition of $I_c^{\text{channel}} = 0.85 I_{c0} = 90\,\mu\text{A}$ yielded an output voltage of 8.1 V and an input-output isolation of 42.7 kΩ. For the

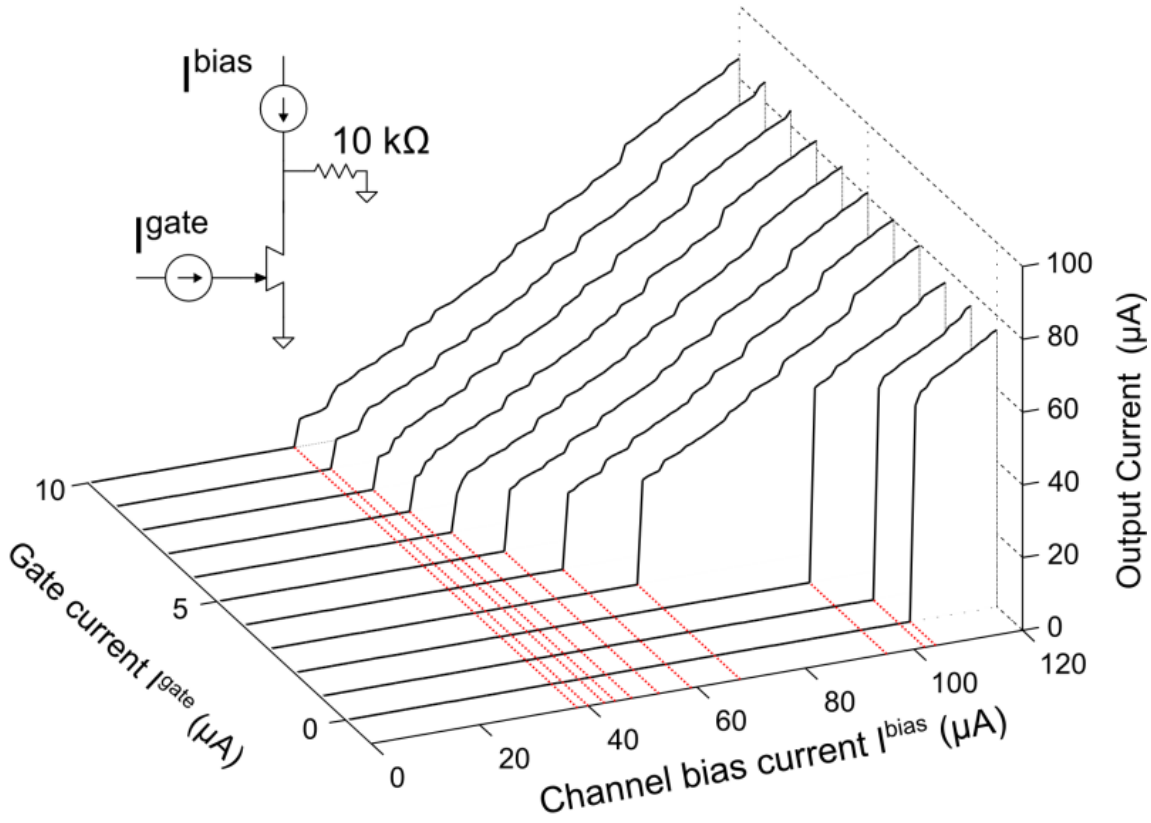

Figure 5-2: Circuit schematic and output characteristics for an nTron in a non-inverting amplifier configuration. I^{gate} was fixed and I^{bias} was swept from 0 to 120 µA.

10 kΩ case, the leakage current into the load during the digital LOW state was less than 0.4 nA, within the measurement error of our testing apparatus.

Fundamental to the operation of the nTron is the phenomenon of localized critical-current suppression, wherein a hotspot sustained by Joule heating suppresses the superconducting characteristics of the nearby material. Phonons and quasiparticles diffuse from the hotspot to the surrounding superconductor where they interact with the superconducting bath, depleting the local Cooper pair population as they relax back to equilibrium [88]. In the case of thin-film NbN, out-diffusion of hot electrons is the primary means of thermal energy transfer from the hotspot to the surrounding material [89] [90]; the characteristic diffusion coefficient for non-equilibrium electrons has been measured [24] to be 45 nm^2/ps.

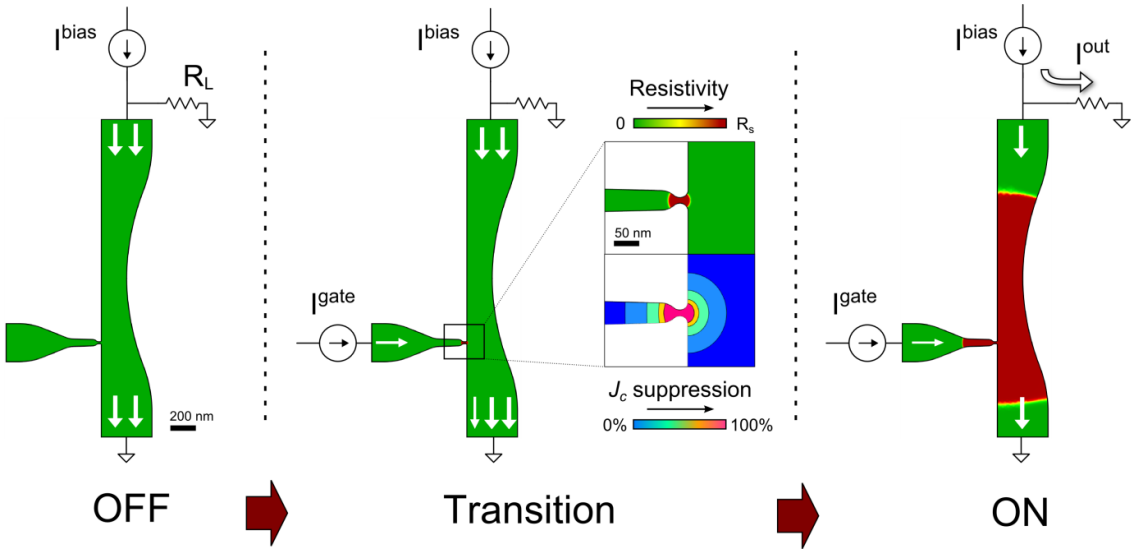

Figure 5-3: Numerical simulation of the nTron depicting the three states of operation. OFF state: The device is fully superconducting, bias current is drained through the channel to ground. Transition state: Current is added to the gate input, forming a resistive hotspot which locally suppresses superconductivity. (inset, upper) Closeup of the resistive hotspot forming in the choke. (inset, lower) Contour map of J_c suppression extending from the hotspot. From inner to outer, the bands represent reductions in J_c by 0 % (blue), 25 % (light blue), 50 % (green), 75 % (orange), and ≥99 % (magenta). ON state: The critical current of the channel is reduced sufficiently that the bias current triggers the formation of a resistive hotspot in the channel.

5.4 Simulation and design parameters

To corroborate our measurement results and facilitate future designs, we simulated the nTron device geometry using an established theoretical framework, the two-temperature model [55], which uses an effective electron temperature T_e to represent the temperature of populations of quasiparticles and Cooper pairs. The simulation used no free parameters–we instead employed measurements from the device as well as empirical parameters for thin-film NbN found in the literature [90] [24]. The simulation results showed that when a hotspot was formed in the choke of the nTron, the effective electron temperature T_e of the surrounding ∼100 nm was increased. This temperature increase corresponds to a decrease in J_c over the same radius, effectively reducing the total channel critical current. As a result of the hotspot formation, the calculated I_{c0} was reduced by 28 % of its original value, closely matching the mea-

sured value of 30.5 %. Additionally, just above I_c^{gate} the resistance of the simulated gate hotspot was 823 Ω, which was comparable to the measured resistance of 832 Ω.

The nTron consists of a single layer of thin-film superconducting material, so its 2D geometry defines its operation. The layout of the device has several essential design elements, resulting in a large design parameter space in which future implementations may be optimized. The most critical design element is the size and location of the choke region, which is the point of highest current density for the gate input current and is where the hotspot first forms $I^{gate} > I_c^{gate}$. The choke hotspot is the key to the nTron's functionality; it proximitizes the nearby superconducting channel and induces a suppression of the critical current in that area. The width of the choke defines the input current level required for the gate hotspot to form and produce a logical HIGH, which can be approximated by $I_c^{gate} = J_c d w^{choke}$, where J_c is the critical current density, d is the substrate thickness, and w^{choke} is the width of the choke. As we observed in our simulation, the formation of the hotspot only suppressed J_c within approximately one diffusion length L_D (∼100 nm for thin-film NbN) of its perimeter. Accordingly, the width of the channel must be on the same length scale for the hotspot to generate a sharp dropoff in $I_c^{channel}$. The shape of the channel presents another design parameter, as it affects the growth of the hotspot after switching. The shallow swept-curve shown in Fig. 5-1 controls the direction of the hotspot growth–it will preferentially grow towards narrower regions due to the higher current density–but does not limit the maximum growth of the hotspot. However, a larger variation of the width along the channel can produce an nTron with a constrained hotspot size, which may be desirable in some applications.

5.5 Digital applications and characterization

To demonstrate the suitability of the nTron for digital applications, we used it to build AND/OR/NOT/COPY gates (Fig. 5-4), and from those constructed a half-adder (Fig. 5-5). We also performed a number of additional characterization experiments to demonstrate RF operation, sensitivity, and robustness of the nTron.

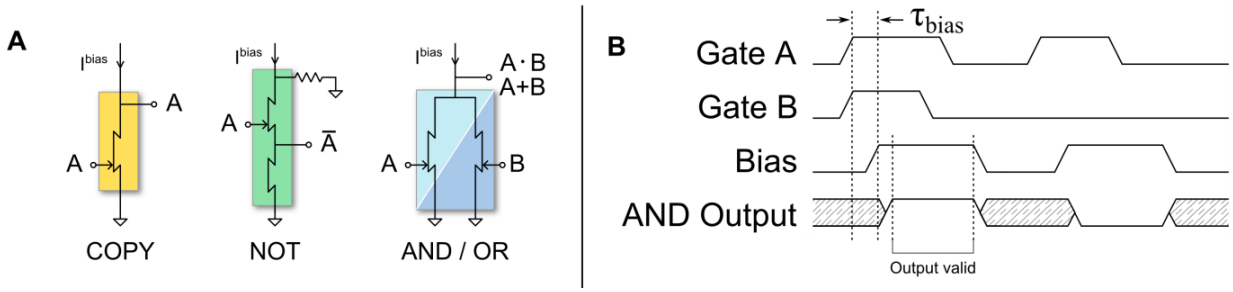

Figure 5-4: Digital gates based on the nanocryotron. (A) Schematic of a set of universal logical gates from the basic three-terminal nTron. The AND gate and OR gate are topologically identical, and are only differentiated by their bias conditions. AND/OR/COPY were constructed purely from nTrons, while the NOT gate required a shunt impedance for the bias (in this case a resistor). (B) AND-gate timing diagram for pipelined logic propagation. Once gates A and B have valid inputs, the bias current is enabled and the resulting output can be used as an input for the next stage. τ_{bias} denotes the propagation delay due to the low-rate bias electronics.

5.5.1 nTron logic gates

Fig. 5-4A shows the COPY/NOT/AND/OR gates. All of the gates required only one or two nTrons, except for the NOT gate which used an additional 330 Ω shunt resistor and another nanowire constriction in addition to a single nTron. The COPY gates operate similar to a non-inverting version of the FET: when a logical HIGH ($I^{\text{gate}} > I_{\text{c}}^{\text{gate}}$) is input to the gate, the channel becomes resistive and the channel bias current is diverted into the output, generating a HIGH output. When a logical LOW ($I^{\text{gate}} < I_{\text{c}}^{\text{gate}}$) is input to the gate, the channel bias current drains directly to ground without generating a resistive region in the channel. As a result, the output is effectively shorted to ground and is thus a logical LOW. The AND and OR gates are the result of putting two nTrons in parallel. In the case of the OR configuration, when either gate input received a logical HIGH, the combined $I_{\text{c}}^{\text{channel}}$ of the two nTrons would be reduced enough such that the channel bias current would switch the device. The AND configuration was achieved by biasing the channel below this point, to the point where the combined channel critical currents only dropped below the bias current when both gate inputs were HIGH. This topological equivalence between the AND and OR gate opens the possibility to dynamically reprogram an otherwise fixed logic circuit.

For the NOT gate, when a logical LOW was input, I_c^{channel} was greater than the bias current, allowing all the current to pass through it without switching. However, the pulldown constriction critical current was designed to be smaller than the full channel bias current, which caused the pulldown constriction to switch and diverted the excess current into the output, producing a logical HIGH out. In the case of a HIGH input, the suppressed $I_c^{\text{channel}}(I^{\text{gate}})$ was less than the bias current. As a result, the nTron transitioned to the ON state, and current was diverted to ground through the shunt resistor. The pulldown constriction served to tie the output to ground, even in the presence of the unavoidable small current leaking through the resistive channel.

5.5.2 The nTron half-adder

The half-adder experiment consisted of fabricating several individual gates on a single chip, connecting them via wirebond, and biasing them in a pipelined manner to perform the summing computation. We built a custom 16-channel combined ADC and DAC system to handle the multiple gate and bias inputs, and to read out their bias voltages. For the gate inputs and channel biases, current sources were approximated using the DAC voltage channels in series with 100 kΩ resistors. The ADC channels were used to record the status of each gate's output. Due to the pipeline-propagation of the half-adder, in combination with the low-rate DAC/ADC system, the computation of the half-adder outputs required approximately 0.8 s to complete. No external amplification was necessary for readout, and the lower bit and carry bit and generated 38.8 mV and 17.0 mV respectively across their 330 Ω load resistors. The sampling rate of the room-temperature electronics setup limited the computation rate to 1.2 Hz. In this mode, longer time scales present more opportunity for noise to erroneously switch the devices. Despite this disadvantage, exercising the circuit over 4,000 cycles spanning 55 minutes the circuit produced only seven errors.

We operated the half-adder in a latching, pipelined fashion, where valid inputs were translated into valid outputs for the next stage only upon the enabling of the gate bias current (Fig. 5-4B). After the computation was completed and the final

outputs were recorded, all the input and bias currents were shut off to unlatch the gates and reset the computation. For the purposes of this demonstration, operating in the latching regime enabled us to tolerate potentially large fabrication defects in these first devices. In the latching regime, variations between the OFF-state input impedances of the gates did not matter because each stage was able to drive arbitrarily large input impedances in the next stages–to operate the nanowires in a non-latching regime, output impedances must be more carefully controlled [52]. No electrical or magnetic shielding was necessary; the nTron does not require fully-superconducting loops to function, and so resistive wirebonds and contact pad connections were used to prevent flux trapping during operation.

5.5.3 Measuring the threshold sensitivity of the nTron

We tested the nTron as a comparator to characterize the current sensitivity of the gate input (Fig. 5-6). The experimental setup was the same as that of the 10 MHz eye diagram characterization, only differing in the current bias and readout scheme. First, we applied a 52.8 µA bias current to the channel in order to prime it for transition from the ON to OFF state when I^{gate} exceeded I_c^{gate}. We then ramped the gate current from 0 to 15 µA at a rate of 16.7 nA/µs, recording the output current through the load resistor RL on a 1 GHz oscilloscope. We repeated this experiment 11,000 times, plotting the results as a histogram (Fig. 5-6B). From the histogram, we found a mode switching value of 2.91 µA with a 1-σ grey zone of 66 nA.

5.5.4 Measurement of a pseudo-eye-diagram at 10 MHz

To characterize the device at higher frequencies than the operating frequency of the half adder experiment described above, we input a 10 MHz square wave into the device to generate a modified eye diagram. With a 1.46 kΩ output load, the nTron was able to convert a 3.10 ± 0.02 µA input square wave into a 62.7 ± 1.2 µA output square wave, corresponding to a signal gain of 20.2 (even though this circuit is a digital comparator, in this chapter we use the term gain to describe the ratio of

the output current to the gate input current). At the sampling point, the signal-to-noise ratio was 168. Applying a magnetic field perpendicular to the device plane, swept between ±7.4 mT, had no observable impact to the eye diagram characteristics. Additionally, we measured the input-level sensitivity by operating the device as a current comparator, measuring an I_c^{gate} of 2.91 µA with a 1-σ grey zone of 66 nA.

Using the experimental setup shown in Fig. 5-7A, we generated a 10 MHz eye diagram for the nTron digital amplifier. We accomplished this by sending one current square wave into the device channel, and one current square wave into the gate port (delayed by approximately 10 ns relative to the channel square wave). The channel square wave primed the nTron to switch from the ON to the OFF state, such that when the rising edge of the gate square wave arrived, the nTron switched, generating an output current which was read out by the scope. Note that the eye diagram shown in Fig. 5-7B is modified from a standard diagram: it only shows the transitions LOW→HIGH and HIGH→LOW, and omits the LOW→LOW transition as well as the HIGH→HIGH transition. The testing was performed in the latching regime, meaning the bias was shut off each cycle, eliminating the possibility of a standard HIGH→HIGH transition. The LOW→LOW transition was also omitted, as the square-wave generator used for this test did not have a pseudo-random bit stream (PRBS) function. The two shown transitions were captured by allowing the oscilloscope to trigger on both the rising edge and falling edge. This demonstration was primarily qualitative, meant to show the large signal-to-noise ratio at 10 MHz-future work will include the high-frequency analysis of the nTron, as well as the generation of a more typical (and lower SNR) eye diagram, covering both the latching and non-latching regimes with all four transitions.

5.5.5 Integration with a superconducting nanowire single-photon detector

We tested the nTron's ability to amplify pulses as well as established an upper bound to its jitter by using it to read out a superconducting nanowire single-photon de-

tector [50] (SNSPD). When detecting a photon, SNSPDs produce millivolt-scale microwave pulses with sub-100 ps rising edges. The integrated device used these pulses as input into the gate of a nTron amplifier. We monolithically fabricated the SNSPD and nTron on the same film within a 100 μm^2 area, connecting the SNSPD output to the gate of the nTron. Our circuit design (Fig. 5-8) enabled us to bias each device separately, as well as simultaneously read out the unamplified SNSPD pulses and nTron-amplified pulses for comparison. When the SNSPD was illuminated with a 1550 nm sub-picosecond laser, output pulses were produced from both devices concurrently. We compared the SNSPD output to the nTron-amplified output, and observed a factor of 2.9 increase in signal pulse amplitude. This increase in amplitude proportionally increased the slew rate of the rising signal edge, resulting in a reduced jitter when measured by our scope. This test also served to demonstrate the non-latching operation of the nTron: after the pulses were produced, both devices reset on their own within $\sim$10 ns, without any modification of the bias conditions. Jitter was measured between the sync edge of the sub-ps laser and the rising edge of each device's output pulses. As can be seen in Fig. 5-8, the unamplified pulses had a full-width half-max jitter of 41.3 ± 0.3 ps, while the corresponding nTron-amplified pulses showed a reduced full-width half-max jitter of 23.8 ± 0.2 ps. This value of 23.8 ps is the total system jitter, and thus also sets an upper bound to the nTron input-to-output device jitter, which is presumably smaller, as state-of-the-art NbN SNSPDs [91] alone produce jitters on the order of 20-40 ps.

As shown in Fig. 5-9, the SNSPD and nTron pulse amplifier were integrated as single circuit. Current biasing was accomplished through the use of inductive splitting, where the inductance was provided by the kinetic inductance of the nanowires. The SNSPD nanowires had a width of 60 nm, and the inductor nanowires had widths of 200 nm. The entire circuit occupied an area of approximately 100 μm^2. The 50 Ω lines were high-frequency coaxial cable running between the sample and room-temperature electronics. During operation, we biased the SNSPD at 35 μA and the nTron at 95 μA. Expected operation was ensured by measuring: photon sensitivity for the SNSPD and amplifier when biased separately; critical current suppression in the nTron channel

when the SNSPD was overbiased (creating a hotspot in the gate); count rate from both outputs when biased together; count rate vs. I^{bias}; and count rate from the SNSPD vs I_{SNSPD}. The results of these measurements allowed us to conclude that (1) the nTron amplifier, at a bias of 95 µA, was not photosensitive; (2) there was a 1:1 correspondence in counts between the two outputs (one amplifier pulse per SNSPD pulse); (3) no counts were generated in the amplifier when only the SNSPD was biased, and vice-versa.

5.5.6 Power dissipation and clock rate

In addition to jitter characterization, to assess the utility of the nTron in future applications, we discuss here its potential clock rate limitations. The maximum clock rate of an nTron is determined by both the superconducting and thermal properties of its constituent materials. Although we presently have no direct measurement of the maximum operating speed of an nTron circuit, their thermal and electrical properties are expected to be identical to SNSPDs, whose reset times are well understood [90] [51]. In SNSPDs, the limiting timescale for reset is either the inductive electrical time constant or the thermal recovery time from the normal to superconducting state, whichever is longer. After the thin film returns to the superconducting state, high-energy phonons must escape into the substrate for the device to return to its initial non-resistive state. This geometry-independent recovery period has been measured to be below 100 ps [92] [93], suggesting an maximum clock rate on the order of 1 GHz for thin-film NbN.

In many cases, switching power dissipation is a factor in determining applicability of a new electronic device. To estimate the optimal power usage per switching event in the non-latching (pulsed) regime, we used conservative values for the nTron device inductance (∼1 nH) and the channel bias current (∼100 µA). These estimates yield a minimum switching-energy of $E \approx LI^2 = 1 \times 10^{-17}$ J/bit for our initial devices, within two orders of magnitude of current SFQ technologies [94]. These speed and power estimates may be improved upon by using different materials or geometries or by scaling to smaller dimensions, which may be desirable in digital applications. Even

for applications in high-performance computing, where Josephson junction electronics may be preferable, the nTron can provide ancillary utility in the form of interfaces with sensors and high-impedance loads such as readouts and data-storage address lines.

5.6 High-T_c YBCO nTrons

In a collaboration with Riccardo Arpaia and Floriana Lombardi of Chalmers University, we were able to test an nTron fabricated from the high-temperature superconductor $YBa_2Cu_3O_7$ (YBCO). YBCO is an exotic cuprate compound which has a T_c of 90 K, well above the boiling point of liquid nitrogen. The Chalmers group had a well-developed thin-film YBCO patterning process, and so by sending them the geometry of the nTron, they were able to recreate the geometry in YBCO, just as we had done with NbN. An image of a chip they fabricated, which was 50 nm of YBCO capped with 50 nm of gold, is shown in Fig. 5-10.

5.6.1 Cryostat experimental setup

Testing the YBCO nTron required some experimental alterations from the NbN measurement setup. YBCO does not tolerate moisture well and thus cannot be cooled down except under vacuum, for fear of degrading the material with condensation. Instead of dunking the sample directly in liquid helium, we built a custom PCB sample mount for the sample. We were able to aluminum wirebonds to connect to the YBCO device because the YBCO was capped in gold – with bare YBCO, it likely would have been difficult to make a solid connection, as YBCO is ceramic-like in most of its physical properties and thus a bond is not easily formed by the wirebonder's ultrasonic bonding process.

The PCB we built with the mounted chip is shown in Fig. 5-11. For each nTron bonded, there was a direct input to the gate, as well as a four-point connection setup which measured the voltage across the channel (two points on the drain terminal, two on the source terminal) and passed that voltage to a SRS560 low-noise voltage

preamplifier. The reason the voltage preamplifier was necessary in this setup and not in the NbN setup was because of the thick gold capping layer on the YBCO. This layer reduced the normal state resistivity of the nTron channel to less than 1 Ω, making it difficult to distinguish the superconducting state from the normal state without amplification.

5.6.2 YBCO nTron results

After cooling down the device to 4 K under vacuum in the cryostat, we measured the IV curve of the nTron channel. The result of the IV curve for zero gate bias is shown in Fig. 5-12. The nTron channel, which was 400 nm wide, had a critical current of 6.1 mA and was non-hysteretic due to the large conductance of the capping gold.

We then measured the IV curve as a function of gate bias, which is shown in Fig. 5-13. These measurements showed that for every 200 µA of gate current added, the IV curve was shifted by exactly 200 µA. This result indicates that there was no hotspot-effect action being produced at the nTron choke. The channel critical current varies linearly with the gate input, even when the gate choke is biased above its critical current. In normal nTron operation, the change of the choke from superconducting normal should trigger a flood of quasiparticles into the channel, suppressing the superconductivity and shifting the IV curve significantly more than the 1:1 ratio seen in Fig. 5-13. The most likely reason for the lack of the hotspot effect is that the gold provides an excellent thermal and quasiparticle shunt, carrying away hot electrons before they are able to deposit energy on the superconducting channel. The next step for testing the nTron in high-temperature superconducting materials will be to use YBCO devices that are not capped in gold.

5.7 Conclusion

The central result of this section was the design, characterization, and implementation of the nTron, a superconducting three-terminal electrothermal device that does not rely on Josephson junctions. The nTron was used to demonstrate digital operations,

as well as pulse amplification with picosecond timing resolution. The nTron has immediate application to the readout of superconducting sensors such as those used in quantum computing (e.g. flux qubit readout, transmission line multiplexing), communications (e.g. single-photon detectors, driving optical modulators), and astronomy (e.g. as an alternative amplifier to SQUIDs for reading out large detector arrays). Its operating characteristics are also complementary to Josephson-junction-based technologies, and integration could enable those technologies to perform otherwise-difficult tasks such as memory line-driving and fanout in exascale computing. Additionally, the ease of fabrication, transistor-like logic-gate design, and extensibility to other materials mean that small-scale superconducting circuits are now accessible with minimal fabrication investment and straightforward circuit designs.

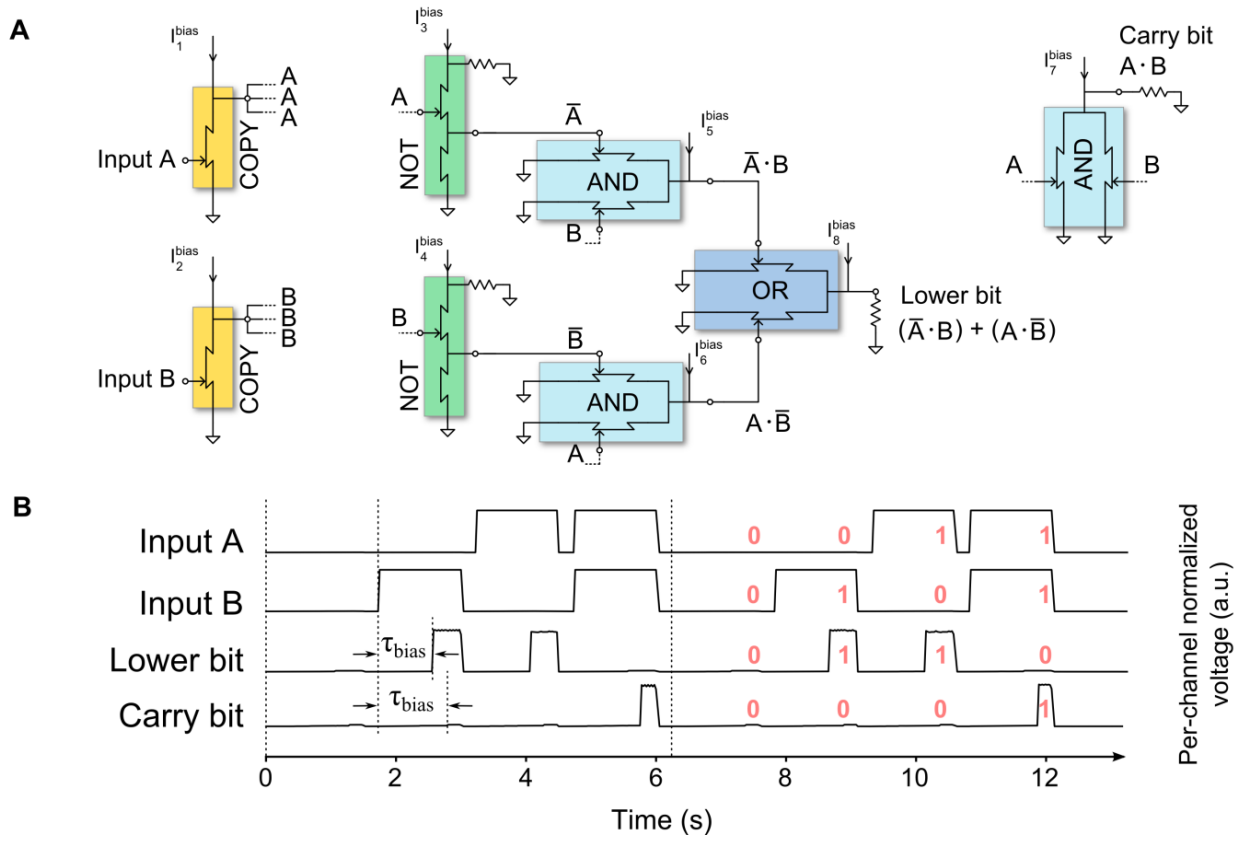

Figure 5-5: Experimental demonstration of an nTron half-adder. (A) Half-adder circuit schematic constructed from logical gates. Single inputs were provided into the initial (yellow) COPY gates, which acted as buffers for the signals Input A and Input B, each with a fanout of three. Connections to ground and between gates were made with low resistance, non-superconducting links. (B) Per-channel output for the half-adder for computation of 0+0, 0+1, 1+0, and 1+1, repeated twice. HIGH (1) and LOW (0) current values were input to Input A and Input B, and after a bias electronics delay τ_{bias}, the lower bit and carry (upper) bit outputs represented the resulting sum of the inputs. The red text overlay of ones and zeros corresponds to HIGH and LOW values.

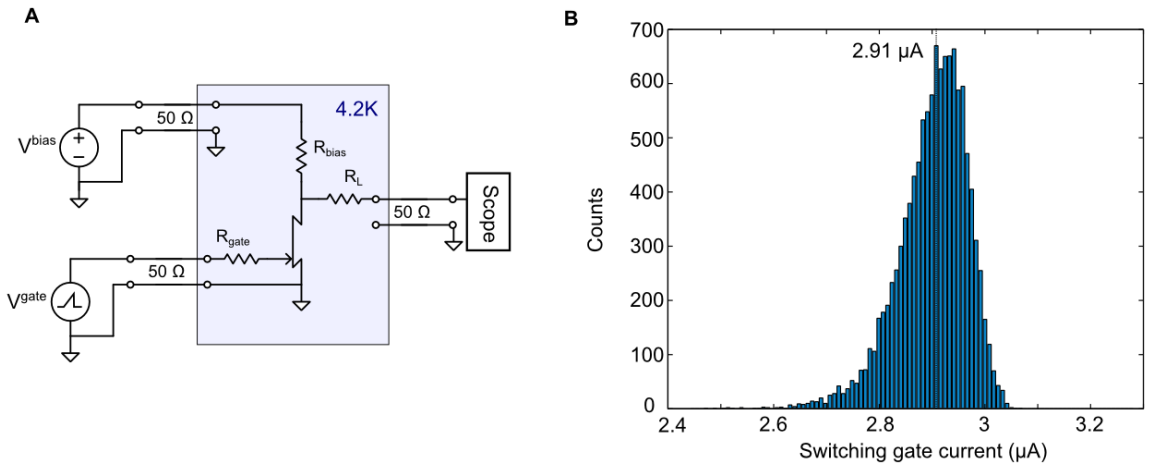

Figure 5-6: The current comparator experiment used to test the input sensitivity of the nTron. (A) Circuit diagram for the nTron current comparator. The channel was biased at a fixed value, and the gate was ramped until output appeared at the scope. (B) Histogram of I^{gate} values for the gate current at which the comparator switched and produced an output voltage at the scope.

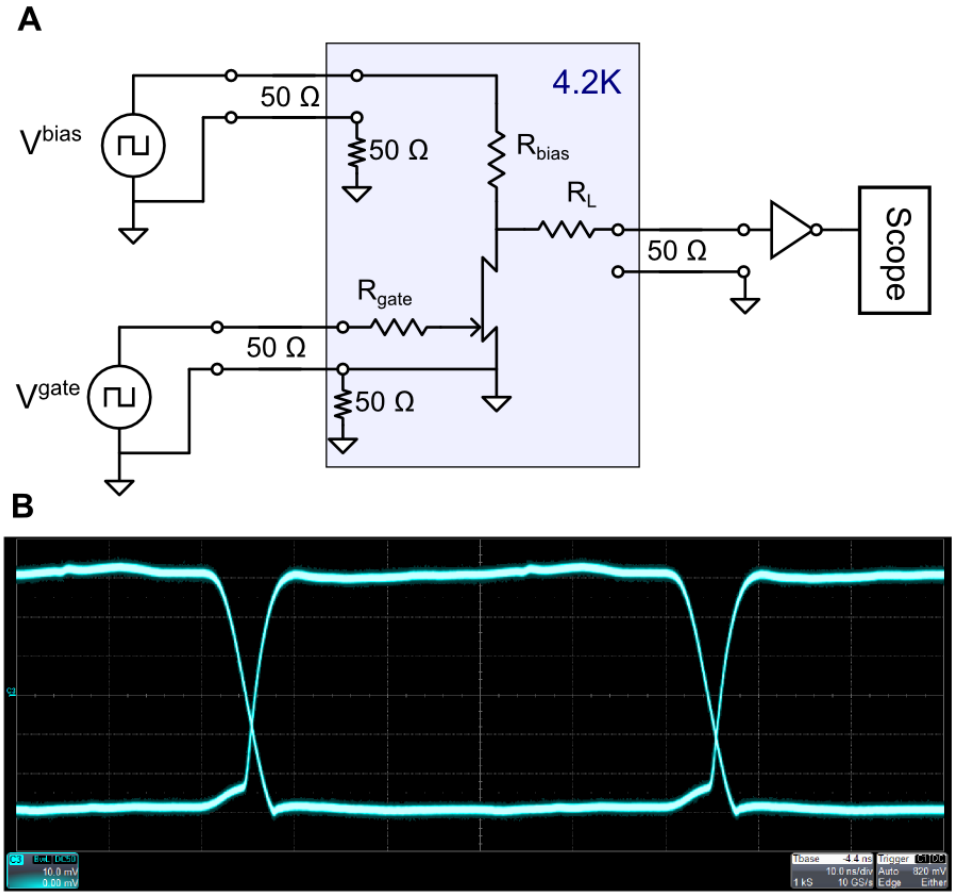

Figure 5-7: Circuit schematic for 10 MHz eye diagram experiment. (A) Circuit diagram for the nTron 10 MHz eye-diagram experiment. The area in blue represents the portion of on the sample holder and submerged in liquid helium at 4.2 K. Placing the resistors close to the device allowed us to convert the incoming voltage square waves to a low-amplitude current square waves. The resistors R_L, R_{bias}, and R_{gate} were 1.46 kΩ, 20.8 kΩ, and 42.0 kΩ, respectively (as measured at 4.2 K). (B) 10 MHz modified eye diagram output taken directly from oscilloscope

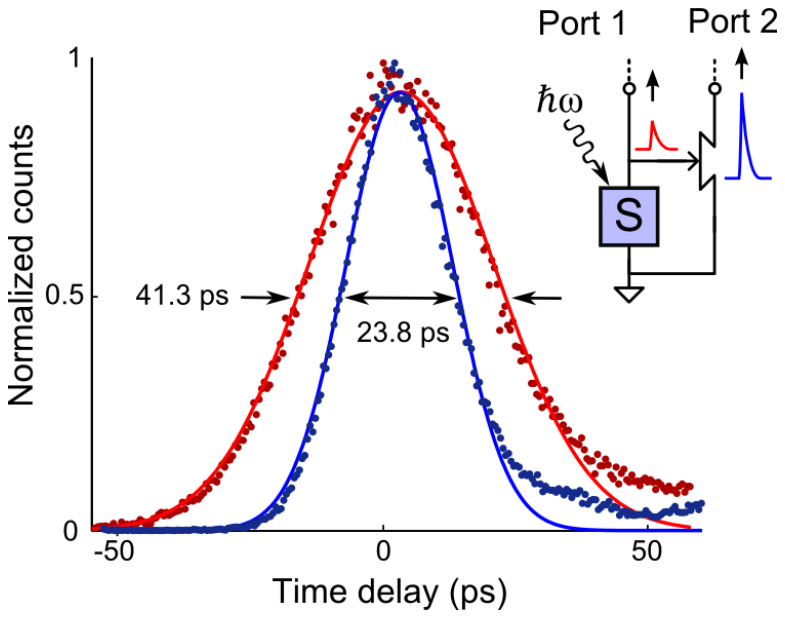

Figure 5-8: Jitter measurements for an nTron integrated as an amplifier for a superconducting nanowire single-photon detector (SNSPD) pulses. Detection of laser photons from a sub-ps laser by the detector (inset, purple 'S' box) generated an electrical pulse on Port 1 (inset, red) and also triggered a concurrent, amplified pulse from the nTron on Port 2 (inset, blue). Plotted is a histogram of the relative delay between the laser sync edge and the resulting electrical pulse edges of the unamplified SNSPD (red dots) and nTron-amplified output (blue dots). Gaussian fits to each data set are shown as solid lines. The reduced jitter in the amplified signal is due to increased signal amplitude. (upper right) Device schematic of the integrated SNSPD-nTron pulse amplifier.

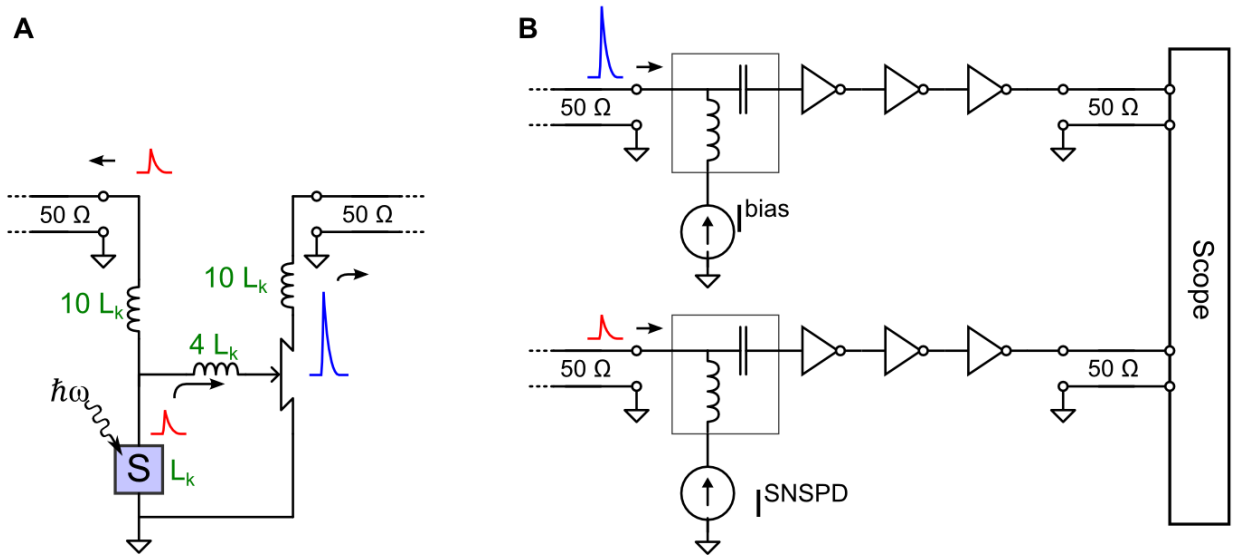

Figure 5-9: Circuit schematic for the SNSPD and nTron pulse amplifier experiment. (A), Device circuit schematic. The inductors were made by patterning long nanowires, which intrinsically produce kinetic inductance. The length of the inductor nanowires (and thus their total inductance) were scaled against the SNSPD, which had an approximate kinetic inductance of $L_k \approx 25\,\mathrm{nH}$. (B) Room-temperature readout and bias electronics. Pulses generated from the device and output to the coax in (a) arrived at the other end of the coax, shown in (b), where they were amplified with three 20-3000 MHz amplifiers in series before being input to the scope.

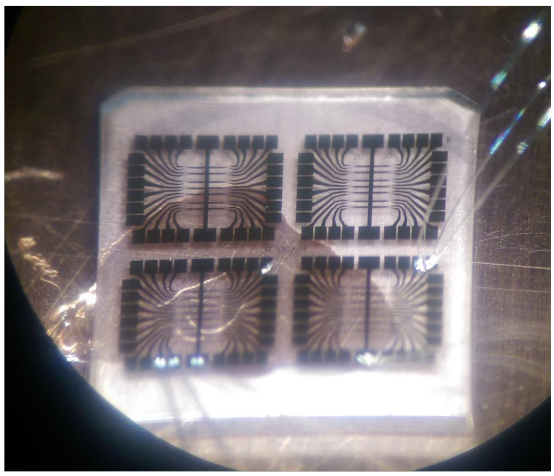

Figure 5-10: Microscope image of the YBCO chip created for us by Lombardi group at Chalmers University. The material is 50 nm of YBCO capped with 50 nm of gold on an MgO substrate.

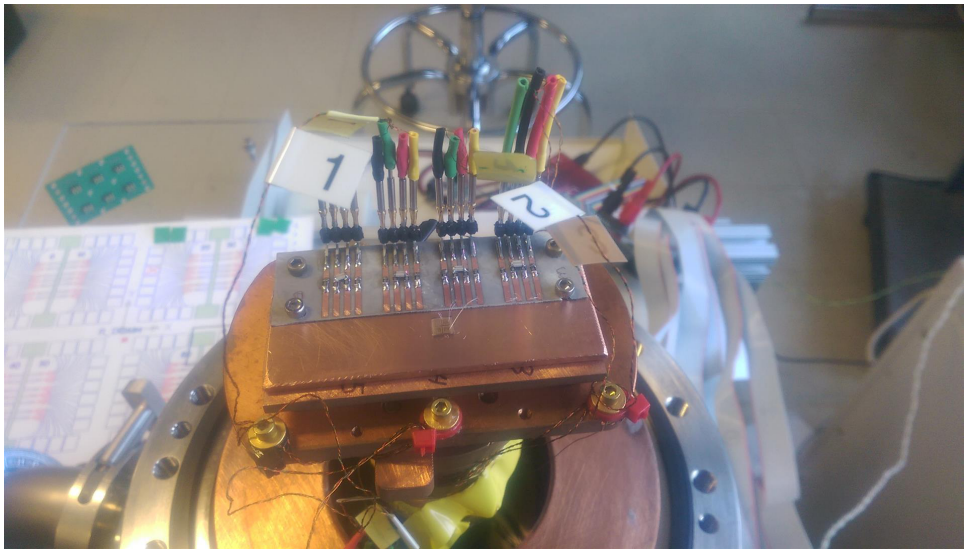

Figure 5-11: YBCO sample wirebonded to the custom PCB and mounted in the vacuum cryostat.

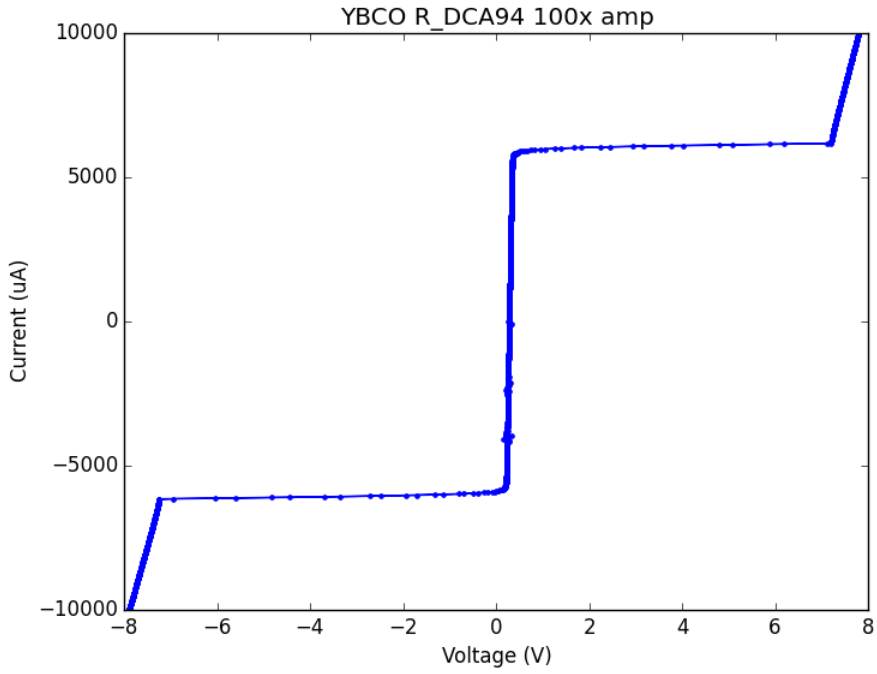

Figure 5-12: I-V curve shown for the YBCO nTron, with $I^{\text{gate}} = 0$.

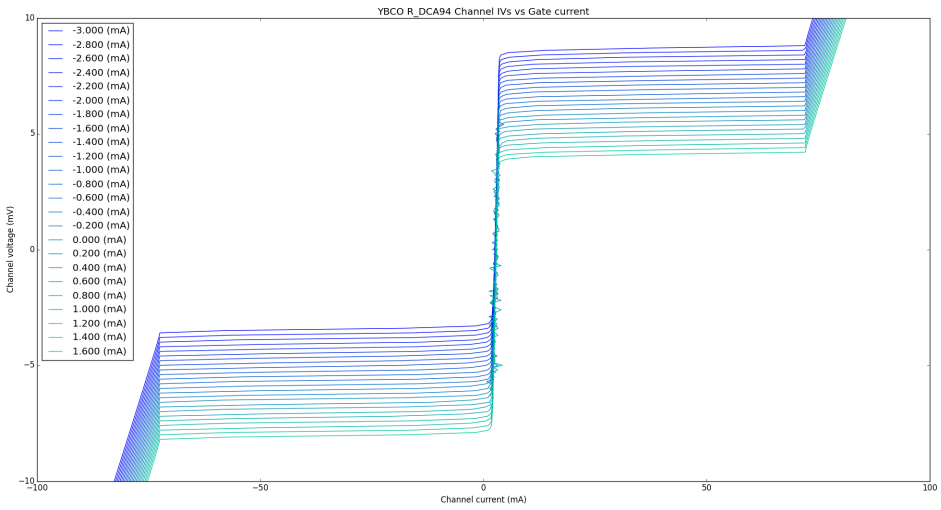

Figure 5-13: I-V curves of the YBCO nTron versus as a function of varying I^{gate}. Shown are values of I^{gate} in increments of 200 µA.

Chapter 6

The current-crowding cryotron (yTron)

The yTron is a three-terminal device which is capable of sensing superconducting loop currents inline without perturbing the superconducting state. This functionality is unique to the yTron, because typically this type of measurement must be done either by magnetically coupling to an external loop or by perturbing the superconducting state in enough to allow flux to pass out of the loop. In this chapter I describe the basic description, characterization, and application of this device. Like the nanoSQUID chapter, the text that follows constitutes a preliminary writeup of work which will be submitted to a journal for publication.

6.1 Device description

The yTron is made from a single layer of superconducting niobium nitride (NbN) thin film which has been patterned into a "Y" shape. As shown in Fig. 6-1, the drain and the gate terminals form the upper arms of the Y, joining together at a sharp intersection where they connect to form the source terminal. The width of the source terminal is equal to the summed widths of the drain and the gate terminals.

The material used to make the device shown in Fig. 6-1 was thin-film NbN which was deposited on SiO_2 in a DC magnetron sputtering system at 800 °C. This NbN

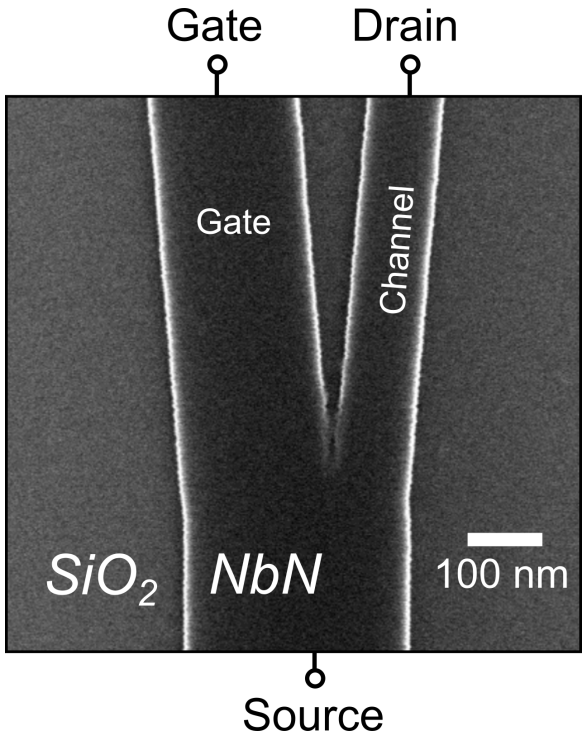

Figure 6-1: Scanning electron micrograph of a yTron with a 200 nm gate and 100 nm channel. The low contrast of the edges that form the intersection are due to the tapering of the e-beam resist in that region.

film was measured to have a sheet resistivity of 437 Ω/□, and a T_c of 10.65 K. After deposition, contact pads shapes were patterned onto the film via photolithography. After patterning, 10 nm Ti and 50 nm Au were deposited to form the contact pads. After performing liftoff to remove the excess Ti and Au, the sample was cleaned by sonicating it in acetone for 5 min. Once cleaned, 4% HSQ was spun onto the sample at 3 krpm for 60 s, creating an HSQ film approximately 50 nm thick. The yTron patterns were then exposed into the HSQ resist by electron-beam lithography on an Elionix 125 kV tool which had a beam current of 1 nA with an areal dose of 3840 μC/cm^2. The patterns were developed by developing the sample in 25% TMAH for 2 min and then rinsing with deionized water for 30 sec. Lastly, the sample was etched in 1.33 Pa (10 mTorr) CF_4 in a PlasmaTherm RIE at 50 W of RF power for 3 min. The 50 W of RF power was spread over 100 cm wafer in the etcher, giving a an areal etching power of 6.4 mW/cm^2.

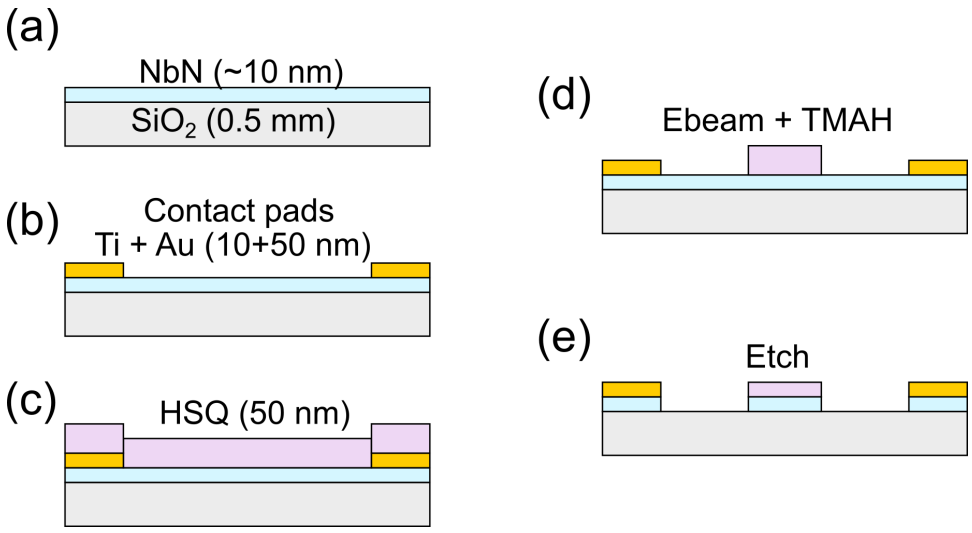

Figure 6-2: Fabrication steps for patterning the yTron out of a thin NbN film. (a) NbN is deposited on an SiO_2 substrate. (b) Titanium-gold contact pads are added by a photolithographic liftoff process. (c) The e-beam resist HSQ is spun on the sample. (d) The HSQ is patterned by an e-beam tool and developed. (e) The sample is etched, leaving NbN only in the areas protected by the HSQ and contact pads.

6.2 Device operation

The functionality of the yTron as an inline current sensor comes from the dependence of the channel switching current on the amount of current flowing into the gate. Although counter-intuitive, adding current to the gate actually increases the switching current of the channel. This increase is the result of to current crowding [57] [95] due to current density mismatches at the intersection of the two upper arms. Current crowding describes the increase in current density that takes place for currents that are bent around sharp features, as shown in Fig. 6-3. The yTron uses this phenomenon as a means controllably break down superconductivity at the intersection between the gate and the channel nanowires.

6.2.1 Current crowding and the channel critical current

We can explain the impact of current crowding using the three examples shown in Fig. 6-4. In Fig. 6-4(a), the yTron is biased such that the current densities through the gate and the channel are equal. As a result, the current densities on either side of

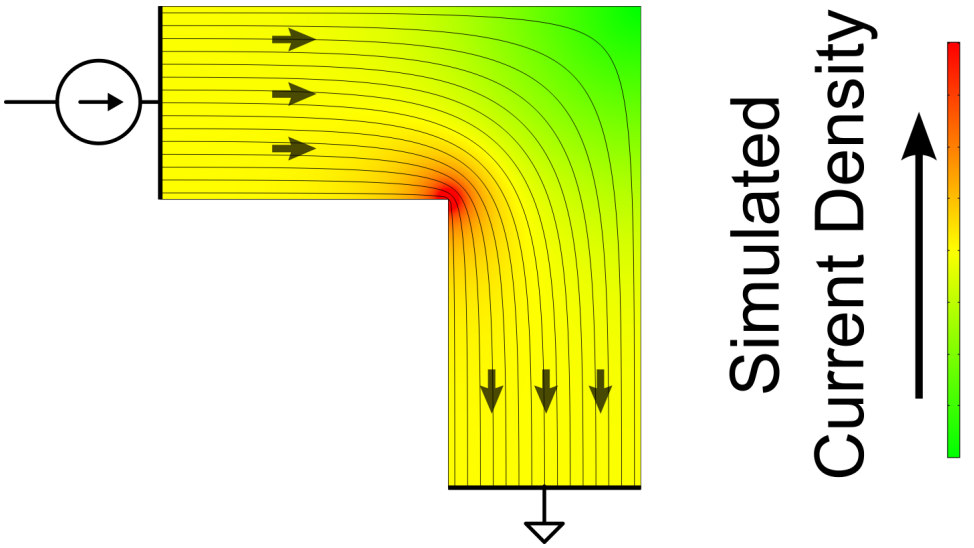

Figure 6-3: Simulation of current flowing around a sharp corner. Current-streamlines are shown, and the coloration indicates the current density, which is at a maximum around sharp corner feature.

intersection are equal and the current streamlines join together smoothly as they flow to the source. In Fig. 6-4(b), the current flowing into the gate has been reduced, and as a result the current streamlines from the channel bend slightly around intersection point so that they can redistribute evenly by the time they arrive at the source. In Fig. 6-4(c), the gate current has been shut off, and the current streamlines from the channel bend sharply around the intersection point as they redistribute. The current flowing through the channel is subject to a large amount of current crowding as it bends around the intersection corner. In other words, the channel current density–which is uniform at the channel terminal entrance–increases in magnitude near the intersection. The increased current density acts as a weak point for the breakdown of superconductivity, either through the entry of vortices [63] or the formation of a hotspot [60]. As a result of this process, reducing the gate current decreases $I_{\mathrm{sw}}^{\mathrm{ch}}$, the switching current of the channel.

Modulation of the yTron channel switching current can be best explained by examining the horizontal current components near the intersection point as shown in Fig. 6-5. Components of the gate current which are tangential to the intersection boundary (and thus produce current crowding) can oppose and cancel out the hor-

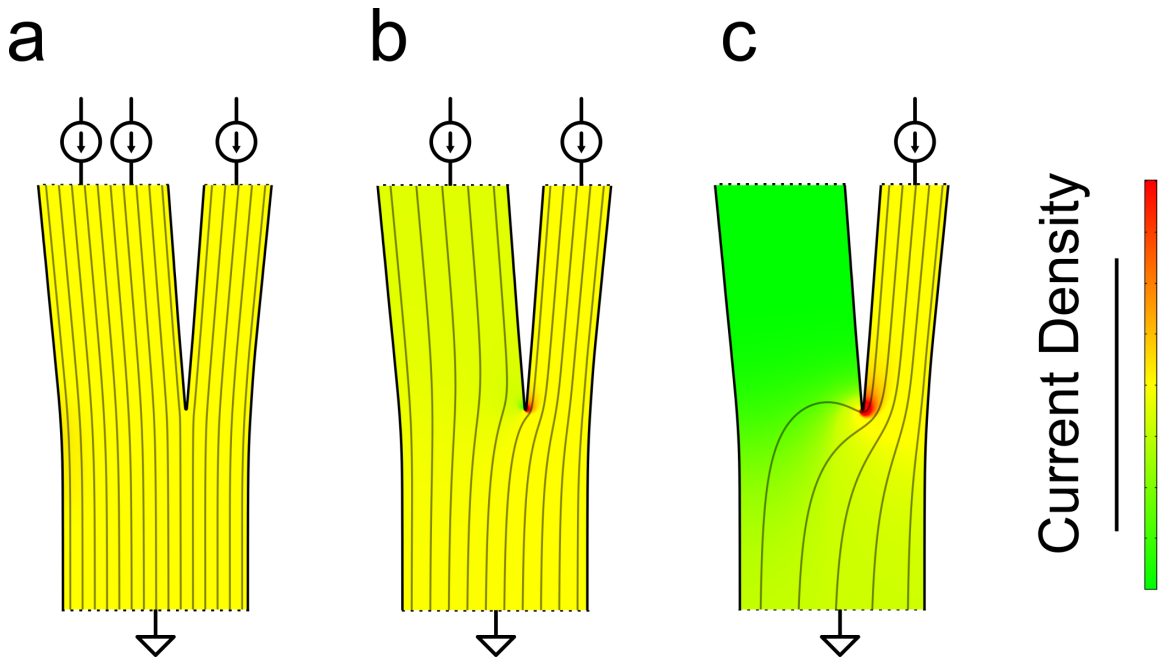

Figure 6-4: Current flow streamlines in the current-crowding cryotron for various gate biases. (a) The gate is biased at the same current density as the channel, and there is minimal current crowding at the intersection. (b) The gate is at half the channel current density. (c) The gate carries no current, and as a result the streamlines from the channel curve sharply around the intersection, causing significant current crowding.

izontal components from the channel. This cancellation results in a total reduction of the current crowding at the intersection. In this way, current added to the gate diminishes current crowding in the channel, and as a result increases the channel switching current.

6.2.2 Output characterization

Fig. 6-6 shows the characterization of a device with the same dimensions as the yTron shown in Fig. 6-1. The dependence of the channel switching current $I_{\mathrm{sw}}^{\mathrm{ch}}$ on the gate current input I^{gate} is approximately linear over a large range of I^{gate} values. This linearity occurs because the magnitude of the current crowding is dependent on the horizontal components of the current density, with respect to the intersection edge. Equal current densities on either side of the intersection produce a minimum in the current crowding, because the horizontal components at the intersection point are

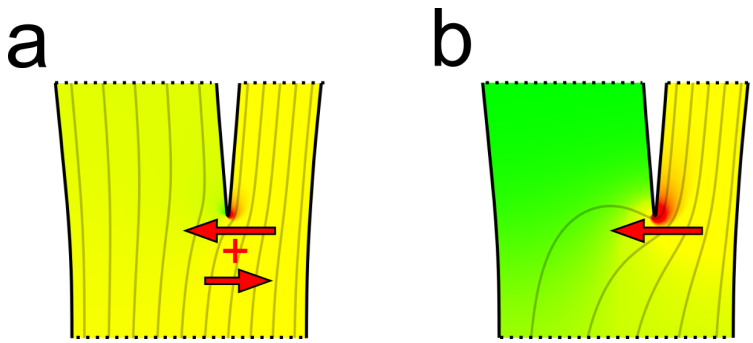

Figure 6-5: Simulation of two yTron bias points showing the summation of horizontal currents. (a) Current flowing in from the upper left arm and current flowing from the upper right arm produce horizontal current components which mostly cancel each other out, reducing current crowding at the intersection point. (b) Current only flowing in from the upper right arm. In this scenario there is no cancellation of horizontal current components, and so there is a large amount of current crowding at the intersection point.

equal and opposite, and thus cancel each other out. This cancellation is conceptually similar to a Wheatstone bridge, where current flow across the midsection of the bridge is minimized when the contributing currents from either side are equal and opposite.

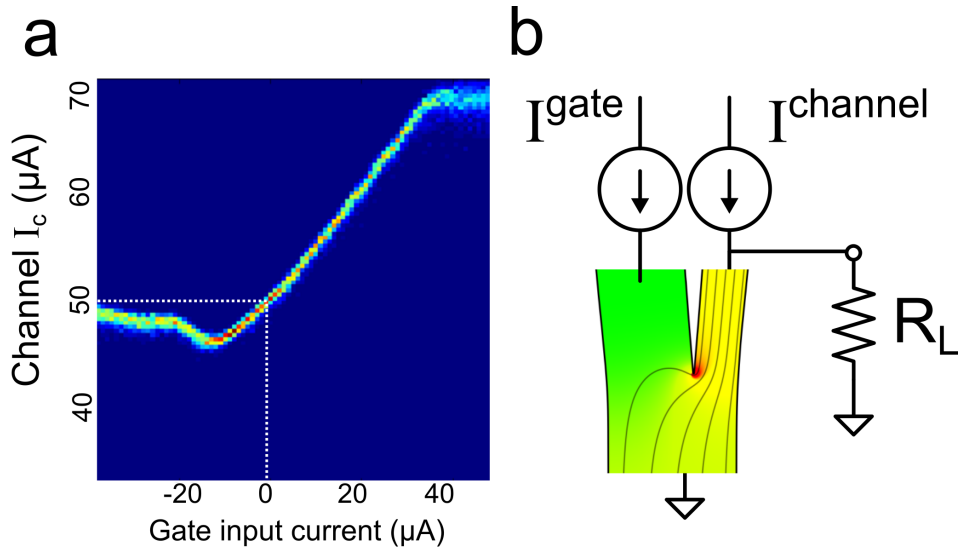

Figure 6-6: Channel switching current modulation versus gate current.

In developing the yTron, we tested several devices with varying widths of the channel and gate nanowires, and found that the ratio of the widths of the channel and gate determines the dependence of I_{sw}^{ch} on the gate current. Specifically, this

ratio determines the slope of the linear regime of $I_{\mathrm{sw}}^{\mathrm{ch}}(I^{\mathrm{gate}})$ in Fig. 6-6. For example, the device pictured in Fig. 6-1 has a channel width of 200 nm and a gate width of 100 nm, giving a channel-to-gate width ratio of 0.5. This 0.5 ratio corresponds approximately to the slope of the linear portion of Fig. 6-6, which is 0.61. We tested a variety of devices with gates and channels ranging from 100-800 nm, and which had channel-to-gate width ratios between 1:8 and 8:1. We found that the slopes of their $I_{\mathrm{sw}}^{\mathrm{ch}}(I^{\mathrm{gate}})$ graphs ranged from 0.33 to 2.93, and although there was quite a bit of scatter with respect to the absolute slope values (even between nominally-identical devices) generally the smaller the channel-to-gate ratio, the lower the slope value.

Looking closely at Fig. 6-6, we observed that the dependence of $I_{\mathrm{sw}}^{\mathrm{ch}}$ on I^{gate} had well-segmented regions of behavior. Around $I^{\mathrm{gate}} = 0$ there was a linear region of $I_{\mathrm{sw}}^{\mathrm{ch}}(I^{\mathrm{gate}})$, where the current densities on either side of the intersection summed linearly to produce current crowding as described earlier. This region was where yTron would be most useful as a current sensor, as the straightforward linear dependence can be used to infer I^{gate} from $I_{\mathrm{sw}}^{\mathrm{ch}}$ measurements. However, as shown in Fig. 6-6 there are two additional regions on either side of that range. For the device measured in Fig. 6-6, these regions corresponded to when I^{gate} was above 38 µA or below -14 µA. We believe the change of $I_{\mathrm{sw}}^{\mathrm{ch}}(I^{\mathrm{gate}})$ away from a simple linear slope occurs when design or fabrication imperfections around the intersection begin to cause more current crowding than the intersection point itself. When we tested device on the same chip with different dimensions, the size of this linear region was variable – in one case, it ranged from -5 µA to 20 µA, and in another cases it ranged from -25 µA to 50 µA. It will not be possible to rule out other causes without further characterization, but if small defects existed a few tens of nanometers away from the intersection point, they could act as focal points for current crowding which only exceeded the intersection current crowding once the gate current became high or low enough.

6.3 Device design considerations

6.3.1 Material considerations

There are several aspects of the yTron design which impact its operation. The first characteristics which must be considered are those of the superconducting material from which the device is fabricated. The superconducting film thickness must be less than the material's penetration depth λ in order for the current crowding to work as described. In a thicker superconductor with a non-uniform kinetic inductance, current will not be distributed evenly across the cross-section of each arm of the yTron, altering the effect of current crowding. By making the device from a film thinner than λ, the device has an (approximately) uniform sheet kinetic inductance that enforces the current redistribution shown in Fig. 6-4.

The other material parameter which must be considered when designing a yTron is the superconducting coherence length. To minimize tunneling effects, arms of the yTron should be wider than the coherence length (in thin-film NbN $\xi \approx 4\,\text{nm}$ [96]). This minimum width is necessary because the yTron relies on an non-uniform current distribution across the width of the wire to produce current crowding. This distribution would not be possible if, for example, all dimensions of the yTron channel were narrower than the coherence length and thus the channel was effectively one dimensional.

6.3.2 Geometric considerations

The geometry of the yTron determines its operation. The dependence of the channel switching current $I_{\text{sw}}^{\text{ch}}$ on the gate current I^{gate} is based on three factors: (1) the sharpness of the intersection point, (2) the widths of the channel and gate nanowires, and (3) the angle at which the gate and channel intersect. In testing various geometries, we did not vary the third factor, and so will not detail its impact here. Nominally, an infinitely sharp point at the intersection tip would result in an infinite amount of current crowding for any streamline bending around the intersection. As a result,

the current density at the corner should diverge is cases like Fig. 6-4b and Fig. 6-4c. However, the sharpness of the intersection point will always be ameliorated by two factors: rounding caused by the practical fabrication limits of e-beam lithography ($\sim$15 nm for the device in Fig. 6-1), and a radius-of-curvature effect (as described in Ref. [57]) in the superconductor produces a rounding of the intersection point on the order of the material superconducting coherence length, even for a perfectly sharp intersection.

In the scenario where the lithographic rounding is significantly smaller than ξ, we can bound the effects of current crowding by approximating the yTron intersection as a 180° hairpin turn. With this approximation, the channel switching current can be reduced by at most a factor of $R = \sqrt{\pi\xi/w}$, where w is the width of the nanowire. For the device described here, $\xi = 10\,\text{nm}$ and $w = 200\,\text{nm}$, and so the range of values $I_{\text{sw}}^{\text{ch}}$ can take will be between 39.6 % and 100 % of the switching current of a 200-nm-wide wire. This value sets a limit to the dynamic range of the yTron.

6.4 Operating modes of the yTron

The yTron can either be used as a latching digital discriminator, or a three-terminal controllable weak link. These two modes are schematically drawn in Fig. 6-7. The mode in which the device operates depends on whether the channel IV curve is hysteretic, which in turn depends on the shunt resistance in parallel with the channel nanowire [1] [82] [81]. If the channel IV curve is hysteretic (large shunt resistance), the device operates as a latching digital discriminator: when the current in the channel exceeds $I_{\text{sw}}^{\text{ch}}(I^{\text{gate}})$, a hotspot will form and stabilize, producing a DC output voltage between the drain and source terminals. Conversely, if a low enough shunt resistance is present across the channel and it becomes non-hysteretic, the channel cannot support a stable hotspot. Instead, the channel will behave like a Dayem-bridge-type weak link, and when biased above $I_{\text{sw}}^{\text{ch}}(I^{\text{gate}})$ flux will be allowed to pass across the channel by way of vortex crossings. Fig. 6-8 shows IV curves of the yTron described here for various values of I^{gate}. Each curve looks approximately like a standard IV

curve for a superconducting NbN nanowire, with a switching current that depends on I^{gate}. Since the material used was thin-film NbN, the curves are highly hysteretic as expected.

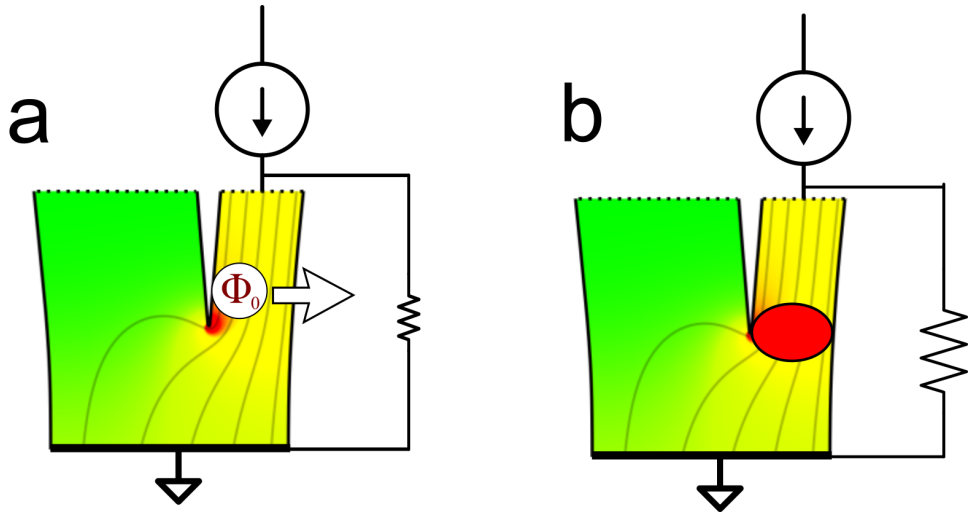

Figure 6-7: The two operating modes of the yTron, which match the operating modes of a typical nanowire [1] based on whether or not the nanowire is hysteretic. (a) The channel is shunted by a small resistance in parallel. Flux flows across the channel, but the small resistance shunts the bias current and prevents a stable Joule-heated hotspot from forming. (b) The channel has a large shunt resistance. Significantly more power is dissipated in the channel, allowing a self-sustaining Joule-heated hotspot (normal region) to form.

Effectively, the yTron acts as a three-terminal controllable weak-link: the amount of current flowing into the gate terminal controls the passage of flux across the channel terminal. At no point during this process is the current in the gate modified; the vortex flow (or hotspot) is isolated in the channel nanowire, leaving the current flowing through the gate undisturbed. This allows nondestructive readout of superconducting loop currents, which previously was only possible through magnetic coupling.

6.4.1 Isolation of the gate from the channel

Isolation between the gate and channel is a key feature of the yTron. Since the yTron is fabricated from a continuous superconducting film, "isolation" in this context does not mean electrically disconnected like the gate of a MOSFET, but instead the isolation of the gate from changes in the channel. The key feature of the yTron is that even

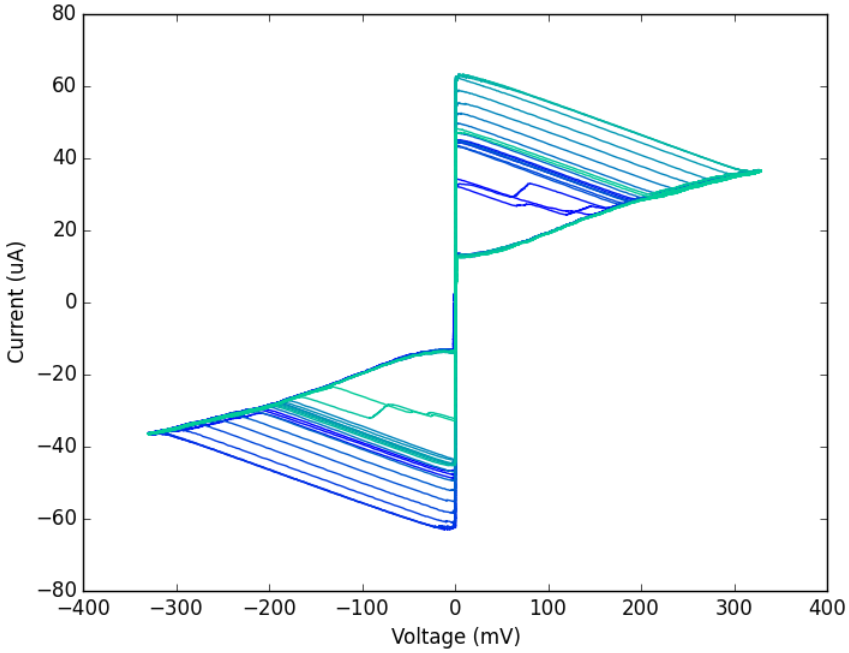

Figure 6-8: IV curves of the yTron channel for different values of I^{gate}. Each IV curve looks approximately like a nanowire with a different I_{c} value.

when the state the channel changes–e.g. between the superconducting state, vortex flow state, or hotspot state–the superconducting state of the gate nanowire is not perturbed. Due to the indirect nature of the current-crowding-based modulation of $I_{\text{sw}}^{\text{ch}}$, a voltage state in the channel (source to drain) does not produce any voltage on the gate (gate to drain). As an example, let us assume we have a non-hysteretic yTron whose channel is biased at I^{ch}, just below $I_{\text{sw}}^{\text{ch}}$. When I^{gate} is reduced, $I^{\text{ch}} > I_{\text{sw}}^{\text{ch}}$, and vortices will begin to flow across the channel, producing a voltage between the source and drain terminals. Despite the fact that flux is passing across the channel nanowire, the gate nanowire is still entirely superconducting and no flux is able to cross. One concern we had when testing the yTron was that excited quasiparticles generated by the hotspot or vortex crossings could diffuse into the gate and perturb the current flowing there. In thin-film NbN, this diffusion length is ∼100 nm [84], on a similar scale to the nanowire widths. However, we found that as long as the total power dissipation in the channel was below 350 nW, it did not impact the switching current of the gate.

6.5 Measurement details

The results of Fig. 6-6 were measured using a current-sweeping setup. Each vertical slice of the graph corresponds to a set of 100 measurements of $I_{\rm sw}^{\rm ch}$ for a given value of $I^{\rm gate}$. Measurement of each distribution began by setting the $I^{\rm gate}$ input, using an SRS variable battery source with a 10 kΩ series resistor in front of the positive terminal. A current ramp was then applied to the channel using an arbitrary waveform generator in series with a 10 kΩ resistor. $I_{\rm sw}^{\rm ch}$ was then recorded as the value of the current ramp when a voltage appeared at the channel input (triggered at 1 mV), indicating the switching of the channel from the superconducting to normal state. This measurement was then repeated an additional 100 times to yield the distribution for $I_{\rm sw}^{\rm ch}(I^{\rm gate})$. Extended details about measuring the critical current distribution can be found in Section 7.1.1. All measurements were made at 4.2 K by submerging the sample directly into liquid helium. The sample was shielded from spurious RF radiation by a thin copper box, but no magnetic shielding was used.

6.6 Inline, nondestructive measurements of a quantized superconducting loop current

Due to its ability to read inline currents, a natural application for the yTron is the readout of quantized currents in a superconducting loop. By placing the gate of the yTron inline with a superconducting loop, we were able to use the yTron to nondestructively read out the number of discrete fluxons (n) trapped in a the loop. We successfully resolved the adjacent fluxon states (n, $n+1$, etc) of the loop, and were able to read out those states several thousand times consecutively without changing the value of n. This application was possible because the gate (loop) current can be inferred from $I_{\rm sw}^{\rm ch}$, which can be measured without allowing flux into or out of the loop. Each trial of the experiment consisted of two alternating steps: First we measured $I_{\rm sw}^{\rm ch}$ several thousand times consecutively (Fig. 6-9). We then heated part of the gate-source loop above $T_{\rm c}$ to break the superconducting loop temporarily and

allow the number of stored fluxons n to change randomly (Fig. 6-10).

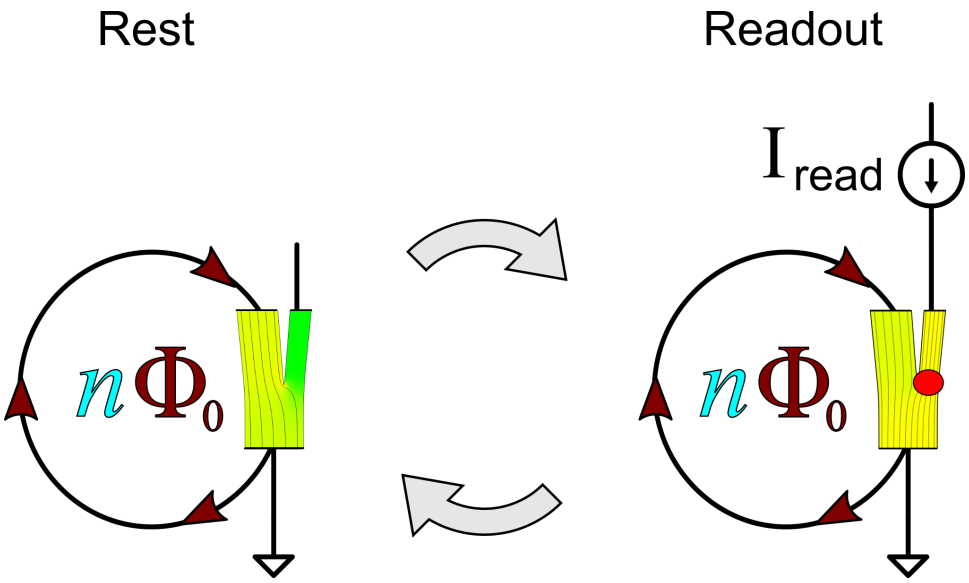

Figure 6-9: Readout procedure for the inline nondestructive measurement of the superconducting loop. The gate-source loop started out at rest (left), and then the I_c of the channel was measured by ramping I_{read} until a hotspot formed in the channel (right). I_{read} was then turned off and the system returned to rest (left). This process was able to be repeated several thousand times without changing n, the number of fluxons trapped in the gate-source loop.

By measuring the channel current after heating it repeatedly, we observed step-like behavior in $I_{\mathrm{sw}}^{\mathrm{ch}}$, which is shown in Fig. 6-11 which indicates the nondestructive readout of quantized loop currents. During each trial, the distribution of $I_{\mathrm{sw}}^{\mathrm{ch}}$ was fixed. Only when the loop was heated and re-cooled did the distribution of $I_{\mathrm{sw}}^{\mathrm{ch}}$ change. Moreover, when the loop was heated and re-cooled, the distribution of $I_{\mathrm{sw}}^{\mathrm{ch}}$ shifted by integer multiples of 2.48 µA, corresponding to the addition or removal of quantized currents in the gate-source loop. The fixed distribution of $I_{\mathrm{sw}}^{\mathrm{ch}}$ during the first step indicates that the readout process $I_{\mathrm{sw}}^{\mathrm{ch}}$ did not alter n. Correspondingly, the evenly-spaced and non-overlapping $I_{\mathrm{sw}}^{\mathrm{ch}}$ measurements between trials indicate we were able to read out individual, adjacent fluxon states (e.g. n, $n+1$, $n+2$). Since the film had an inductance of ∼10 pH/□, we calculated that our loop had an inductance of approximately 200 pH/□, meaning each fluxon contributed 10 µA. This fluxon current value corroborates well with our measurements of other standalone yTrons of similar dimensions, which have shown that for every 2-3 µA of gate current added,

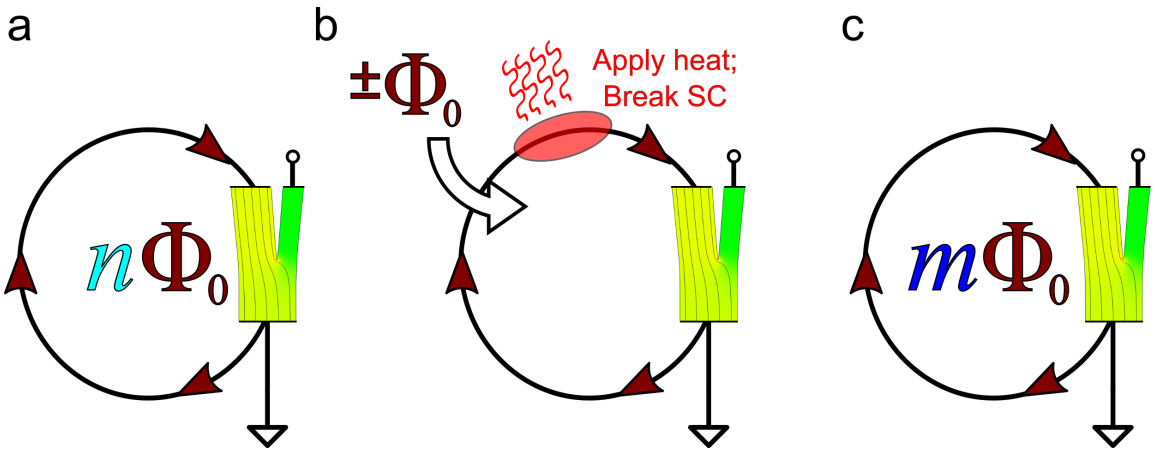

Figure 6-10: Procedure to change the number of fluxons n in the superconducting gate-source loop. (a) The entire device starts out unbiased, completely superconducting. n fluxons are stored in the gate-source loop. (b) An applied electrical current from an external wire creates a hotspot in part of the gate-source loop, breaking the superconductivity and allowing flux to enter or leave the loop randomly. (c) The number of fluxons in the loop has changed from n to m.

$I_{\mathrm{sw}}^{\mathrm{ch}}$ changes by 1 µA.

6.7 Outlook

In conclusion we have developed, characterized, and applied the yTron, a new superconducting device which is able to sense superconducting currents inline without perturbing them. We expect the yTron will find application as an inline current sensor for devices such as transition edge sensors and superconducting nanowire single photon detectors (SNSPD). In these devices, the yTron may be used to produce large (∼10 mV) ancillary outputs for multiplexing or time resolution purposes, without otherwise disturbing the primary readout method. Additionally, as a three-terminal controllable weak link, the yTron can serve as a logic or memory element with which to process and record detection events. Monolithic integration of the yTron with an SNSPD is feasible based on our previous work with the nanocryotron (nTron) which has similar fabrication to the yTron.

Since the yTron functionality comes from current crowding which occurs in every superconductor, it should be possible to fabricate it from any superconducting mate-

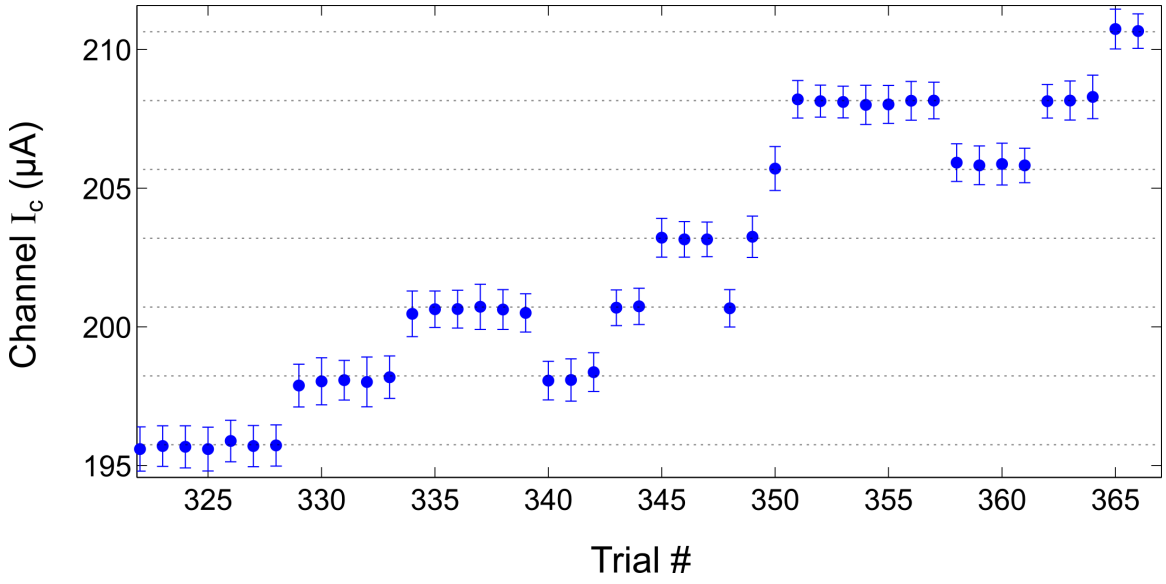

Figure 6-11: Sequential trials of measurements of a quantized superconducting loop using the yTron as an inline readout. Each dot corresponds to the median value of 100 measurements of the I_c of the yTron channel. The bars around each dot indicate the standard deviation of the I_c measurements for that trial. Between each trial, the loop was heated and cooled to allow fluxons to enter and leave. The step-like, evenly-spaced division of I_c values indicate that the yTron was able to read out the quantized current stored in the superconducting loop.

rial, although considerations must be made since the effective radius of curvature of the intersection point may be mitigated by the coherence length of the material. Additionally, the form of the yTron lends itself well to a CMOS-type fabrication scheme: it could be fabricated vertically by using a oxide layer between two superconducting thin films as the barrier between the gate and channel wires.

Chapter 7

Experimental techniques

In the process of testing the nTron, nanoSQUID, and yTron, a number of experimental techniques were developed that were common to all three. These techniques ranged from equipment automation using Python to building sample holders using a laser cutter.

7.1 Measurement and automation

7.1.1 Critical current measurements

Since all three devices were made from superconducting nanowires, it was crucial to have a consistent and well-characterized method of measuring the critical current I_c of the devices. Due to the dynamics that take place during the superconducting to resistive transition in a thin film, measurement of the switching current of a nanowire depends greatly on the readout and bias circuitry.

Factors that affect I_c measurement

At its most fundamental level, the transition from a superconducting to resistive state for a superconducting nanowire under a current bias is a stochastic process [97] [98]. Even neglecting quantum fluctuations which may vary I_c with time, there will always be Johnson-Nyquist noise [99] present on the nanowire. The presence of this

noise means that even with a fixed applied current, the actual current magnitude in the nanowire is constantly shifting. Outside of these internal processes, there are additional sources of noise such as thermally-radiated photons from the testing chamber [100], as well as ambient electromagnetic noise which can induce currents in the nanowire. These properties of the nanowire demand that I_c be measured as a distribution, not as a single measurement.

Even allowing that I_c is a distribution, there is no canonical I_c measurement: in fact, there are several measurement methods upon which the I_c value can be based, and all will produce different distributions (e.g. shift the median value of the distribution). Take for example a long nanowire like an SNSPD which has a large amount of kinetic inductance and a low shunt. When an SNSPD is current-biased, the nanowire will stochastically output pulses once the current bias is large enough. Clearly in the absence of light sources, the output pulses are the result of the wire being overbiased, but it is not clear whether the lowest bias value that produces a single pulse should be called I_c. Especially since this output pulse behavior is not universal to all nanowires–in short nanowires with low inductance, these pulses are often so small they cannot be read out by a standard amplifier setup.

Due to the properties of the NbN nanowire-based devices we often tested, we chose to interpret I_c as the latching current measurement for a wire. For a highly resistive material such as thin film niobium nitride, the latching current is very distinctive and straightforward to measure, regardless of device length or inductance [52] [54]. The latching current is characterized by the lowest current value at which the voltage across the device jumps from zero to a finite steady state value and does not return to zero. This current value corresponds to the creation of a resistive hotspot in the nanowire that is stable as long as the applied current bias is not reduced.

The one requirement for the latching measurement to be straightforward and easy to measure is that the nanowire readout must be hysteretic. In this instance, hysteresis means the nanowire will have a different I-V curve depending on whether current is swept in the positive direct or negative direction. This discrepancy occurs because a hotspot forms at high currents, and the presence of that hotspot can change

the point at which the nanowire transitions from resistive to superconducting.

If the nanowire is not hysteretic, instead of the readout voltage jumping sharply from zero to a finite voltage, there will instead be a gradual increase in voltage. The reasoning for this behavior is described in detail in Ref. [59], but for a brief explanation we will give the following example. Consider a 100-nm-wide nanowire with sheet resistivity R_s of $500\,\Omega/\square$ that is being measured by an oscilloscope with an input impedance of $1\,\Omega$. A current source inputs a current ramp which starts at zero and increases by $1\,\mu A$ per second. At $t = 8\,s$, the current in the nanowire is at $8\,\mu A$ and the wire is still fully superconducting, meaning the voltage is still zero. When the current reaches $9\,\mu A$ though, assume the nanowire can no longer carry all the current and enters the resistive state. However, this resistive state is actually a hotspot which when created always has a minimum size of on the order of the thermal diffusion length, which for NbN is $\sim$100 nm. At this point the nanowire has a resistivity of approximately one square, or $500\,\Omega$. Instead of flowing only through the nanowire, the current will then split between the nanowire and the oscilloscope, which as we specified has a resistance of $1\,\Omega$. As a result of this splitting, the majority of the current that was in the nanowire will be diverted to the oscilloscope input resistor, leaving the nanowire with only a few nanoamperes still passing through the resistive hotspot. As a result, the hotspot is able to cool, the superconducting state is restored, and once again the current begins to divert from the oscilloscope input impedance back into the nanowire, and the process repeats.

This oscillation is a well-known process called as relaxation-oscillation [3]. If we observe the voltage on the scope in this regime, we will either see a series of pulses, or if the pulse frequency is higher than the scope input bandwidth, the scope will just read the averaged voltage of the pulses which will be slightly above zero volts. If we increase the current bias to $10\,\mu A$ at this point, this dynamic process will shift slightly and spend more time in the hotspot state, and as a result the average voltage the scope reports will be increased slightly. As the current bias increases, the process of going into and out of the hotspot state will generate so much heat the wire will be transition to being completely resistive. However, this will not be a sharp transition

in the voltage readout, making it difficult to determine at which current value this occurs.

By the previous example, we can see how the nanowire switching process can actually be an unstable, dynamic process that depends on the external readout circuit. The load impedance the nanowire sees can affect the measurement process–a low load impedance will cause the nanowire to be non-hysteretic, robbing us of the sharp superconducting to resistive transition seen in hysteretic nanowires. Taking this a step further, even when the nanowire is hysteretic changing the load impedance can shunt the quantum and thermal noise in the nanowire, changing the I_c distribution. Another factor that affects the I_c distribution is the rate at which the applied current bias is ramped. Due to the stochastic nature of the switching, the higher the current ramp rate (larger A/s) the larger the median of the I_c distribution will be. Thus, it behooved us to find a consistent method that allowed for a straightforward, repeatable implementation of I_c measurements.

The standardized I_c measurement

The testing setup used to measure the nTron, nanoSQUID, and yTron I_c can be constructed with common lab equipment. Specifically, what is needed are an oscilloscope, an arbitrary waveform generator (or sine wave voltage source), lowpass filters, and resistors in RF-shielded boxes. A typical setup is shown as a circuit schematic in Fig. 7-1.

For our setup, we used a LeCroy 620Zi oscilloscope, which allowed for remote control using a Python interface. This remote interface is detailed in Section 7.1.2. This oscilloscope had an input bandwidth of 2 GHz, but since we were only interested in voltage measurement timescales on the order of microseconds, we internally limited the bandwidth to 20 MHz in order to reduce high-frequency noise. To generate the current ramp, we used a Agilent 33250a arbitrary waveform generator (AWG) to generate a voltage ramp. As shown in Fig. 7-1, the AWG voltage output was connected to the scope channel 1 to serve as a reference, and was also split off and connected to a 10 kΩ resistor. The AWG additionally had a 1.9 MHz lowpass filter

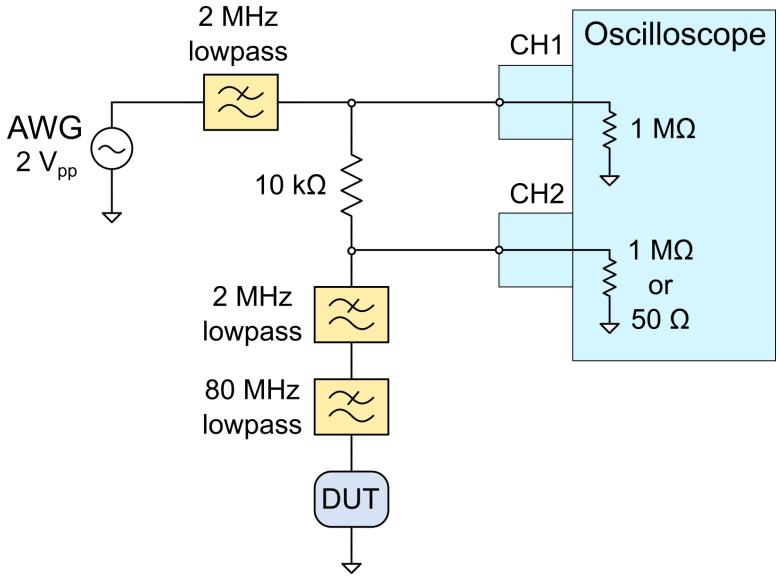

Figure 7-1: Circuit diagram of the I_c sweeping setup. DUT stands for "Device Under Test" and refers to the nanowire being measured. The arbitrary waveform generator (AWG) was a Agilent 33250A, the 2 MHz lowpass filter was a Mini-Circuits BLP-1.9+, and the 80 MHz lowpass filter was a high-rejection Mini-Circuits VLFX-80+.

in front of it, to block digital noise caused by the internal digital-to-analog converter (DAC). The resistor was in series with the nanowire and converted the voltage signal to a current signal, such that one volt at the AWG produced 100 µA through the nanowire. Channel 2 of the oscilloscope was then connected between the resistor and nanowire to serve as the device output voltage in a two-wire measurement setup. Although a four-wire measurement would have been more exact, these measurements typically produced tens of millivolts of output voltages. A two-wire measurement was more than adequate due to the comparatively small voltage drops along the connections. Both oscilloscope channels had their input impedances set to DC 1 MΩ input impedance, to guarantee the nanowire saw a high load impedance and would remain hysteretic.

All of the connections were made using BNC or SMA coaxial cables, in order to shield the device from high-frequency RF noise from the environment. Exposing a small unshielded area (such as using a resistor not in an RF-tight box) made it possible to see spurious radiation from cell phones and FM radio stations on the oscilloscope readout. To further ensure the isolation of the device from high frequency noise,

lowpass filters were placed at all connections facing the device, as can be seen in Fig. 7-1. Two types of lowpass filters were used in series: high-rejection lowpass filters (Mini-Circuits VLFX-80+), which absorbed frequencies from 80 MHz up to 20 GHz, and lower-frequency lowpass filters (Mini-Circuits BLP-1.9+) which absorbed frequencies down to 1.9 MHz but had poor absorption above 200 MHz.

With this setup in place, the I_c sweep measurement was ready to begin. The AWG was set to produce a 200 Hz, 20 V_{pp} sine waveform, so that the device current was swept between ± 1 mA every few milliseconds. This timescale was chosen because it often took several tens of microseconds for the voltage to reach steady-state once the device had latched. This settling time occurred because at low frequencies the coax cabling and lowpass filters looked like they had capacitances to ground of several nanohenries. Because of the nanohenry-scale capacitance, the RC time constant for transient effects was the series resistance time the capacitance, $10\,\mathrm{k\Omega} \times 1\,\mathrm{nH} = 10\,\mu\mathrm{s}$. Since we wanted the voltage readout to reflect the steady-state value as we swept the current, we needed the transient timescale to be much shorter than the current ramp timescale. It was also important to make the sine wave V_{pp} large enough such that the measured I_c occurred during the approximately-linear portion of the sine wave voltage, so that the ramp rate (which affects the I_c distribution) was approximately constant during the superconducting to resistive transition. Typically, this meant adjusting the AWG V_{pp} such that the current ramp swept to at least twice the measured I_c.

While the equipment for the I_c sweep was initially set up, it produced an output on the oscilloscope that looked like Fig. 7-2. As shown in that figure, the oscilloscope simultaneously reads out the AWG reference voltage as well as the nanowire voltage. Then by triggering on the rising edge of the device voltage (the jump from the superconducting to resistive state), the reference voltage at that point was recorded as a single I_c measurement. This process was typically repeated 100 to 1,000 times to produce the I_c distribution. Since we were using a digital oscilloscope, however, some factors had to be taken into account in order to get an accurate reading of the reference voltage. These factors are detailed in the following section.

Figure 7-2: Oscilloscope voltage traces for an I_c sweeping measurement. Shown in yellow is the sine-wave reference voltage produced by the AWG. In pink is the voltage of the device under test (in this case an SNSPD).

Avoiding digital noise in the I_c measurement

Initially, the technique for extracting the I_c current from the measurement setup was as follows: (1) trigger on the superconducting to resistive voltage jump; (2) at the trigger/jump point, take the corresponding voltage datapoint from the AWG reference voltage; (3) Divide this voltage datapoint by the series resistance to get I_c.

However, while taking thousands of I_c measurements, we found that there were strange striations in the resulting histogram which did not seem to correspond to any physical phenomenon. Normally, the I_c sweep distribution should look like a smooth Gumbel distribution [101] of the form $P(x) = \exp\left(-(x + e^{-x})\right)$. However, as shown in Fig. 7-3 the general shape of the distribution was correct, but it was not smooth. The distribution looked like it suffered from digital noise, but at the same time it was not purely digital noise because the striations were not the result of truncated bits, which would make most bins of the histogram zero.

It appeared the full distribution was actually comprised of periodic Gaussians of

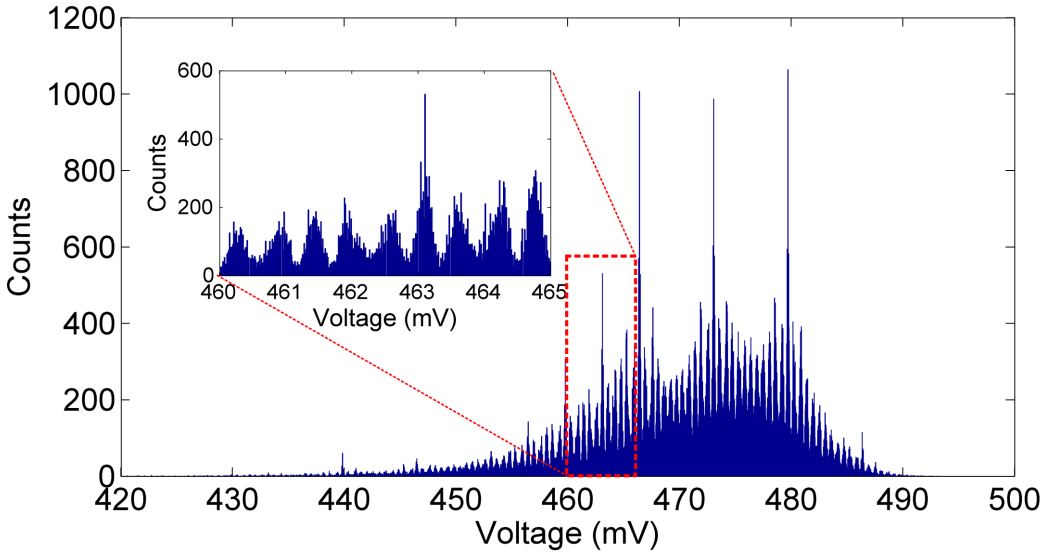

Figure 7-3: I_c sweep distribution measurement, shown in terms of the raw voltage (to convert to the I_c current divide by 10 kΩ). The I_c was swept 300,000 times to build this histogram. (inset) Zoomed portion of the distribution showing the unexpected striations (periodic Gaussian-like shapes) of the measured distribution. These striations were due to the digital nature of the digital oscilloscope.

different heights. At first we believed this was the result of the AWG producing a very digitized sine wave with discrete steps. This would have made sense beaus the AWG is fundamentally just a high-speed digital-to-analog converter (DAC), so possibly what we were seeing was that each sub-Gaussian corresponded the noisy measurement of single-bit DAC step. But no matter what we did to filter the AWG output – we tried many combinations of bandpass and lowpass filters – the striations would not disappear from the measurement.

We then decided it could be a problem with the actual scope measurement. In our initial implementation, the scope waited for the nanowire voltage jump, then it read the datapoint of the AWG voltage at that time to determine I_c. But the problem with this approach was that the voltage datapoints were digitally recorded. In the example shown in Fig. 7-3, each sub-Gaussian is about 0.1 mV, which for the scope measurement settings (20 mV/div) corresponds to about 11 bits of precision. That is close to the edge of how well a very fast analog-to-digital converter (ADC) can function, so any precision beyond those 11 bits is essentially just the scope guessing.

With this discovery, it became clear that it was not a good idea to just pick one datapoint from the AWG reference waveform and use only that datapoint for the switching current. Instead, we slightly changed the way the scope read out I_c: when the scope triggered on the nanowire, we then took the mean of several thousand datapoints of the AWG reference voltage around the trigger time. Since the AWG reference voltage was slowly-varying, these several thousand datapoints were essentially the same voltage level, comprising only a few hundred nanoseconds worth of data. We accomplished this mean function by zooming the scope to 200 ns of width, and using the built-in scope mean function to generate a single value from the all the datapoints in the (approximately flat) AWG voltage waveform.

By taking the average of several thousand datapoints, we were able to greatly increase the accuracy of each individual I_c reading. After running another sample test, we were able to get the smooth Gumbel distribution we initially expected. This distribution is shown in Fig. 7-4 and represents the measurement technique used for all I_c distribution measurements listed in this thesis.

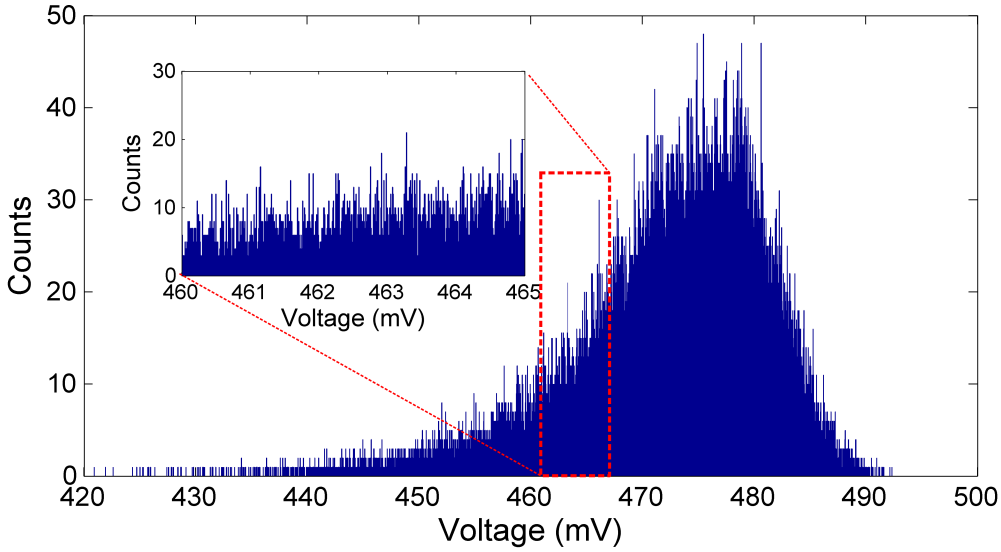

Figure 7-4: I_c sweep distribution measurement with the improved measurement technique, eliminating the striations in the distribution (to convert to the I_c current divide by 10 kΩ). The I_c was swept 58,000 times to build this histogram. (inset) Zoomed portion of the distribution showing the corrected distribution which does not have periodic behavior.

7.1.2 Measurement automation with Python

The ability to control experimental equipment remotely was crucial to configuring repeatable measurements with as little setup time as possible. By writing functions and scripts in Python, we were able to build standardized test configurations that could be implemented in a few seconds, rather than tens of minutes of manual setup. It also allowed us to ensure that the measurement setup was the same each time; as long as the script configuring the equipment interface remained the same, the resulting equipment configuration was the same. The Python code which was used to control the equipment described in this thesis can additionally be found in Appendix A.

Remote control of equipment using GPIB

Many pieces of scientific equipment come with the ability to be remotely controlled. Typically, communications with the instrument is accomplished using a General Purpose Interface Bus (GPIB). The GPIB interface specification is also known as IEEE-488 and dates back to the 1960s, but is often still implemented on modern equipment due to its robust operation and long history as a standard equipment communications protocol. The physical GPIB setup typically consists of a single GPIB controller (which plugs into a computer using USB) which is connected by GPIB-specific cables to several pieces of equipment. These two components are shown in Fig. 7-5. Each piece of equipment has an address associated with it (usually between 1 and 24), and the computer can send messages or queries to a specific instrument by specifying its address to the controller. Thus, the controller handles the signal-level communications protocol, and the computer just needs to provide (1) the GPIB address of the instrument and (2) the message to send to the instrument. The messages sent by the computer to the instruments are typically text strings. These strings can either be queries, which generate a response, or commands which direct the instrument to perform some function and do not generate a response. Sending a query is usually a two step process: first, the computer issues a query command, and second, the computer reads the text string response from the instrument.

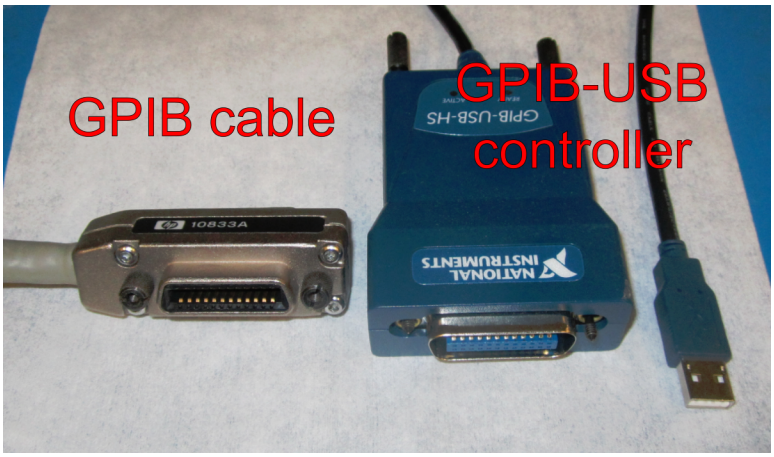

Figure 7-5: Photograph of a GPIB cable connector and a GPIB-USB interface.

Automating measurements using Python and GPIB

The majority of the measurements done in this thesis were performed using Python scripts which controlled instruments through a Python-GPIB interface. The Python software package used to talk to the GPIB was called PyVISA. PyVISA abstracts simple command/response communications for several types of protocols (TCP/IP, LXI, GPIB) away from the details of the protocol and lets the user communicate with instruments using simple Python commands.

Instruments are created in Python by specifying a GPIB address to PyVISA. PyVISA will then return an object which represents the instrument. The user can then interact with the instrument by using the instrument-object functions `read` and `write`.

A typical Python interaction with an instrument works like the following example which describes reading the voltage on a Keithley 2001 multimeter. The user first finds the GPIB address of the instrument (typically found in the instrument's configuration) and uses that address with PyVISA to create a Python object representing that instrument, for example `my_multimeter`. The user then looks up the command for the desired action, in this case reading out a voltage. Commands for a given piece of equipment are usually listed and described in a section of the equipment manual called "Remote Programming", "SCPI Command Reference", or similar. In this case, the Keithley 2001 multimeter command to read a voltage can

be found in the "IEEE-488 Reference" section of the manual, and is listed as the command `READ?`. The user can send this command to the instrument using the `write` command of the `my_multimeter` object, so that the full Python command is `my_multimeter.write('READ?')`. The string `'READ?'` will then be received and processed by the multimeter, and since the string is a command that asks for a response (usually indicated by a question-mark at the end of the command string), the instrument will return a response string. If the Keithley multimeter had a voltage of 3.81 V attached to it, it would send the response string `'3.81'`. This response string sits in an input buffer when it is received by the computer, so it is not assigned to any Python variable until the `read` function is issued. To put the response string into the Python variable `the_voltage`, the user issues the command `the_voltage = my_multimeter.read()`. At this point, the string `'3.81'` is contained in the variable `the_voltage` and can be saved, converted to a floating point number, etc.

7.2 Sample holder design

The sample holders that were used to test the devices described in this thesis were built out of low-cost materials and designed to allow for fast testing turnaround.

7.2.1 Sample holder construction

Although most superconducting experiments take place in a cryogenic vacuum environment with careful attention paid to the rate of cooldown and vacuum properties, the thin films we tested were found to be very resistant to moisture and extreme thermal shock. We routinely cooled our superconducting nanostructures from room temperature to 4.2 K in under a minute by submerging the samples directly into a dewar of liquid helium, and observed no degradation in metrics of import such as I_c, R_s, or T_c. These samples were often removed from the liquid helium without special precautions as well, and often there would be significant condensation left on the devices as they warmed up–but again no pattern of degradation was observed.

This quick cooldown time allowed us to design, fabricate, and test superconducting

devices with a total turnaround time as low as 24 hours, but also required us to make some special considerations when building the sample holder. For instance, due to the submersion into liquid helium, it was important that the sample holders were built from low-heat-capacity materials that would not boil off large amounts of expensive liquid helium [102]. The sample holder also had to withstand the thermal shock from the cooling process, and not break or detach due to thermal expansion. Additionally, the holder needed to be sized such that it could fit down the neck of the dewar, and be detachable from the submersion stick so that it can be brought to the wirebonder for making electrical connections.

We found that an effective sample holder design consisted of an acrylic base, an acrylic cover, a clip to mechanically hold down the (typically 1×1 cm) sample, a PCB with which to make electrical connections, and a rod for dropping the sample into the liquid helium. We typically cut the acrylic base and cover out of a large piece of acrylic using a laser cutter. This allowed for rapid prototyping of sample holder designs. Some finished examples of the sample holder are shown in Fig. 7-6 and .

The first step we took when constructing the sample holder was to design a to-scale 2D representation of the holder in the open-source vector graphics software package Inkscape. Our dewar mouth had a diameter of approximately 5 cm, and so the holder base was typically designed to be long and narrow, about 3 to 4 cm wide by 10 cm long. One example design is shown in Fig. 7-8. Since there were no large mechanical forces being applied to our test setup, creating holes in the acrylic for 4-40 tapping was adequate for most mechanical connections. In the design, we chose to use exclusively 4-40 screws in order to reduce the complexity of assembling and disassembling the holder. Once the vector design for the base was completed, the design was cut out from a sheet of acrylic 1/4 inch thick.

Once the sample holder base was complete, a custom PCB was designed and fabricated (either by a PCB foundry or the process detailed in Section 7.2.2) to carry electrical signals to the sample. This PCB typically had traces leading up to the 1×1 cm sample area. The aluminum wirebonds we used unfortunately were not able to bond to the solder coating on these traces, likely because the solder was too

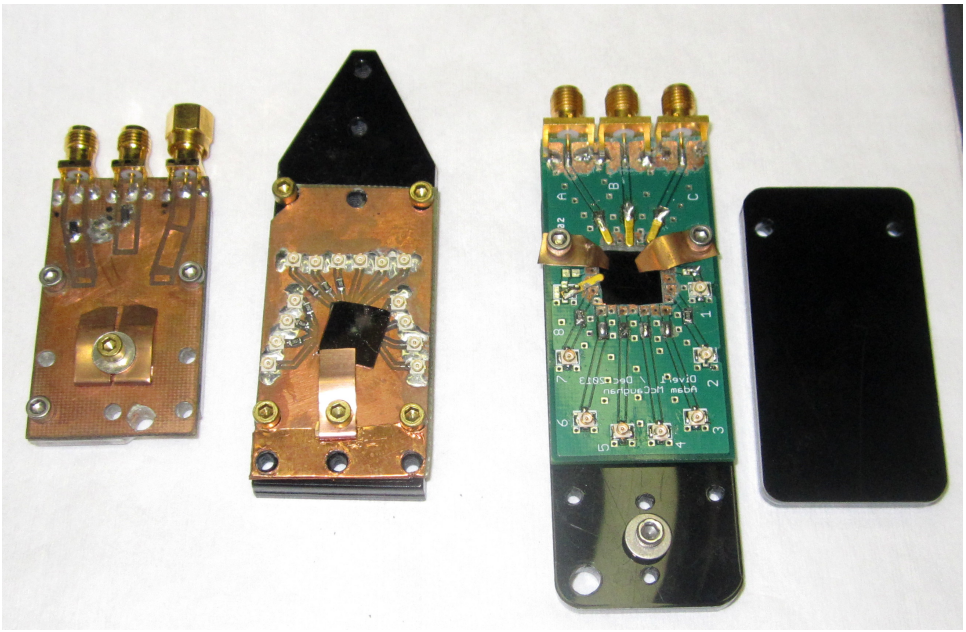

Figure 7-6: Photograph of three different custom-built sample holders. The two sample holders on the left were constructed from PCBs that were fabricated in-house using the etching process described in this thesis. The other sample holder (green PCB) had a PCB which was designed in-house but purchased from a commercial PCB company.

soft for the ultrasonic bonding process. Initially, we ground the solder off with a dremel to expose the underlying copper trace, but often that copper would oxidize after a few days and require re-polishing before wirebonds would successfully stick again. We found that the best solution to make a robust wirebonding target was to cut the ends off of a gold-coated pin header or other gold-coated part and solder it down to the PCB trace. These parts typically had an electroplated gold finish several tens of nanometers thick, which provided an ideal wirebonding target surface. The result of soldering a gold-coated part (Digikey part number 1003-1626-ND) is shown in Fig. 7-9. On the other end of the PCB trace was a microwave connector such as SMA, SMP, or U.FL which attached to a coax and led to the room-temperature electronics. Because we were submersing the whole holder into liquid helium, we had a significant amount of cooling power and were able to use standard flexible copper coaxial cables without worries of inadvertently heating the sample.

Samples were typically held in place by a beryllium copper (BeCu) clip. The

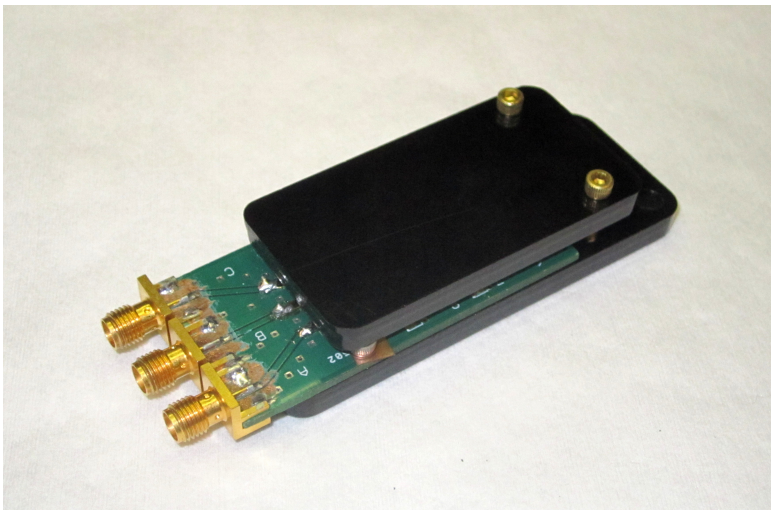

Figure 7-7: Finished sample holder with cover on top.

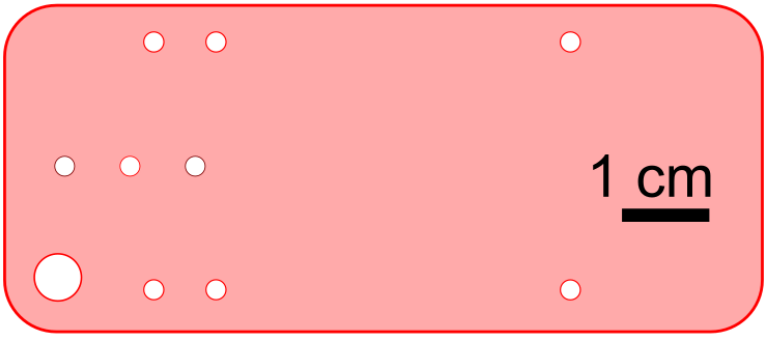

Figure 7-8: Vector drawing for an acrylic sample holder drawn in Inkscape. All of the solid lines represent cuts performed by the laser cutter. The smallest holes are holes meant for 4-40 tapping

clip material was chosen because BeCu is one of the few materials which retains its spring-like characteristics even at cryogenic temperatures–many other materials become hard and brittle [102]. Custom-shaped BeCu was expensive, and sheets of BeCu were difficult to form, but we found a solution by ordering BeCu "finger stock". This type of item is typically sold in long strips and is used for shielding purposes, but we repurposed it by cutting short sections and using their spring-like qualities to pin down the sample. Two examples of these clip can be seen in Fig. 7-6.

Once the sample holder components were complete, assembly for testing was ready. The sample would be loaded into the BeCu clip, electrical connections would be made by wirebond from the PCB traces to the devices on the sample, and the cover was

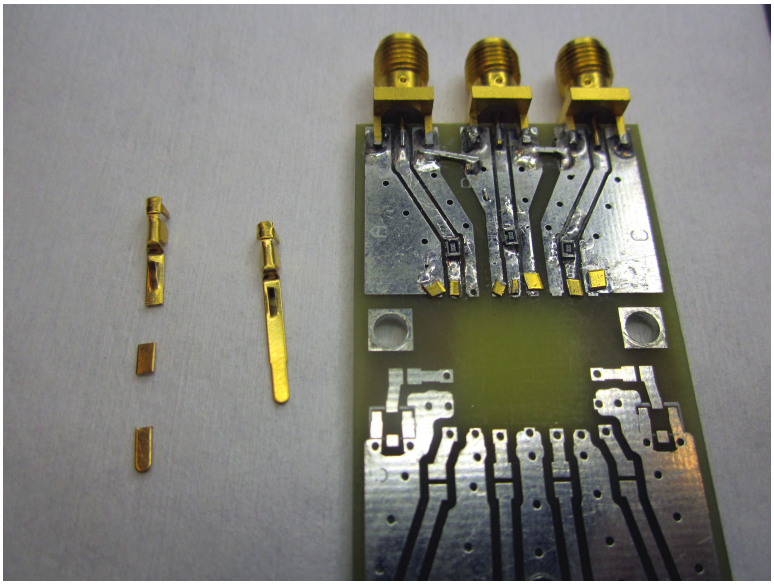

Figure 7-9: Photograph of gold-coated components which have been cut into pieces and soldered to the PCB to act as a wirebonding targets.

screwed down on top of the assembly to prevent inadvertent contact with the sample or wirebonds. Altogether, the assembly was very robust and only infrequently were there mechanical problems such as detaching wirebonds. The PCB would then have coaxial cables attached to it, and the whole assembly would be mounted on the end of a thin stainless steel tube for submersion.

7.2.2 In-house PCB fabrication

For many of the experiments detailed in this these, PCBs were commonly used as sample holders since they allowed for easy integration of lumped element circuit components, and were bondable with the wirebonding processes needed to connect to the gold pads of the samples. Unfortunately, many PCB foundries can take days or sometimes weeks to fabricate and ship a simple PCB. This is confounded further by the requirement to learn EAGLE or an equivalent circuit-layout program to produce the Gerber files necessary for the foundries. In many cases the sample holder PCBs were simply a few traces on one side of the PCB, and did not require the advanced routing techniques available in the circuit-layout program. Instead, these traces can be drawn in a basic graphics design program such as Inkscape.

We discovered that the Epilog Mini laser cutter we used to cut acrylic could be used as a raster patterning tool for patterning simple PCBs. Were were successfully able to fabricate PCBs with features sizes of less than 0.5 mm using this technique. This resolution could likely be improved with further optimization. Here we describe the PCB fabrication technique from start to finish. First, the supplies that are needed are:

- Laser cutter
- Copper-clad PCB board
- Spraypaint (Used Krylon "Eco-Guard" Latex Enamel spraypaint, black, worked well because it was fast-drying and low odor.)
- Isopropyl alcohol
- Ferric chloride copper etchant

As shown in Fig. 7-10 first coat the copper side of the PCB in a thin layer of spraypaint. After coating, allow it to dry – putting it on a hotplate at $\sim$60 °C will speed this up greatly. It may be desirable to put a piece of foil over it while drying to prevent dust from landing and sticking to the surface. Put a second coat on and allow that to dry as well. It should be dry to the touch, but leaving it out longer (or baking) is recommended to get as much of the spraypaint solvent out as possible. If the PCB is copper-clad on both sides, and it is necessary to keep the backside copper as a ground-plane, cover the backside with two coats of spraypaint as well.

The next step is to design the pattern in Inkscape or another favorite graphic design program. Save the design as a PDF for laser cutter. This format works well because the laser cutter acts as a printer and the most compatible format for raster printing is PDF. In this example, the design shown in Fig. 7-12 will be patterned onto the copper. In this process, the spraypaint acts as a etch resist and the laser cutter ablates the spraypaint off where the design is black. As a result, areas of the design that are black will have their copper exposed and subsequently etched. Areas that are white on the design will be leftover as bare copper.

Figure 7-10: (left) Bare copper PCB board used as the blank substrate for PCB patterning. (right) The same copper PCB board, covered with two coats of black spraypaint.

The next step is to send the design file PDF to the laser cutter printer. The settings used for the Epilog Mini laser cutter are:

- Raster mode
- 400 dpi (this can be increased, but not usefully)
- Power 100 %
- Speed 40 %

As laser cutter is printing (shown in Fig. 7-11), it should be possible to see the pattern take form. Once it's done, the pattern should be fully printed but there will be burned spraypaint left over in the exposed areas, which is the result of the laser ablation not fully removing all of the spraypaint. This leftover spraypaint needs to be removed that so it does not affect the etching. This removal process is done but this by using a Q-tip that's very slightly damp with isopropyl alcohol. Run the q-tip

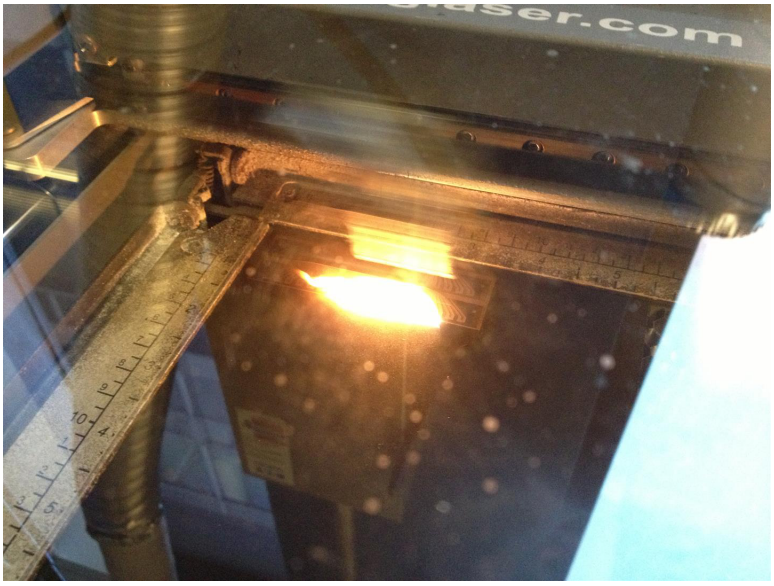

Figure 7-11: Laser cutter in the process of patterning the spraypaint on the surface of the PCB board.

along the various traces and areas until the copper start to shine. We had to be careful about pushing too hard or using too much isopropyl alcohol; both the leftover and untouched spraypaint are soluble and pushing too hard may wipe away the finer details of the pattern. This difference between the cleaned and uncleaned sections is shown in Fig. 7-13. As a result, left with a very high-contrast pattern, shiny copper and black paint.

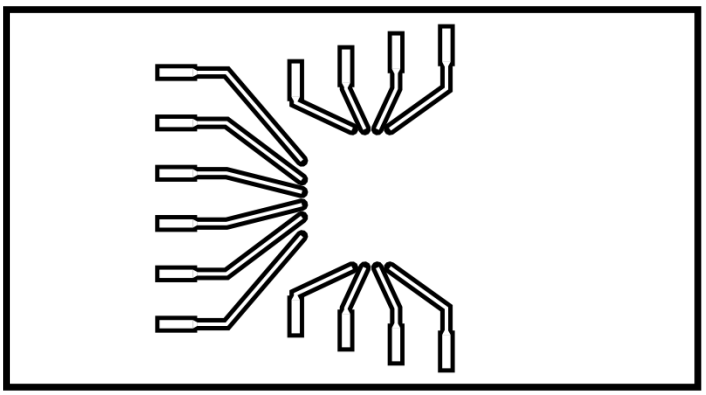

Figure 7-12: PCB design made in Inkscape. Areas which are black will be "printed" by the laser cutter, exposing the bare copper and allowing those areas to be etched. Areas in white will be copper in the finished PCB.

The next step is to cut the patterns out of the PCB and drop them into a solution

Figure 7-13: The laser-patterned PCB, parts of which have been cleaned with a Q-tip soaked in isopropyl alcohol. Before etching, the entire pattern should be as shiny as the original bare copper was before spraypaint application.

of ferric chloride (FeCl). Warm the FeCl solution on a hotplate set to 80 °C. We purchased the FeCl from a local electronics store, and it took about 15 min to start seeing the etch, and about 30 min to fully etch the copper. The PCB etch progress needs to be checked often, the timing can vary significantly even between identical PCBs due to some of the spraypaint slowly dissolving and clogging up the solution. The final step is to wash away the spraypaint. The paint we used was very soluble in acetone, so a little bit of scrubbing with a clean-wipe and acetone removed it completely. The final result is shown in Fig. 7-14.

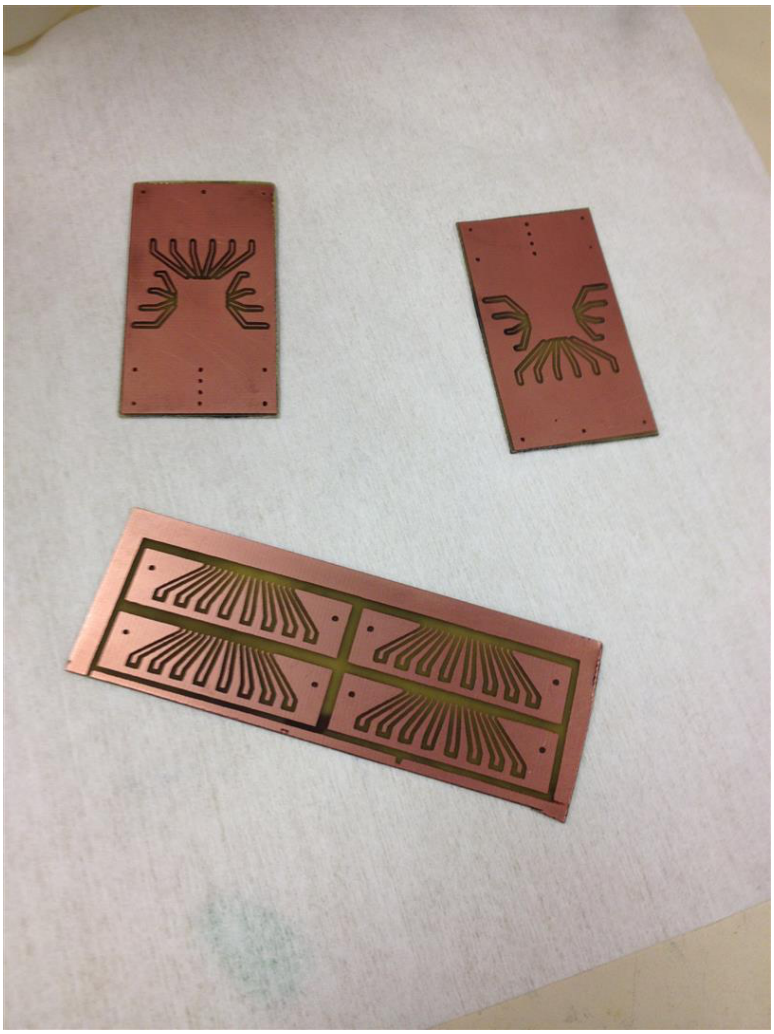

Figure 7-14: The final product from the in-house PCB fabrication process using the laser cutter.

Chapter 8

Conclusion and outlook

Superconducting devices are presently being used in a diverse set of applications in an equally diverse set of fields. Broadly speaking, devices which are made from superconductors fall into two categories: phase-based devices and magnitude-based devices. Several magnitude-based devices are currently employed as sensors (e.g. SNSPDs, MKIDs, TESs), and the phase-based Josephson junction has been successful as a electronics element (e.g. RSFQ).

However, in the realm of superconducting devices there is still much left to do. For instance, although the Josephson junction is both fast and low-power, it cannot be easily interfaced with external technologies which require high input voltages (e.g. CMOS). And although devices like the SNSPD and TES are excellent sensors, they are often amplified by noisy, non-superconducting sources.

To help fill these gaps in functionality, this thesis described the development of several new devices made by nano-patterning superconducting thin films into 2D geometries. Superconducting thin films form an ideal platform on which to take advantage of both the phase and magnitude in a superconductor: in a thin film the magnitude of the superconducting state can be weakened locally (e.g. the nTron), and the phase can be manipulated directly by injected current flow (e.g. the current-biased nanoSQUID).

Although this thesis has described a small handful of implementations for the nTron, yTron, and current-biased nanoSQUID, there are also several applications

which should be possible for the near future. For instance, the nTron has operating characteristics which are complementary to Josephson-junction-based technologies, and integration could enable those technologies to perform otherwise-difficult tasks such as memory line-driving and fanout in exascale computing. Additionally, the ease of fabrication, transistor-like logic-gate design, and extensibility to other materials mean that small-scale superconducting circuits are now accessible with minimal fabrication investment and straightforward circuit designs.

The current-biased nanoSQUID may find use as a convenient metrological tool to measure kinetic inductances in thin films, since accurately measuring the inductance of the nanoSQUID only requires that a few DC wires. Additionally, it may find use as a feedback tool for scanning SQUID microscopy.

One of the most potentially interesting uses of the yTron would be to use it as a three-terminal controllable weak link for single-flux quantum logic. By forming loops between the gate and drain and source and drain, flux flow into the source-drain loop can be controlled by flux stored in the gate-drain loop. In future work, the yTron may be used inline with transition-edge sensors or superconducting nanowire single-photon detectors to provide extra, high-impedance outputs.

Appendix A

Python equipment automation code

This appendix contains Python code for the control and automation of several different scientific instruments, which was critically enabling to the measurement of the devices described this thesis. Each instrument is given its own Python class, based on the PyVISA 1.3 instrumentation framework.

LeCroy 620Zi Oscilloscope

```
from pyvisa import visa
import numpy as np
import time
import datetime

class LeCroy620Zi(visa.Instrument):
    """Python class for LeCroy Oscilloscope, written by Adam McCaughan.  Most of
        these commands
    originate from the Automation Command Reference Manual for WaveRunner
        Oscilloscopes"""

    def __init__(self, args):
        super( visa.Instrument, self).__init__(args)
        self.write('COMM_HEADER OFF') # Get rid of the leading 'VBS ' crap
        self.write('COMM_FORMAT DEF9,WORD,BIN') # Set output to 16 bits of
            information (a 'word') per datapoint


    def round_up_lockstep(self, x):
        """ Some functions on the LeCroy require numbers to be rounded up to
            nearest 1,2 or 5
        e.g. 1.2e-6 -> 5e-6 and 4.7e0 -> 5e0 """
        x_str = '%0.9e' % x  # Takes 1234.24e-10 -> '1.234240000e-07'
        x_digits = x_str[:-4] #  Takes '1.234240000e-07' -> '1.234240000'
        x_exp = x_str[-4:]
        if float(x_digits) <= 1:      locked_x = '1'
        elif float(x_digits) <= 2:    locked_x = '2'
        elif float(x_digits) <= 5:    locked_x = '5'
        else:                         locked_x = '10'
        return float(locked_x + x_exp)
```

```
def vbs_ask(self,message):
    vbs_msg = 'VBS? \'return = %s\'' % message
    # print 'Sending command:  ' + vbs_msg
    return self.ask(vbs_msg)


def vbs_write(self,message):
    vbs_msg = 'VBS \'%s\'' % message
    # print 'Sending command:  ' + vbs_msg
    self.write(vbs_msg)


def reset(self):
    self.write('*RST')
    self.write('COMM_HEADER OFF') # Get rid of the leading 'VBS ' crap
    self.write('COMM_FORMAT DEF9,WORD,BIN') # Set output to 16 bits of
        information (a word) per sample
    time.sleep(1)


def clear_sweeps(self):
    self.vbs_write('app.ClearSweeps') #
    time.sleep(0.2) # Necessary to allow the scope time to reset all values


def view_channel(self, channel = 'C1', view = True):
    if channel[0] == 'C':  # If it's C1, C3, etc
        self.vbs_write('app.Acquisition.%s.View = %s' % (channel, view))
    elif channel[0] == 'F': # If it's F1, F2...
        self.vbs_write('app.Math.%s.View = %s' % (channel, view))


def set_coupling(self, channel = 'C1', coupling = 'DC1M'):
    """ Coupling should be either AC1M, DC1M, DC50, or Gnd """
    self.vbs_write('app.Acquisition.%s.Coupling = "%s"' % (channel, coupling))
```

```
def get_coupling(self, channel = 'C1'):
    """ Coupling should be either AC1M, DC1M, DC50, or Gnd """
    return self.vbs_ask('app.Acquisition.%s.Coupling' % (channel))


def set_bandwidth(self, channel = 'C1', bandwidth = 'Full'):
    """ Bandwidth should be either 1GHz, 200MHz, 20MHz, 3GHz, 4GHz, Full """
    self.vbs_write('app.Acquisition.%s.BandwidthLimit = "%s"' % (channel,
        bandwidth))


def set_vertical_scale(self, channel = 'C1', volts_per_div = 1, volt_offset =
    0):
    # Lecroy only allows digits 1, 2, and 5.  e.g. 5e-6 is acceptable, 4e-6 is
         not
    volts_per_div = self.round_up_lockstep(volts_per_div)
    self.vbs_write('app.Acquisition.%s.VerScale = %0.0e' % (channel,
        volts_per_div))
    self.vbs_write('app.Acquisition.%s.VerOffset = %0.0e' % (channel,
        volt_offset))

def find_vertical_scale(self, channel = 'C1'):
    self.vbs_write('app.Acquisition.%s.FindScale' % channel)


def set_horizontal_scale(self, time_per_div = 1e-6, time_offset = 0):
    self.vbs_write('app.Acquisition.Horizontal.HorScale = %0.6e' %
        time_per_div)
    self.vbs_write('app.Acquisition.Horizontal.HorOffset = %0.6e' %
        time_offset)

def set_memory_samples(self, num_samples = 1e6):
    self.vbs_write('app.Acquisition.Horizontal.MaxSamples = %0.3e' %
        num_samples)
```

```
def set_trigger(self, source = 'C1', volt_level = 0.1, slope = 'positive'):
    """ Slope should be "Either" / "Negative" / "Positive" """
    self.vbs_write('app.Acquisition.Trigger.Source = "%s"' % source)
    self.vbs_write('app.Acquisition.Trigger.%s.Level = %0.4e' % (source,
        volt_level))
    self.vbs_write('app.Acquisition.Trigger.%s.Slope = "%s"' % (source, slope)
        )


def set_trigger_mode(self, trigger_mode = 'Normal'):
    """ trigger_mode should be set to Auto/Normal/Single/Stop """
    self.vbs_write('app.Acquisition.TriggerMode = "%s"' % trigger_mode)


def set_persistence(self, channel = 'C1', persistence = False, monochrome =
    False):
    self.vbs_write('app.Display.LockPersistence = "PerTrace"')
    self.vbs_write('app.Acquisition.%s.Persisted = %s' % (channel, persistence
        ))
    self.vbs_write('app.Acquisition.%s.PersistenceMonochrome = %s' % (channel,
         monochrome))


def label_channel(self, channel = 'C1', label = 'Channel 1 label text'):
    if (label == '') or (label == False) or (label == None):
        self.vbs_write('app.Acquisition.%s.ViewLabels = False' % channel)
    else:
        self.vbs_write('app.Acquisition.%s.LabelsText = "%s"' % (channel,
            label))
        self.vbs_write('app.Acquisition.%s.ViewLabels = True' % channel)


def set_display_gridmode(self, gridmode = 'Auto'):
    """ gridmode should be Auto / Dual / Octal / Quad / Single / XY / XYDual /
```

```
        XYSingle """
    self.vbs_write('app.Display.GridMode = "%s"' % gridmode)


def set_parameter(self, parameter = 'P1', param_engine = 'Maximum', source1 =
    'C1', source2 = None, show_table=True):
    """ Possible param_engine values listed in a table on page 1-151 of the
        automation manual.
    Some sample param_engine values are:
    Frequency / LevelAtX / Fall / Maximum / Mean / Median / Minimum /
        PeakToPeak """
    self.vbs_write('app.Measure.ShowMeasure = %s' % show_table)
    self.vbs_write('app.Measure.%s.ParamEngine = "%s"' % (parameter,
        param_engine))
    if source1 is not None:
        self.vbs_write('app.Measure.%s.Source1 = "%s"' % (parameter, source1))
    if source2 is not None:
        self.vbs_write('app.Measure.%s.Source2 = "%s"' % (parameter, source2))
    self.vbs_write('app.Measure.%s.View = True' % parameter)


def set_math(self, math_channel = 'F1', operator = 'AbsoluteValue', source1 =
    'C1', source2 = None):
    """ Possible operator values listed in a table on page 1-151 of the
        automation manual.
    Sample values include: Average / Trend / Histogram / FFT / Integral / etc
        """
    self.vbs_write('app.Math.%s.Operator1 = "%s"' % (math_channel, operator))
    if source1 is not None:
        self.vbs_write('app.Math.%s.Source1 = "%s"' % (math_channel, source1))
    if source2 is not None:
        self.vbs_write('app.Math.%s.Source1 = "%s"' % (math_channel, source2))


def get_parameter_value(self, parameter = 'P1'):
```

```
        return float(self.vbs_ask('app.Measure.%s.Out.Result.Value' % parameter))



def get_trigger_mode(self):
    return self.vbs_ask('app.Acquisition.TriggerMode')



def get_wf_data(self,channel='C1'):  # e.g. channel = C1 or F3 etc
    ADDR_VGAIN = 156
    ADDR_VOFFSET = 160
    ADDR_HINTERVAL = 176
    ADDR_HOFFSET = 180
    databytes = self.ask(channel + ':WAVEFORM? DAT1') # Contains waveform data
    databytes = databytes[16:]  # Strips leading header data
    if len(databytes) == 0:
        return np.array([]), np.array([])
    if len(databytes) % 2 == 1: # Sometimes accidentally returns an extra byte
        databytes = databytes[:-1]
    data = np.frombuffer(databytes, np.int16)
    # DESC contains info about vertical/horiz scaling, etc,
    # see P280, Appendix II Remote Control Manual for byte addresses
    desc = self.ask(channel + ':WAVEFORM? DESC')
    desc = desc[16:]
    vgain = float(np.frombuffer(desc[ADDR_VGAIN:ADDR_VGAIN+4], np.float32))
    voffset = float(np.frombuffer(desc[ADDR_VOFFSET:ADDR_VOFFSET+4], np.
        float32))
    hinterval = float(np.frombuffer(desc[ADDR_HINTERVAL:ADDR_HINTERVAL+4], np.
        float32))
    hoffset = float(np.frombuffer(desc[ADDR_HOFFSET:ADDR_HOFFSET+8], np.double
        ))
    num_samples = len(data)
    x = np.array(range(num_samples))*hinterval + hoffset
    # yscale = float(2**16)/(vf_stop - vf_start)  # Scale the data, it's
        output as ints from -2^16 to 2^16
    y = data*vgain - voffset
```

```
        return x,y



    def get_single_trace(self, channel = 'C1'):
        """ Sets scope to "single" trigger mode to acquire one trace, then waits
            until the trigger has happened
        (indicated by the trigger mode changing to "Stopped").  Returns blank
            lists if no trigger occurs within 1 second """
        n = 0; x = np.array([]); y = np.array([])
        self.set_trigger_mode(trigger_mode = 'Single')
        while self.get_trigger_mode() == 'Single' or n > 1e10:
            time.sleep(1e-4)
            n = n+1
        x,y = self.get_wf_data(channel=channel)
        return x,y



    def get_num_sweeps(self,channel='F1'):  # For use with histograms, trends, etc
        return int(self.vbs_ask('app.Math.%s.Out.Result.Sweeps' % channel))



    def setup_math_trend(self, math_channel = 'F1', source = 'P1', num_values = 10
        e3):
        self.set_math(math_channel = math_channel, operator = 'Trend', source1 =
            source)
        self.vbs_write('app.Math.%s.Operator1Setup.Values = %s' % (math_channel,
            num_values))
        self.view_channel(channel = math_channel, view = True)



    def setup_math_wf_average(self, math_channel = 'F1', source = 'C1', num_sweeps
         = 100):
        self.set_math(math_channel = math_channel, operator = 'Average', source1 =
```

```
        source)
    self.vbs_write('app.Math.%s.Operator1Setup.Sweeps = %s' % (math_channel,
        num_sweeps))
    self.view_channel(channel = math_channel, view = True)


def setup_math_histogram(self, math_channel = 'F1', source = 'P1', num_values
    = 10e3,
                         num_bins = 100, center = 0, width_per_div = 1,
                             auto_scale = True):
    self.set_math(math_channel = math_channel, operator = 'Histogram', source1
        = source)
    self.vbs_write('app.Math.%s.Operator1Setup.Values = %s' % (math_channel,
        num_values))
    self.vbs_write('app.Math.%s.Operator1Setup.AutoFindScale = %s' % (
        math_channel, auto_scale))
    self.vbs_write('app.Math.%s.Operator1Setup.Bins = %s' % (math_channel,
        num_bins))
    self.vbs_write('app.Math.%s.Operator1Setup.Center = %s' % (math_channel,
        center))
    width_per_div = self.round_up_lockstep(width_per_div)
    self.vbs_write('app.Math.%s.Operator1Setup.HorScale = %s' % (math_channel,
        width_per_div))
    self.view_channel(channel = math_channel, view = True)


def collect_sweeps(self, channel = 'F1', num_sweeps = 1000):
    self.clear_sweeps()
    time.sleep(0.1)
    while (self.get_num_sweeps(channel = channel) < num_sweeps+1):
        time.sleep(0.1)
    x, ic_values = self.get_wf_data(channel=channel)
    while len(ic_values) < num_sweeps:
        time.sleep(0.05)
        x, ic_values = self.get_wf_data(channel=channel)
    return ic_values[:num_sweeps] # will occasionally return 1-2 more than
```

```
            num_sweeps



    def save_screenshot(self, file_path = None, white_background = True):
        if file_path == None:
            time_str = datetime.datetime.now().strftime('%Y-%m-%d %H-%M-%S')
            file_path = time_str + ' lecroy screenshot.png'


        # lecroy.ask('HCSU?') # Asks what the current hard copy setup is (useful
            for reference)
        if white_background: self.write('HCSU BCKG,WHITE') # Sets background to
            white
        if white_background is False: self.write('HCSU BCKG,BLACK') # Sets
            background to black
        self.write('HCSU DEV,PNG')
        self.write('HCSU FORMAT,LANDSCAPE')
        self.write('HCSU DEST,REMOTE')
        self.write('HCSU AREA,DSOWINDOW')
        self.write('SCREEN_DUMP') # Takes the screenshot
        newFileBytes = self.read()

        with open(file_path, "wb") as newFile:
            newFileByteArray = bytearray(newFileBytes)
            newFile.write(newFileByteArray)

        return file_path


#### Sample script for PyVisa 1.3
# lecroy_ip = '192.168.1.100'
# lecroy = LeCroy620Zi("TCPIP::%s::INSTR" % lecroy_ip)
# x,y = lecroy.get_wf_data('F1')
# from matplotlib import pyplot as plt
# plt.plot(x,y)
```

```
# plt.show()
```

Agilent 8153A tunable laser power meter

```
from pyvisa import visa
from time import sleep
import numpy as np

class Agilent8153A(visa.Instrument):
    """Python class for Agilent 8153A power meter, written by Adam McCaughan"""
    def __init__(self, args):
        super( visa.Instrument, self).__init__(args)
        # Anything else here that needs to happen on initialization
        self.timeout = 1 # Set timeout to 1 second



    def reset(self):
        self.write('*RST')



    def setup_basic(self, lambda_nm = 1550, averaging_time = 0.1):
        self.write('*RST')
        self.write('INIT1:CONT 1')
        self.set_averaging_time(averaging_time = averaging_time) # Sets averaging
            time, 20ms < value < 3600s
        self.set_wavelength(lambda_nm = lambda_nm)
        # self.write('OUTP 1')

    def set_averaging_time(self, averaging_time = 0.1):
        self.write('SENS1:POW:ATIME %0.3e' % averaging_time) # Sets averaging time
            , 20ms < value < 3600s

    def read_power(self):
        power = float(self.ask('READ1:POW?'))  # Returns power in watts
        return power
```

```
    def set_wavelength(self, lambda_nm):
        self.write('SENS1:POW:WAVE %0.6e' % (lambda_nm*1e-9))


# pm = Agilent8153A('GPIB0::22')
```

Agilent 33250A 80 MHz Arbitrary Waveform Generator

```
from pyvisa import visa
import numpy as np

class Agilent33250a(visa.GpibInstrument):
    """Python class for Agilent 33250a 80MHz Frequency Generator, written by Adam
        McCaughan"""
    def reset(self):
        self.write('*RST')

    def set_sin(self, freq=1000, vpp=0.1, voffset=0):
        # In a string, %0.6e converts a number to scientific notation like
        # print '%.6e' %(1234.56789) outputs '1.234568e+03'
        self.write('APPL:SIN %0.6e HZ, %0.6e VPP, %0.6e V' % (freq,vpp,voffset))

    def set_pulse(self, freq=1000, vlow=0.0, vhigh=1.0, width = 100e-6, edge_time
        = 1e-6):
        vpp = vhigh-vlow
        voffset = vpp/2
        self.write('APPL:PULS %0.6e HZ, %0.6e VPP, %0.6e V' % (freq,vpp,voffset))
        self.write('PULS:WIDT %0.6e' % (width))
        self.write('PULS:TRAN %0.6e' % (edge_time))



    def set_freq(self, freq=1000):
        self.write('FREQ %0.6e' % (freq))

    def set_vpp(self, vpp=0.1):
        self.write('VOLT %0.6e' % (vpp))

    def set_voffset(self, voffset = 0.0):
        self.write('VOLT:OFFS %0.6e' % (voffset))
```

```
def set_vhighlow(self, vlow=0.0, vhigh=1.0):
    if vhigh > vlow:
        self.set_vpp(vhigh-vlow)
        self.set_voffset((vhigh+vlow)/2.0)
        self.set_polarity(inverted = False)
    elif vhigh < vlow:
        self.set_vpp(vlow-vhigh)
        self.set_voffset((vhigh+vlow)/2.0)
        self.set_polarity(inverted = True)

def set_output(self,output=False):
    if output is True:  self.write('OUTPUT ON')
    else:               self.write('OUTPUT OFF')

def set_load(self, high_z=False):
    if high_z is True:  self.write('OUTP:LOAD INF')
    else:               self.write('OUTP:LOAD 50')

def set_polarity(self, inverted = False):
    if inverted is True:  self.write('OUTP:POL INV')
    else:               self.write('OUTP:POL NORM')

def set_trigger(self, external_trigger = False, delay = 0.0):
    if external_trigger:    self.write('TRIG:SOUR EXT' )
    else:                   self.write('TRIG:SOUR IMM' )
    self.write('TRIG:DEL %s' % (delay)) # Delay in seconds


def trigger_now(self):
    self.write('*TRG')


def set_burst_mode(self, burst_enable = True, num_cycles = 1, phase = 0):
    if burst_enable:
        self.write('BURS:STAT ON') # Enables burst state
        self.write('BURS:NCYC %s' % (num_cycles))
```

```
            self.write('BURS:PHAS %s' % (phase)) # Phase in degrees

        else:
            self.write('BURS:STAT OFF')  # Disables burst state


    def set_arb_wf(self, t = [0.0, 1e-3], v = [0.0,1.0], name = 'ARB_PY'):
        """ Input voltage values will be scaled to +/-1.0, you can then adjust the
             overall
        amplitude using the set_vpp function.  The 33250a does not allow the input
             of time for each
        point, so we instead use interpolation here to create waveform of 2^14
            equally-spaced
        points, after which you can use set_freq to get the desired freq"""

        t = np.array(t);  v = np.array(v)

        v = v-min(v);  v = 2*v/max(v);  v = v-1
        temp = self.timeout; self.timeout = 60
        t_interp = np.linspace(t[0],t[-1],2**14) # Can be up to 2**14 long
        v_interp = np.interp(t_interp, t, v)

        data_strings = ['%0.3f' % x for x in v_interp]
        data_msg = ', '.join(data_strings)

        self.write('DATA VOLATILE, ' + data_msg) # Form of "DATA VOLATILE, 1, .67,
             .33, 0, -.33", p200 user's guide
        name = name[0:8].upper()
        self.write('DATA:COPY %s, VOLATILE' % name)
        self.write('APPL:USER')  # Set output to ARB
        self.write('FUNC:USER %s' % name) # Select the waveform in the volatile
            memory
        self.write('APPL:USER')
        self.timeout = temp
        # self.write('FUNC USER') # Output the selected waveform
```

```
def setup_heartbeat_wf(self):
    heartbeat_t = [0.0, 4.0/8, 5.0/8, 6.0/8,  7.0/8, 8.0/8]
    heartbeat_v = [0.0,   0.0,   1.0,   0.0,   -1.0,   0.0]
    freq_gen.set_arb_wf(t = heartbeat_t, v = heartbeat_v, name = 'HEARTBEA')


def select_arb_wf(self, name = 'HEARTBEA'):
    name = name[0:8].upper()
    self.write('APPL:USER')  # Set output to ARB
    self.write('FUNC:USER %s' % name)
    self.write('APPL:USER')  # Set output to ARB
```

Agilent 53131A Universal Counter

```
from pyvisa import visa
import numpy as np
from time import sleep
from matplotlib import pyplot as plt

class Agilent53131a(visa.GpibInstrument):
    """Python class for Agilent 53131a counter, written by Adam McCaughan
    Use like c = Agilent53131a('GPIB0::3')"""


    def reset(self):
        self.write('*RST')

    def basic_setup(self):
        self.write('*RST')
        self.write('*CLS')

        self.write(':EVEN:LEV:AUTO OFF') # Turn off auto trigger level
        self.write(':EVEN:LEV -0.200V')  # Set trigger level
        self.write(':EVEN:SLOP NEG') # Or POS. Trigger on negative slope
        self.write(':EVEN:HYST:REL 0') # Set hysteresis (?)
        self.write(':INP:COUP AC') # Or DC.  Input coupling
        self.write(':INP:IMP 50') # Set input impedance to 50ohms
        self.write(':INP:FILT OFF') # Turn off 100kHz lowpass filter
        self.write(':FUNC "TOT 1"') # Totalize on channel 1
        self.write(':TOT:ARM:STAR:SOUR IMM') # Set start source to immediate (run
            on command)
        self.write(':TOT:ARM:STOP:SOUR TIM') # Set stop source to time (wait
            certain time)
        self.write(':TOT:ARM:STOP:TIM 0.1') # Set stop time to 100 ms
        self.write(':INP:ATT 1') # Or 10. Set attenuation factor
```

```
def set_trigger(self, trigger_voltage = -0.075, trigger_slope = None):
    if trigger_slope is 'POS' or trigger_slope is 'NEG':
        self.write(':EVEN:SLOP %s' % trigger_slope) # Or POS. Trigger on
            negative slope
    self.write(':EVEN:LEV %0.3fV' % trigger_voltage) # Set trigger level



def count_rate(self, counting_time = 0.1):
    self.write(':TOT:ARM:STOP:TIM %0.3f' % counting_time) # Set stop time to #
         of seconds
    dcr = self.ask(':READ?')
    dcr = float(dcr)/counting_time
    # time.sleep(counting_time + 0.1)
    return dcr

def counts_vs_time(self, trigger_voltage= -0.075, counting_time=0.1,
    total_time=2):
    self.set_trigger(trigger_voltage)
    num_tests = int(total_time/counting_time)
    dcr = []
    t = []
    start_time = time.time()
    for n in range(num_tests):
        dcr.append(self.get_dcr(counting_time))
        t.append(time.time() - start_time)

    return  t, dcr


def scan_trigger_voltage(self, voltage_range=[-0.2,0.2], counting_time=0.1,
    num_pts=40):
    v = np.linspace(voltage_range[0],voltage_range[1],num_pts)
    dcr = []
    for trigger_voltage in v:
        self.set_trigger(trigger_voltage)
```

```
        dcr.append(self.count_rate(counting_time))
        print 'Trigger voltage = %0.3f  /  Count rate %0.1f' % (
            trigger_voltage, dcr[-1])
    return v, np.array(dcr)/float(counting_time)
```

Anritsu MG9638A Tunable Laser Source

```
from pyvisa import visa

class AnritsuMG9638A(visa.Instrument):
    """Python class for Antritsu M9638 tunable laser source, written by Adam
        McCaughan.  Adapted from
    Mihir's MATLAB code"""
    def __init__(self, args):
        super( visa.Instrument, self).__init__(args)
        # Anything else here that needs to happen on initialization
        self.timeout = 1 # Set timeout to 1 second



    def reset(self):
        self.write('*RST')



    def setup_basic(self):
        self.write('MCW') # Set laser to CW mode
        self.write('COH ON') # Set laser to coherent mode
        self.set_power_unit('mW')
        self.set_wavelength(1550)

    def set_power_unit(self, power_unit):
        """ power_unit should be either dBm, mW, or uW """
        self.write('POWU %s' % power_unit)

    def get_power_unit(self, power_unit):
        return self.ask('POWU?')

    def get_wavelength(self):
        wavelength_str = self.ask('OUTW?')
        return float(wavelength_str)
```

```
def set_output(self, output = False):
    self.write('OUTP %d' % output)

def get_output(self):
    return bool(self.ask('OUTP?'))

def set_power(self, power, power_unit = 'uW'):
    """ power_unit should be either dBm, mW, or uW """
    power_str = self.write('POW %0.3d%s' % (power, power_unit))

def get_power(self):
    power_str = self.ask('POW?')
    return float(power_str)

def set_wavelength(self, lambda_nm):
    self.write('WCNT %0.3fNM' % lambda_nm)
```

HP 8722C Network Analyzer

```
from pyvisa import visa
from time import sleep
import numpy as np

class HP8722C(visa.GpibInstrument):
    """Python class for HP 8722C Network Analyzer, written by Adam McCaughan"""
    def reset(self):
        self.write('*RST')
        self.timeout = 5



    def freq_range(self, f_start = 0.1e9, f_stop = 1.0e9, f_center = None, f_span
        = None, num_pts = 401):

        if (f_center is not None) and (f_span is not None):
            f_start = f_center - f_span/2.0
            f_stop = f_center + f_span/2.0

        self.write('POIN %0.0i;' % num_pts)
        self.write('STAR %0.6e;' % f_start)
        self.write('STOP %0.6e;' % f_stop)

    def fixed_freq(self, f = 10e6):
        self.write('CWFREQ%0.6eHZ;' % f)

    def power(self, power = -20):
        if (power < -60) or (power > 0):
            print 'Out of range value'; return
        if   power >=  -5:  power_range = '01' # Only available below 26 GHz
        elif power >= -20:  power_range = '02'
        elif power >= -35:  power_range = '05'
        elif power >= -50:  power_range = '08'
```

```
    elif power >= -60:  power_range = '10'

    self.write('PRAN%s' % power_range)
    self.write('POWE %0.0d' % power)  # Sets power (in dBm)

def s_mode(self, s_mode = 'S11'):
    self.write('%s;' % s_mode)

def format_polar(self):
    self.write('POLA') # Set to polar coordinates

def format_logarithmic(self):
    self.write('LOGM') # Set to polar coordinates


def run_sweep_ri(self):
    """ Runs a sweep using whatever settings are currently on the NA and
        returns the real
    and imaginary components of each data point """
    self.format_polar() # Set to polar coordinates
    f_start = float(self.ask('STAR?;'))
    f_span = float(self.ask('SPAN?;'))
    f_stop = float(self.ask('STOP?;'))
    num_pts = int(float(self.ask('POIN?;')))

    print 'Sweeping from %0.0d MHz to %0.0d MHz, with %0.0d points' % (f_start
        /1e6, f_stop/1e6, num_pts)

    temp = self.timeout; self.timeout = 20
    completion = self.ask('OPC?;SING;') # Runs a SINGle sweep, and waits for
        the OPeration to Complete
    self.timeout = temp

    self.write('FORM4;') # Make the data output in ASCII
    data = self.ask_for_values('OUTPFORM;')
```

```
    F = np.linspace(f_start, f_stop, num_pts, endpoint = True)
    R = data[::2] # Every other element starting with element 0
    I = data[1::2]
    self.write('CONT')
    return F, R, I



def run_sweep_mag(self):
    """ Runs a sweep using whatever settings are currently on the NA and
        returns the real
    and imaginary components of each data point """
    self.format_logarithmic() # Set to logarithimic coordinates
    f_start = float(self.ask('STAR?;'))
    f_span = float(self.ask('SPAN?;'))
    f_stop = float(self.ask('STOP?;'))
    num_pts = int(float(self.ask('POIN?;')))

    print 'Sweeping from %0.0d MHz to %0.0d MHz, with %0.0d points' % (f_start
        /1e6, f_stop/1e6, num_pts)

    temp = self.timeout; self.timeout = 20
    completion = self.ask('OPC?;SING;') # Runs a SINGle sweep, and waits for
        the OPeration to Complete
    self.timeout = temp

    self.write('FORM4;') # Make the data output in ASCII
    data = self.ask_for_values('OUTPFORM;')

    f = np.linspace(f_start, f_stop, num_pts, endpoint = True)
    F = f[::1]
    M = data[::2] # Every other element starting with element 0
    self.write('CONT')
    return F, M
```

JDS Fitel HA9 Optical Attenuator

```
from pyvisa import visa
import numpy as np
import time

class JDSHA9(visa.Instrument):
    """Python class for JDS HJA9 Optical Attenuator, written by Adam McCaughan."""

    def __init__(self, args):
        super( visa.Instrument, self).__init__(args)
        self.timeout = 2


    def set_attenuation_db(self, attenuation_db = 10):
        self.write(('ATT %0.1f dB' % attenuation_db))


    def set_beam_block(self, beam_block = True):
        self.write(('D %0.0f' % beam_block))


# att = JDSHA9('GPIB0::10')
```

Keithley 2400 Sourcemeter

```
from pyvisa import visa

class Keithley2400(visa.Instrument):
    """Python class for Keithley 2400 Sourcemeter, written by Adam McCaughan"""
    def __init__(self, args):
        super( visa.Instrument, self).__init__(args)
        # Anything else here that needs to happen on initialization
        self.timeout = 1 # Set timeout to 1 second


    def reset(self):
        self.write('*RST')


    def setup_read_volt(self):
        self.write('*RST')
        self.write(':SOUR:FUNC CURR')
        self.write(':SOUR:CURR:LEVEL 0E-6')
        self.write('SENS:FUNC \"VOLT\"')


    def setup_4W_source_I_read_V(self):
        self.write('*RST')
        self.write(':SOUR:FUNC CURR') # Set operation mode to: source current
        self.write(':SOUR:CURR:LEVEL 0E-6') # Set current level to 0 uA
        self.write(':SYST:RSEN 1') # Turn off "Remote Sensing" aka 4-wire
            measurement mode
        self.write('SENS:FUNC \"VOLT\", \"CURR\"') # Have it output


    def setup_2W_source_I_read_V(self):
        self.write('*RST')
```

```
        self.write(':SOUR:FUNC CURR') # Set operation mode to: source current
        self.write(':SOUR:CURR:LEVEL 0E-6') # Set current level to 0 uA
        self.write(':SYST:RSEN 0') # Turn off "Remote Sensing" aka 4-wire
            measurement mode
        self.write('SENS:FUNC \"VOLT\", \"CURR\"') # Have it output


    def setup_2W_source_V_read_I(self):
        self.write('*RST')
        self.write(':SOUR:FUNC VOLT') # Set operation mode to: source voltage
        self.write(':SOUR:VOLT:LEVEL 0E-3') # Set voltage level to 0 mV
        self.write(':SYST:RSEN 0') # Turn off "Remote Sensing" aka 4-wire
            measurement mode
        self.write('SENS:FUNC \"VOLT\", \"CURR\"') # Have it output


    def set_output(self, output = False):
        if output is True:  self.write(':OUTP ON')
        if output is False: self.write(':OUTP OFF')


    def set_measurement_time(self, plc_cycles = 1.0):
        """ plc_cycles Sets integration time Keithley.  Each cycle corresponds to
        1/60th of a second.  Default is 1.0, Max is 10.0. Min is 0.01.  See
            Keithley
        manual p18-70 for more details """
        self.write(':NPLCycles %0.2f' % plc_cycles)


    def disable_remote(self):
        """ Simulates the pressing of the "LOCAL" button on the Keithley
        which will take the keithley out of remote mode """
        self.write(':SYST:KEY 23')


    def set_compliance_i(self, compliance_i = 10e-6):
```

```
        self.write(':SENS:CURR:PROT %0.3e' % compliance_i)


    def set_compliance_v(self, compliance_v = 10e-6):
        self.write(':SENS:VOLT:PROT %0.3e' % compliance_v)


    def set_current(self, current = 0e-6):
        self.write(':SOUR:CURR:LEVEL %0.4e' % current)   # Set current level


    def set_voltage(self, voltage = 0e-6):
        self.write(':SOUR:VOLT:LEVEL %0.4e' % voltage)   # Set current level


    def read_voltage_and_current(self):
        read_str = self.ask(':READ?')
        # See page 18-51 of manual, returns: voltage, current, resistance,
            timestamp, status info
        # Returns something like '5.275894E-05,-1.508318E-06,+9.910000E
            +37,+2.562604E+03,+3.994000E+04'
        data = read_str.split(',')
        voltage, current = float(data[0]), float(data[1])
        return voltage, current


    def read_current(self, current = 0e-6):
        voltage, current = self.read_voltage_and_current()
        return current


    def read_voltage(self):
        voltage, current = self.read_voltage_and_current()
        return voltage
```

SRS SIM928 adjustable voltage source

```
from pyvisa import visa

class SIM928(visa.Instrument):
    """Python class for SRS SIM928 Isolated Voltage Source inside a SIM900
    mainframe, written by Adam McCaughan"""
    def __init__(self, sim900port, args):
        super( visa.Instrument, self).__init__(args)
        self.sim900port = sim900port
        # Anything else here that needs to happen on initialization
    def write_simport(self, message):
        write_str = 'SNDT ' + str(self.sim900port) + ',\"' + message + '\"'
        # print write_str
        self.write(write_str) # Format of 'SNDT 4,\"GAIN 10\"'
    def ask_simport(self, message):
        write_str = 'SNDT ' + str(self.sim900port) + ',\"' + message + '\"'
        return self.ask(write_str) # Format of 'SNDT 4,\"GAIN 10\"'
    def reset(self):
        self.write_simport('*RST')
    def set_voltage(self, voltage=0.0):
        # In a string, %0.4e converts a number to scientific notation
        self.write_simport('VOLT %0.4e' %(voltage))
    def set_output(self, output=False):
        if output==True:
            self.write_simport('OPON')
        else:
            self.write_simport('OPOF')  # Only uses "OPOF" or "OPON": "OPOFF" does
                not work
```

Bibliography

[1] M. W. Brenner, D. Roy, N. Shah, and A. Bezryadin. Dynamics of superconducting nanowires shunted with an external resistor. *Phys. Rev. B*, 85(22):224507, June 2012.

[2] D. S. Holmes, A. L. Ripple, and M. A. Manheimer. Energy-Efficient Superconducting Computing–Power Budgets and Requirements. *IEEE Trans. Appl. Supercond.*, 23(3):1701610–1701610, June 2013.

[3] Robert H. Hadfield. Single-photon detectors for optical quantum information applications. *Nat. Photonics*, 3(12):696–705, December 2009.

[4] Jonas Zmuidzinas. Superconducting Microresonators: Physics and Applications. *Annu. Rev. Condens. Matter Phys.*, 3(1):169–214, March 2012.

[5] Karsten Sternickel and Alex I Braginski. Biomagnetism using SQUIDs: status and perspectives. *Supercond. Sci. Technol.*, 19(3):S160–S171, March 2006.

[6] John Clarke and Frank K. Wilhelm. Superconducting quantum bits. *Nature*, 453(7198):1031–1042, June 2008.

[7] Don M. Boroson, Bryan S. Robinson, Daniel V. Murphy, Dennis A. Burianek, Farzana Khatri, Joseph M. Kovalik, Zoran Sodnik, and Donald M. Cornwell. Overview and results of the Lunar Laser Communication Demonstration. In Hamid Hemmati and Don M. Boroson, editors, *SPIE Photonics West 2014-LASE Lasers Sources*, volume 8971, page 89710S, March 2014.

[8] Jonas Zmuidzinas and Paul L Richards. Superconducting Detectors and Mixers for Millimeter and Submillimeter Astrophysics. *October*, 92(10), 2004.

[9] Peter K. Day, Henry G. LeDuc, Benjamin A. Mazin, Anastasios Vayonakis, and Jonas Zmuidzinas. A broadband superconducting detector suitable for use in large arrays. *Nature*, 425(6960):817–821, October 2003.

[10] W. J. Skocpol, M. R. Beasley, and M. Tinkham. Phase-slip centers and nonequilibrium processes in superconducting tin microbridges. *J. Low Temp. Phys.*, 16(1-2):145–167, July 1974.

[11] T. M. Klapwijk. Proximity effect from an Andreev perspective. *J. Supercond.*, 17(5):593–611, October 2004.

[12] Cihan Kurter, Alexander P. Zhuravel, Alexey V. Ustinov, and Steven M. Anlage. Microscopic examination of hot spots giving rise to nonlinearity in superconducting resonators. *Phys. Rev. B*, 84(10):104515, September 2011.

[13] T. Orlando, J. Mooij, L. Tian, C. van der Wal, L. Levitov, S. Lloyd, and J. Mazo. Superconducting persistent-current qubit. *Phys. Rev. B*, 60(22):15398–15413, 1999.

[14] J. J. A. Baselmans, A. F. Morpurgo, B. J. van Wees, and T. M. Klapwijk. Reversing the direction of the supercurrent in a controllable Josephson junction. *Nature*, 397(6714):43–45, January 1999.

[15] S. Nagasawa, S. Tahara, H. Numata, and S. Tsuchida. A miniaturized vortex transitional memory cell for a Josephson high-speed RAM. *Electron Devices Meet. 1992. IEDM '92. Tech. Dig. Int.*, pages 793–796, 1992.

[16] B.D. Josephson. Possible new effects in superconductive tunnelling. *Phys. Lett.*, 1(7):251–253, 1962.

[17] K. K. Likharev and V. K. Semenov. RSFQ logic/memory family: a new Josephson-junction technology for sub-terahertz-clock-frequency digital systems. *IEEE Trans. Appiled Supercond.*, 1(1):3–28, March 1991.

[18] Konstantin K. Likharev. Superconductor digital electronics. *Phys. C Supercond.*, 482:6–18, November 2012.

[19] W. Chen, A.V. Rylyakov, V. Patel, J.E. Lukens, and K.K. Likharev. Rapid single flux quantum T-flip flop operating up to 770 GHz. *IEEE Trans. Appiled Supercond.*, 9(2):3212–3215, June 1999.

[20] S Pagano and A Barone. Josephson junctions. *Supercond. Sci. Technol.*, 10(12):904–908, December 1997.

[21] P. de Vegvar, T. Fulton, W. Mallison, and R. Miller. Mesoscopic Transport in Tunable Andreev Interferometers. *Phys. Rev. Lett.*, 73(10):1416–1419, September 1994.

[22] P Cadden-Zimansky, J Wei, and V Chandrasekhar. Coherent nonlocal correlations in Andreev interferometers. *New J. Phys.*, 14(4):043004, April 2012.

[23] Christopher Checkley. *Andreev Interferometry of Flux Qubits Driven By Radio Frequency Field*. PhD thesis, 2010.

[24] Alex D. Semenov, Gregory N. Gol'tsman, and Alexander A. Korneev. Quantum detection by current carrying superconducting film. *Phys. C Supercond.*, 351(4):349–356, April 2001.

[25] Faraz Najafi, Jacob Mower, Nicholas C Harris, Francesco Bellei, Andrew Dane, Catherine Lee, Xiaolong Hu, Prashanta Kharel, Francesco Marsili, Solomon Assefa, Karl K Berggren, and Dirk Englund. On-chip detection of non-classical light by scalable integration of single-photon detectors. *Nat. Commun.*, 6:5873, January 2015.

[26] Nathan R. Gemmell, Aongus McCarthy, Baochang Liu, Michael G. Tanner, Sander D. Dorenbos, Valery Zwiller, Michael S. Patterson, Gerald S. Buller, Brian C. Wilson, and Robert H. Hadfield. Singlet oxygen luminescence detection with a fiber-coupled superconducting nanowire single-photon detector. *Opt. Express*, 21(4):5005, February 2013.

[27] M.K. Mc Manus, J.A. Kash, S.E. Steen, S Polonsky, J.C. Tsang, D.R. Knebel, and W Huott. PICA: Backside failure analysis of CMOS circuits using Picosecond Imaging Circuit Analysis. *Microelectron. Reliab.*, 40(8-10):1353–1358, August 2000.

[28] Matthew E. Grein, Andrew J. Kerman, Eric A. Dauler, Oleg Shatrovoy, Richard J. Molnar, Danna Rosenberg, Jung Yoon, Catherine E. DeVoe, Daniel V. Murphy, Bryan S. Robinson, and Don M. Boroson. Design of a ground-based optical receiver for the lunar laser communications demonstration. In *2011 Int. Conf. Sp. Opt. Syst. Appl.*, pages 78–82. IEEE, May 2011.

[29] J Zmuidzinas. Superconducting Microresonator Detectors. pages 1–12, 2008.

[30] S. J. C. Yates, A. M. Baryshev, J. J. A. Baselmans, B. Klein, and R. Gusten. Fast Fourier transform spectrometer readout for large arrays of microwave kinetic inductance detectors. *Appl. Phys. Lett.*, 95(4):042504, 2009.

[31] W. Gallagher. Three-terminal superconducting devices. *IEEE Trans. Magn.*, 21(2):709–716, March 1985.

[32] D. Buck. The Cryotron-A Superconductive Computer Component. *Proc. IRE*, 44(4):482–493, April 1956.

[33] A. F. Morpurgo, T. M. Klapwijk, and B. J. van Wees. Hot electron tunable supercurrent. *Appl. Phys. Lett.*, 72(8):966, 1998.

[34] Seung-Beck Lee, Gregory D Hutchinson, David a Williams, David G Hasko, and Haroon Ahmed. Superconducting nanotransistor based digital logic gates. *Nanotechnology*, 14(2):188–191, February 2003.

[35] R. Sprik, W. J. Gallagher, S. I. Raider, B. Bumble, and C.-C. Chi. Transient response of quasiparticle injected superconducting links. *Appl. Phys. Lett.*, 55(5):489, 1989.

[36] Ting Wah Wong, J. T C Yeh, and D. N. Langenberg. Quasiparticle-injection-induced superconducting weak links. *Phys. Rev. Lett.*, 37(3):150–153, July 1976.

[37] S. Faris, S. Raider, W. Gallagher, and R. Drake. Quiteron. *IEEE Trans. Magn.*, 19(3):1293–1295, May 1983.

[38] Tatsushi Akazaki, Hideaki Takayanagi, Junsaku Nitta, and Takatomo Enoki. A Josephson field effect transistor using an InAs-inserted-channel In0.52Al0.48As/In0.53Ga0.47As inverted modulation-doped structure. *Appl. Phys. Lett.*, 68(3):418, 1996.

[39] Huigao Duan, Hailong Hu, Karthik Kumar, Zexiang Shen, and Joel K W Yang. Direct and Reliable Patterning of Plasmonic Nanostructures with Sub-10-nm Gaps. *ACS Nano*, 5(9):7593–7600, September 2011.

[40] Joel K. W. Yang and Karl K. Berggren. Using high-contrast salty development of hydrogen silsesquioxane for sub-10-nm half-pitch lithography. *J. Vac. Sci. Technol. B Microelectron. Nanom. Struct.*, 25(6):2025, 2007.

[41] Francesco Marsili, Faraz Najafi, Eric Dauler, Francesco Bellei, Xiaolong Hu, Maria Csete, Richard J Molnar, and Karl K Berggren. Single-photon detectors based on ultranarrow superconducting nanowires. *Nano Lett.*, 11(5):2048–53, May 2011.

[42] C. P. Foley and H. Hilgenkamp. Why NanoSQUIDs are important: an introduction to the focus issue. *Supercond. Sci. Technol.*, 22(6):064001, June 2009.

[43] Amit Finkler, Yehonathan Segev, Yuri Myasoedov, Michael L. Rappaport, Lior Ne'eman, Denis Vasyukov, Eli Zeldov, Martin E. Huber, Jens Martin, and Amir Yacoby. Self-Aligned Nanoscale SQUID on a Tip. *Nano Lett.*, 10(3):1046–1049, March 2010.

[44] Denis Vasyukov, Yonathan Anahory, Lior Embon, Dorri Halbertal, Jo Cuppens, Lior Neeman, Amit Finkler, Yehonathan Segev, Yuri Myasoedov, Michael L Rappaport, Martin E Huber, and Eli Zeldov. A scanning superconducting quantum interference device with single electron spin sensitivity. *Nat. Nanotechnol.*, 8(September):639–44, 2013.

[45] Quentin P. Herr, Anna Y. Herr, Oliver T. Oberg, and Alexander G. Ioannidis. Ultra-low-power superconductor logic. *J. Appl. Phys.*, 109(10):103903, 2011.

[46] M. Tinkham. *Introduction to Superconductivity: Second Edition.* Dover Books on Physics. Dover Publications, 2004.

[47] Terry P. Orlando and Kevin A. Delin. *Foundations of Applied Superconductivity.* Reading, MA, 1990.

[48] G. N. Gol'tsman, O. Okunev, G. Chulkova, A. Lipatov, A. Semenov, K. Smirnov, B. Voronov, A. Dzardanov, C. Williams, and Roman Sobolewski. Picosecond superconducting single-photon optical detector. *Appl. Phys. Lett.*, 79(6):705, 2001.

[49] Kristine M Rosfjord, Joel K W Yang, Eric A Dauler, Andrew J Kerman, Vikas Anant, Boris M Voronov, Gregory N Gol'tsman, and Karl K Berggren. Nanowire single-photon detector with an integrated optical cavity and anti-reflection coating. *Opt. Express*, 14(2):527, 2006.

[50] F Marsili, V B Verma, J A Stern, S Harrington, A E Lita, T Gerrits, I Vayshenker, B Baek, M D Shaw, R P Mirin, and S W Nam. Detecting single infrared photons with 93% system efficiency. *Nat. Photonics*, 7(3):210–214, February 2013.

[51] Andrew J. Kerman, Eric A. Dauler, William E. Keicher, Joel K. W. Yang, Karl K. Berggren, G. Gol'tsman, and B. Voronov. Kinetic-inductance-limited reset time of superconducting nanowire photon counters. *Appl. Phys. Lett.*, 88(11):111116, 2006.

[52] Andrew Kerman, Joel Yang, Richard Molnar, Eric Dauler, and Karl Berggren. Electrothermal feedback in superconducting nanowire single-photon detectors. *Phys. Rev. B*, 79(10):1–4, March 2009.

[53] S Berg. Fundamental understanding and modeling of reactive sputtering processes. *Thin Solid Films*, 476:215–230, 2005.

[54] J.K.W. Yang, A.J. Kerman, E.A. Dauler, V. Anant, K.M. Rosfjord, and K.K. Berggren. Modeling the Electrical and Thermal Response of Superconducting Nanowire Single-Photon Detectors. *IEEE Trans. Appl. Supercond.*, 17(2):581–585, June 2007.

[55] A. Semenov, R. Nebosis, Yu. Gousev, M. Heusinger, and K. Renk. Analysis of the nonequilibrium photoresponse of superconducting films to pulsed radiation by use of a two-temperature model. *Phys. Rev. B*, 52(1):581–590, July 1995.

[56] K.D. Irwin, S.W. Nam, B. Cabrera, B. Chugg, G.S. Park, R.P. Welty, and J.M. Martinis. A self-biasing cryogenic particle detector utilizing electrothermal feedback and a SQUID readout. *IEEE Trans. Appl. Supercond.*, 5(2):2690–2693, 1995.

[57] John R Clem. Current-Induced Suppression of Superconductivity in Thin Films due to Simple Geometric Effects. *Physics (College. Park. Md).*, pages 1–10, 2011.

[58] F Gross, BS Chandrasekhar, and D Einzel. Anomalous temperature dependence of the magnetic field penetration depth in superconducting UBe13. *Zeitschrift für Phys. B ...*, 188:175–188, 1986.

[59] M. Tinkham, J. Free, C. Lau, and N. Markovic. Hysteretic I-V curves of superconducting nanowires. *Phys. Rev. B*, 68(13):1–7, October 2003.

[60] W. J. Skocpol, M. R. Beasley, and M. Tinkham. Self-heating hotspots in superconducting thin-film microbridges. *J. Appl. Phys.*, 45(9):4054, 1974.

[61] Albert Schmid. A time dependent Ginzburg-Landau equation and its application to the problem of resistivity in the mixed state. *Phys. der Kondens. Mater.*, 5(4):302–317, 1966.

[62] Klaus D. Usadel. Generalized diffusion equation for superconducting alloys. *Phys. Rev. Lett.*, 25(8):507–509, 1970.

[63] L. N. Bulaevskii, M. J. Graf, C. D. Batista, and V. G. Kogan. Vortex-induced dissipation in narrow current-biased thin-film superconducting strips. *Phys. Rev. B*, 83(14):144526, April 2011.

[64] Simon K H Lam and Sabaratnasingam Gnanarajan. Hysteretic behaviour of nanoSQUIDs–prospective application as trapped-vortex memory. *Supercond. Sci. Technol.*, 22(6):064005, June 2009.

[65] AH Dayem and JJ Wiegand. Behavior of Thin-Film Superconducting Bridges in a Microwave Field. *Phys. Rev.*, 155(2):419–428, March 1967.

[66] H. Fink, V. Grünfeld, and A. López. Quantum-interference device without Josephson junctions. *Phys. Rev. B*, 35(1):35–37, January 1987.

[67] Aico G. P. Troeman, Hendrie Derking, Bert Borger, Johannes Pleikies, Dick Veldhuis, and Hans Hilgenkamp. NanoSQUIDs Based on Niobium Constrictions. *Nano Lett.*, 7(7):2152–2156, July 2007.

[68] K. Hasselbach, C. Veauvy, and D. Mailly. MicroSQUID magnetometry and magnetic imaging. *Phys. C Supercond. its Appl.*, 332:140–147, 2000.

[69] Simon K H Lam, John R Clem, and Wenrong Yang. A nanoscale SQUID operating at high magnetic fields. *Nanotechnology*, 22(45):455501, December 2011.

[70] C H Wu, Y T Chou, W C Kuo, J H Chen, L M Wang, J C Chen, K L Chen, U C Sou, H C Yang, and J T Jeng. Fabrication and characterization of high-T(c) YBa(2)Cu(3)O(7-x) nanoSQUIDs made by focused ion beam milling. *Nanotechnology*, 19(31):315304, 2008.

[71] R. Arpaia, M. Arzeo, S. Nawaz, S. Charpentier, F. Lombardi, and T. Bauch. Ultra low noise YBa2Cu3O7-δ nano superconducting quantum interference devices implementing nanowires. *Appl. Phys. Lett.*, 104(7):0–4, February 2014.

[72] V. V. Moshchalkov, L. Gielen, M. Dhallé, C. Van Haesendonck, and Y. Bruynseraede. Quantum interference in a mesoscopic superconducting loop. *Nature*, 361(6413):617–620, February 1993.

[73] Sebastien Michotte, Damien Lucot, and Dominique Mailly. Fluxoid quantization in the critical current of a niobium superconducting loop far below the critical temperature. *Phys. Rev. B*, 81(10):100503, March 2010.

[74] S. Adam, X. Hallet, L. Piraux, D. Lucot, and D. Mailly. Switching current modulations induced by vortices rearrangement in mesoscopic superconducting loops. *Phys. Rev. B*, 84(10):104512, September 2011.

[75] A. Gubin, K. Il'in, S. Vitusevich, M. Siegel, and N. Klein. Dependence of magnetic penetration depth on the thickness of superconducting Nb thin films. *Phys. Rev. B*, 72(6):1–8, August 2005.

[76] A. Troeman, S. van der Ploeg, E. Il'Ichev, H.-G. Meyer, A. Golubov, M. Kupriyanov, and H. Hilgenkamp. Temperature dependence measurements of the supercurrent-phase relationship in niobium nanobridges. *Phys. Rev. B*, 77(2):024509, January 2008.

[77] K. K. Likharev. Superconducting weak links. *Rev. Mod. Phys.*, 51(1):101–159, January 1979.

[78] John Clem and V. Kogan. Kinetic impedance and depairing in thin and narrow superconducting films. *Phys. Rev. B*, 86(17):174521, November 2012.

[79] Anthony J Annunziata, Daniel F Santavicca, Luigi Frunzio, Gianluigi Catelani, Michael J Rooks, Aviad Frydman, and Daniel E Prober. Tunable superconducting nanoinductors. *Nanotechnology*, 21(44):445202, November 2010.

[80] K. Il'in, M. Siegel, A. Semenov, A. Engel, and H.-W. Hï£¡bers. Critical current of Nb and NbN thin-film structures: The cross-section dependence. *Phys. status solidi*, 2(5):1680–1687, March 2005.

[81] S. Michotte, S. Mátéfi-Tempfli, L. Piraux, D. Vodolazov, and F. Peeters. Condition for the occurrence of phase slip centers in superconducting nanowires under applied current or voltage. *Phys. Rev. B*, 69(9):094512, March 2004.

[82] Shi-zeng Lin and Lev N Bulaevskii. I-V characteristics of short superconducting nanowires with different bias and shunt: a dynamic approach. page 5, August 2013.

[83] A. T. Fiory, A. F. Hebard, P. M. Mankiewich, and R. E. Howard. Penetration depths of high Tc films measured by two-coil mutual inductances. *Appl. Phys. Lett.*, 52(25):2165, 1988.

[84] Adam N. McCaughan and Karl K. Berggren. A superconducting-nanowire three-terminal electrothermal device. *Nano Lett.*, 14(10):5748–53, October 2014.

[85] M Ejrnaes, A Casaburi, R Cristiano, N Martucciello, F Mattioli, A Gaggero, R Leoni, J-C Villégier, and S Pagano. Characterization of superconducting pulse discriminators based on parallel NbN nanostriplines. *Supercond. Sci. Technol.*, 24(3):035018, March 2011.

[86] AV Gurevich and RG Mints. Self-heating in normal metals and superconductors. *Rev. Mod. Phys.*, 59(4):941–999, October 1987.

[87] TL Peterson, I. Maartense, and R.R. Biggers. Self-heating hotspot effects in HTS thin films. *IEEE Trans. Appl. Supercond.*, 5(2):1436–1439, June 1995.

[88] Allen Rothwarf and B. N. Taylor. Measurement of recombination lifetimes in superconductors. *Phys. Rev. Lett.*, 19(1):27–30, July 1967.

[89] D. E. Prober. Superconducting terahertz mixer using a transition-edge microbolometer. *Appl. Phys. Lett.*, 62(17):2119, 1993.

[90] Anthony J. Annunziata, Orlando Quaranta, Daniel F. Santavicca, Alessandro Casaburi, Luigi Frunzio, Mikkel Ejrnaes, Michael J. Rooks, Roberto Cristiano, Sergio Pagano, Aviad Frydman, and Daniel E. Prober. Reset dynamics and latching in niobium superconducting nanowire single-photon detectors. *J. Appl. Phys.*, 108(8):084507, 2010.

[91] F. Najafi, F. Marsili, E. Dauler, R. J. Molnar, and K. K. Berggren. Timing performance of 30-nm-wide superconducting nanowire avalanche photodetectors. *Appl. Phys. Lett.*, 100(15):152602, 2012.

[92] K. S. Il'in, M. Lindgren, M. Currie, A. D. Semenov, G. N. Gol'tsman, Roman Sobolewski, S. I. Cherednichenko, and E. M. Gershenzon. Picosecond hot-electron energy relaxation in NbN superconducting photodetectors. *Appl. Phys. Lett.*, 76(19):2752, 2000.

[93] M. Beck, M. Klammer, S. Lang, P. Leiderer, V. V. Kabanov, G. N. Gol'tsman, and J. Demsar. Energy-Gap Dynamics of Superconducting NbN Thin Films Studied by Time-Resolved Terahertz Spectroscopy. *Phys. Rev. Lett.*, 107(17):177007, October 2011.

[94] M H Volkmann, A Sahu, C J Fourie, and O a Mukhanov. Implementation of energy efficient single flux quantum digital circuits with sub-aJ/bit operation. *Supercond. Sci. Technol.*, 26(1):015002, January 2013.

[95] H. L. Hortensius, E. F. C. Driessen, T. M. Klapwijk, K. K. Berggren, and J. R. Clem. Critical-current reduction in thin superconducting wires due to current crowding. *Appl. Phys. Lett.*, 100(18):182602, 2012.

[96] M. Bell, A. Sergeev, V. Mitin, J. Bird, A. Verevkin, and G. Gol'tsman. One-dimensional resistive states in quasi-two-dimensional superconductors: Experiment and theory. *Phys. Rev. B*, 76(9):094521, September 2007.

[97] Nayana Shah, David Pekker, and Paul Goldbart. Inherent Stochasticity of Superconductor-Resistor Switching Behavior in Nanowires. *Phys. Rev. Lett.*, 101(20):207001, November 2008.

[98] M Sahu. *Switching current distributions of superconducting nanowires: Evidence of quantum phase slip events*. PhD thesis, 2009.

[99] J. B. Johnson. Thermal Agitation of Electricity in Conductors. *Phys. Rev.*, 32(1):97–109, July 1928.

[100] Hiroyuki Shibata, Kaoru Shimizu, Hiroki Takesue, and Yasuhiro Tokura. Ultimate low system dark count rate for superconducting nanowire single-photon detector. pages 3–6, 2015.

[101] Peng Li, Phillip Wu, Yuriy Bomze, Ivan Borzenets, Gleb Finkelstein, and A. Chang. Switching Currents Limited by Single Phase Slips in One-Dimensional Superconducting Al Nanowires. *Phys. Rev. Lett.*, 107(13):1–5, September 2011.

[102] Jack Ekin. *Experimental Techniques for Low-Temperature Measurements*. Oxford University Press, October 2006.